SYNTHESIS AND CHARACTERIZATION OF MULTIFUNCTIONAL $GdB_3O_6/Ca_{10}(PO_4)_6(OH)_2$ CORE/SHELL PARTICLES FOR BIOMEDICAL APPLICATIONS

A THESIS SUBMITTED TO
THE GRADUATE SCHOOL OF NATURAL AND APPLIED SCIENCES
OF
MIDDLE EAST TECHNICAL UNIVERSITY

BY

MEHMET BURAK UZUN

IN PARTIAL FULFILLMENT OF THE REQUIREMENTS
FOR
THE DEGREE OF MASTER OF SCIENCE
IN
CHEMISTRY

JANUARY 2023

Approval of the thesis:

SYNTHESIS AND CHARACTERIZATION OF MULTIFUNCTIONAL $GdB_3O_6/Ca_{10}(PO_4)_6(OH)_2$ CORE/SHELL PARTICLES FOR BIOMEDICAL APPLICATIONS

submitted by **MEHMET BURAK UZUN** in partial fulfillment of the requirements for the degree of **Master of Science** i**n Chemistry, Middle East Technical University** by,

Prof. Dr. Halil Kalıpçılar
Dean, Graduate School of **Natural and Applied Sciences** _____

Prof. Dr. Özdemir Doğan
Head of the Department, **Chemistry** _____

Prof. Dr. Ayşen Yılmaz
Supervisor, **Chemistry, METU** _____

Examining Committee Members:

Prof. Dr. Gülsün Arslan Gökağaç
Chemistry, METU _____

Prof. Dr. Ayşen Yılmaz
Chemistry, METU _____

Prof. Dr. İrem Erel Göktepe
Chemistry, METU _____

Assoc. Prof. Dr. Özgül Persil Çetinkol
Chemistry, METU _____

Assist. Prof. Dr. Okan İçten
Chemistry, Hacettepe University _____

Date: 06.01.2023

I hereby declare that all information in this document has been obtained and presented in accordance with academic rules and ethical conduct. I also declare that, as required by these rules and conduct, I have fully cited and referenced all material and results that are not original to this work.

Name Last name : Mehmet Burak Uzun

Signature :

ABSTRACT

SYNTHESIS AND CHARACTERIZATION OF MULTIFUNCTIONAL $GdB_3O_6/Ca_{10}(PO_4)_6(OH)_2$ CORE/SHELL PARTICLES FOR BIOMEDICAL APPLICATIONS

Uzun, Mehmet Burak
Master of Science, Chemistry
Supervisor: Prof. Dr. Ayşen Yılmaz

January 2023, 94 pages

Multifunctional particles with multiple properties are used in biomedical applications for cancer treatment. With the recently developing technology, particles with photoluminescent properties can perform real-time imaging. In this study, Ce^{3+}/Tb^{3+} co-doped, Eu^{3+} doped GdB_3O_6 particles were synthesized, coated with hydroxyapatite (HAP) and polyethylene glycol (PEG). Then, particles were loaded with doxorubicin. Ce^{3+}/Tb^{3+} co-doped and Eu^{3+} doped GdB_3O_6 particles were synthesized by the sol-gel process using different chelating agents and surfactant (Cetyltrimethylammonium bromide (CTAB), citric acid, glycine, ethylenediaminetetraacetic acid (EDTA), tartaric acid, phthalic acid) to see the effect of different chelating agents or surfactant on the structure. Ce^{3+}/Tb^{3+} co-doped $Gd_{0.95}Ce_{0.025}Tb_{0.025}B_3O_6$ compound with the highest crystallinity and luminescence intensity was obtained with CTAB. The Eu^{3+} ions were doped at different molar ratios in subsequent experiments. An increase in luminescence intensity was observed with increased amounts of Eu^{3+} ions, where the highest luminescence intensity was obtained in the $Gd_{0.825}Eu_{0.175}B_3O_6$ nanoparticle. $GdBO_3$ particles doped with Eu^{3+} ions were also synthesized under the same conditions and the highest luminescence intensity was obtained in $Gd_{0.80}Eu_{0.20}BO_3$ nanoparticles. The core was

coated with hydroxyapatite to increase the drug loading efficiency. Hydroxyapatite was synthesized on the core by the wet precipitation method. The core had an average size of 458.65 nm and was analyzed with dynamic light scattering (DLS) as 616.85 nm after coating. The hydroxyapatite-coated core was then coated with non-cytotoxic PEG 10000 to increase the liquid circulation time and colloidal stability. $Gd_{0.825}Eu_{0.175}B_3O_6$@HAP@PEG particles were mixed in doxorubicin for 24 hours and drug loading was completed. Drug releases were then studied at 37 °C in pH 7.4 phosphate buffered saline (PBS) and pH 5.5 acetate buffer solutions. During the release studies, the total number of moles of drug released versus luminescence intensity was measured and real-time imaging studies were completed. Finally, cytotoxicity experiments were performed on HCT-116 colon cancer cells.

Keywords: Borates, Core/shell, Drug delivery, Real-time monitoring, Hydroxyapatite

ÖZ

BİYOMEDİKAL UYGULAMALAR İÇİN ÇEKİRDEK/KABUK TİPİ $GdB_3O_6/Ca_{10}(PO_4)(OH)_2$ PARÇACIKLARININ SENTEZİ VE KARAKTERİZASYONU

Uzun, Mehmet Burak
Yüksek Lisans, Kimya
Tez Yöneticisi: Prof. Dr. Ayşen Yılmaz

Ocak 2023, 94 sayfa

Bünyesinde birden çok özelliği bulunduran parçacıklar biyomedikal uygulamalar için kanser tedavisinde kullanılmaktadırlar. Son zamanlarda gelişen teknolojiyle birlikte fotolüminesan özellik gösteren parçacıklar gerçek zamanlı görüntüleme yapabilmektedirler. Bu çalışmada, Ce^{3+}/Tb^{3+} katkılı, Eu^{3+} katkılı GdB_3O_6 parçacıkları sentezlenmiş, hydroksiapatit ve polietilen glikol ile kaplanmıştır. Sonra, parçacıklara doksorubisin yüklenmiştir. Ce^{3+}/Tb^{3+}, Eu^{3+} katkılı GdB_3O_6 parçacıklar sol-jel yöntemiyle sentezlenmiştir. Farklı şelat ajanları ve yüzey aktif maddeler (Setiltrimetilammonyum bromür (CTAB), sitrik asit, glisin, etilendiamin tetra asetik asit (EDTA), tartarik asit, fitalik asit) kullanılarak gerçekleştirilen sentezlerde, farklı şelat ajanlarının ve yüzey aktif maddelerin yapı üzerindeki etkisi araştırılmıştır. Ce^{3+}/Tb^{3+} katkılı $Gd_{0.95}Ce_{0.025}Tb_{0.025}B_3O_6$ parçacıklarında en yüksek ışıma şiddeti ve kristallilik CTAB ile yapılan sentezde gözlemlenmiştir. Devam eden çalışmalarda, Eu^{3+} katkılı parçacıklar farklı mol oranlarıyla katkılanmıştır. En yüksek ışıma şiddeti $Gd_{0.825}Eu_{0.175}B_3O_6$ parçacığında, Eu^{3+} oranının artmasıyla elde edilmiştir. Aynı şartlar altında Eu^{3+} katkılı $GdBO_3$ parçacıkları sentezlenmiş olup, en yüksek ışıma şiddeti $Gd_{0.80}Eu_{0.20}BO_3$ parçacığında gözlemlenmiştir. Çekirdek ilaç yükleme verimini artırmak için hidroksiapatit ile kaplanmıştır. Hidroksiapatit yaş çöktürme yöntemiyle sentezlenmiştir. Çekirdek 458.65 nm parçacık boyu dağılımına sahipken

kaplamadan sonra 616.85 nm parçacık boyu dağılımı dinamik ışık saçılımı yöntemiyle belirlenmiştir. Daha sonrasında, dolaşım süresini artırmak ve kolloidal kararlılık sağlamak için hidroksiapatit kaplanmış çekirdek, sitotoksik olmayan PEG 10000 ile kaplanmıştır. $Gd_{0.825}Eu_{0.175}B_3O_6$@HAP@PEG parçacıkları doksorubisin ile 24 saat karıştırılarak ilaç yüklemesi tamamlanmıştır. İlaç salımı 37 °C de pH 7.4 fosfat tamponlu tuz (PBS) ve pH 5.5 asetat tampon çözeltilerinde çalışılmıştır. Salım çalışmaları sırasında, toplam salımı yapılan mol sayısına karşılık lüminesan şiddeti ölçülmüştür ve böylelikle gerçek zamanlı görüntüleme çalışmaları tamamlanmıştır. Son olarak, HCT-116 kolon kanser hücrelerinde parçacıkların sitotoksisite çalışmaları tamamlanmıştır.

Anahtar Kelimeler: Borat, Çekirdek/kabuk, İlaç taşıma, Gerçek zamanlı görüntüleme, Hidroksiapatit

To my family…

ACKNOWLEDGMENTS

The author wishes to express his deepest gratitude to his supervisor Prof. Dr. Ayşen Yılmaz for her guidance, advice, criticism and letting me chance to study such a great subject.

The author would also like to thank Prof. Dr. Okan Esentürk for his suggestions and comments.

Other thanks to Assoc. Prof. Dr. Özgül Persil Çetinkol and Mehrdad Forough for letting me use their laboratory for the utilization of photoluminescence and UV-VIS measurements.

The author also thanks Prof. Dr. İrem Erel Göktepe and Gökçe Tidim to help me deal with DLS and zeta potential measurements.

Other thanks to Prof. Dr. Enver Bulur for his help with decay measurements.

İsmail Güderer and Prof. Dr. Sreeparna Banerjee, I appreciate their help with the MTT assay.

I also would like to thank to my laboratory mates Dr. Sera İflazoğlu, Gencay Çelik, Özde Ceren Abacı, İpek Yıldırım, Oğuzcan Taneroğlu and Pelin Akman for their help and friendships.

I also would like to very thank my friends Osman Karaman, Ceren Akgül, Ozan Oymak, Taylan Edis, Ulaş Yıldırım, Gizem Demir, Görkem İzel Şimşek, Bahar Aslan for their support and work with me any time.

TABLE OF CONTENTS

LIST OF TABLES

TABLES

LIST OF FIGURES

FIGURES

LIST OF ABBREVIATIONS

ABBREVIATIONS

CTAB: Cetyltrimethylammonium Bromide

EDTA: Ethylenediaminetetraacetic Acid

FT-IR: Fourier Transform Infra-Red

PBS: Phosphate Buffered Saline

RE: Rare Earth

SEM: Scanning Electron Microscope

UV-VIS: Ultra Violet-Visible

XRD: X-Ray Diffraction

PL: Photoluminescence

TGA: Thermal Gravimetric Analysis

DTA: Differential Thermal Analysis

PEG: Polyethylene Glycol

RTM: Real-Time Monitoring

DLS: Dynamic Light Scattering

HAP: Hydroxyapatite

CHAPTER 1

INTRODUCTION

1.1 Borates

Inorganic boron oxygen compounds are materials that do not contain organic groups, are dominated by B-O bonds and include product groups such as borates, perborates, boron trioxide, boric acid or boron phosphate. Borates are the leading compounds among inorganic boron-oxygen products. Their structure always contains at least one boron oxo anion (BO_3^{3-}). Most of the boron minerals belong to the borates group. The most used boron products in the industry are borates.

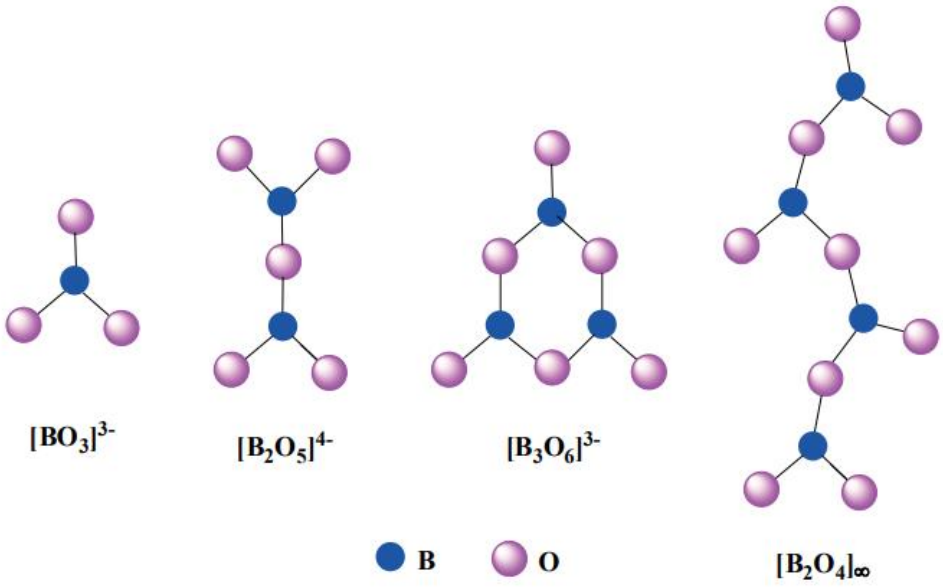

Figure 1: Coordination of some borates compounds

Chemically, borates are salts or esters of boric acid. More than two hundred crystalline borate minerals are recognized, as well as several hundred synthetic borate derivatives and some of them can be seen in **Figure 1**. The molecular/crystal structures of most of them have been studied. Borate crystal structures are quite

complex. This may be because boron is electron deficient. Almost all boron minerals found in nature contain the boron-oxygen (B-O) moiety. The only oxidation number that boron can perform in its compounds is +3, but due to the high energy of the first three ionizations, the B^{3+} ion is not formed. Instead, complex shapes (rings, cages, clusters, network systems) are formed using covalent bonds. In the crystal structure of borates, their structures usually show three-bonded (trigonal, coordination number three) BO_3 groups or tetrahedral (tetrahedral, coordination number four, negatively charged) BO_4 groups (e.g. $B(OH)_4^-$) or combinations (Yünlü, 2016).

There are many ways to synthesize borates. Solid-state, and water-assisted are two of these ways (Celik et al., 2017). One of the most important methods developed for nano-sized borates is the sol-gel process. The sol-gel process consists of hydrolysis and condensation steps. In the sol-gel method, an alkoxide stable solution is formed and this is called sol. A gel network is formed by polycondensation. The sol-gel process is completed by dehydration and decomposition of the gel. Pechini has developed a modified sol-gel method for metal elements that are difficult to hydrolyze. Complex structures formed with chelating agents bind with polyalcohols and initiate the esterification reaction. This esterification causes the solution to gel over time. After burning the organic molecules in the gel, agglomerated nano- or micron-sized particles are usually obtained. (Chung, 2010). Ranjeh et al. use Cu_2O/Li_3BO_3 and CuO/Li_3BO_3 borates in the photocatalytic degradation of dye. They used the Pechini sol-gel method in their studies. While making this synthesis, they examined how different chelating agents affect the morphology and size of the mole ratios and structures of the gel agents. In experiments with EDTA, citric acid, tartaric acid and phthalic acid, they obtained fine nanoparticles with EDTA, plate-like structures with citric acid, short nanorods with tartaric acid and microsphere crystals with phthalic acid (Ranjeh et al., 2020).

Borates are an important part of solid-state chemistry due to their functionality. Borates have attracted the attention of researchers due to their complex structure. Since there are many modes of B-O bonding and their association with metals, borates have a wide range of applications as optical materials. Since borates are

highly efficient in performance, they are used as novel optical materials. Therefore, they are UV and deep UV optical materials. The noncentrosymmetric structure, large optical transmittance, high temperature and chemical stability, and large polarization make borates a candidate for optical materials (Mutailipu et al., 2021).

1.1.1 Crystal Structure of GdB_3O_6 and $GdBO_3$

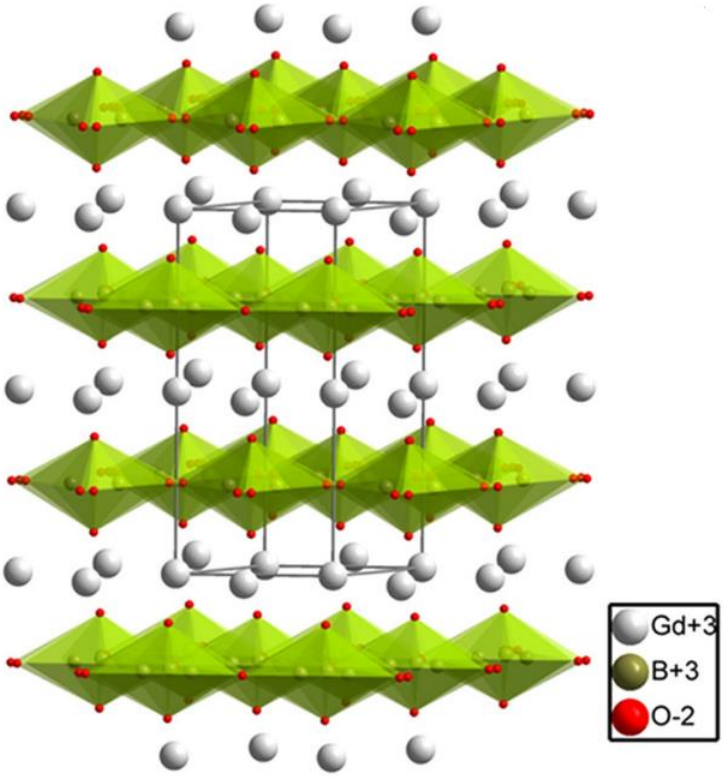

Figure 2: Crystal structure of hexagonal $GdBO_3$

$GdBO_3$ has three different crystal systems. These are monoclinic, hexagonal and P_1triclinic systems. Hexagonal $GdBO_3$ in **Figure 2** has lattice parameters a=b=5.28 Å and c=6.52 Å and $\alpha=\beta=90°$ $\gamma=120°$ (P. Wang et al., 2014). In addition, BO_3 compounds can be called aragonite, calcite and vaterite in terms of structure. Aragonite and calcite-type BO_3 structures contain only BO_3 groups in their unit cells. Vaterite-type BO_3 structures contain the $B_3O_9^{9-}$ ring. Vaterite contains trigonal planar BO_3 and tetrahedral BO_4 units due to the opening of the B_3O_9 ring (Seraiche

et al., 2020). In 2016, Severoğlu investigated the optical properties of vaterite type Dy^{3+}, Sm^{3+} and Tb^{3+} doped with a tetrahedral crystal system (Severoğlu, 2016). Then, Akman et al. made SiO_2 coating by utilizing the optical properties of Ce^{3+} and Tb^{3+} doped $GdBO_3$ particles and investigated the loading and release properties of the drug celecoxib (Akman et al., 2020). Later, Taneroğlu synthesized vaterite-type $GdBO_3$ particles doped with Eu^{3+} in 2020 and investigated the optical properties of Europium in the $GdBO_3$ host (Taneroğlu, 2020). İçten et al. synthesized magnetic nanocomposite. They reported that there are different crystal systems in synthesis made with boric acid and borax. They reported that they obtained hexagonal vaterite type $GdBO_3$ with boric acid and triclinic-$GdBO_3$ borate with borax (Icten et al., 2017).

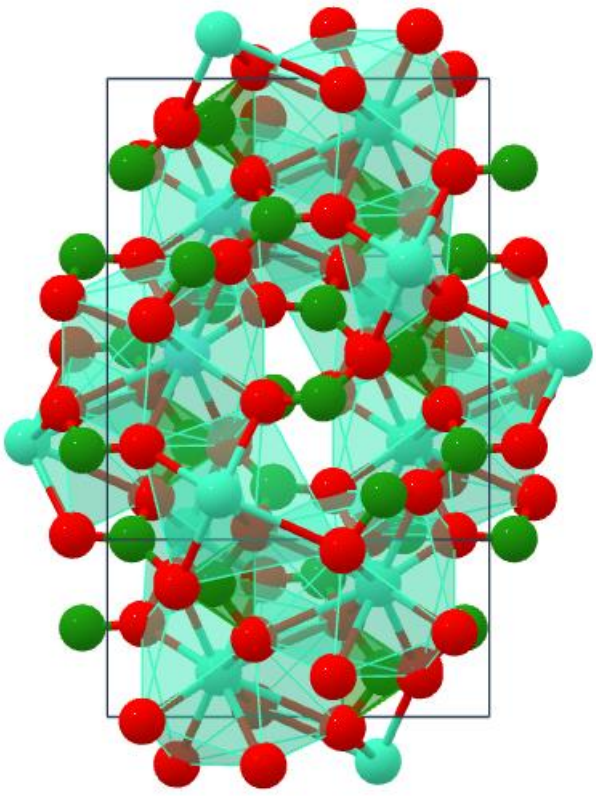

Figure 3: Crystal structure of monoclinic GdB_3O_6

Gadolinium triborate is a borate compound that currently has two different crystal systems. These are orthorhombic and monoclinic crystal systems. Schmitt et al. studied the β-$Gd(BO_2)_3$ phase and it has a Pnma space group with an orthorhombic crystal system. Lattice parameters were determined as a=15.886 , b=7.3860 and c=12.2119 Å (Schmitt & Huppertz, 2017). On the other hand, Mukherjee et al. synthesized a triborate structure with lattice parameters a=9.83, b=8.15 and c=6.31 Å belonging to the C2/c space group with monoclinic crystal system which is represented in **Figure 3** (Mukherjee et al., 2017). In these studies, they stated that the structure consists of trigonal planar BO_3 and tetrahedral BO_4 groups. The importance of these structures and their various combinations are important for UV absorption. Li studied the UV absorption of different borates in his work and this publication examined in detail in results and discussion section (Li, 1989).

1.2 Luminescence

Light displays wave and electromagnetic properties together. Maxwell proved that light has electromagnetic properties (Fujiwara, 2003). The interaction of light and solid-state materials can be broadly classified as reflection, transmission and propagation. When the lights hit the surface of the materials some of it is reflected and the rest propagates through the optical medium. While propagation some of it may be reflected and the remainder will be transmitted. Phenomena such as refraction, absorption, luminescence, scattering and non-linear optical effects occur when the light propagates into the optical medium. Refraction causes light to travel slower than free space. Refraction does not affect the intensity of the light. Scattering is a phenomenon in which light changes its direction and frequency depending on the situation. If the frequency of the light does not change, it is elastic scattering, if it does, it is called inelastic scattering. Free carriers in the atom or the transition frequency of atoms resonate with light during propagation, and absorption occurs. Absorption can excite electrons electronically, vibrationally and rotationally according to the spectrum of light. Photoluminescence is called the transition of the

incoming electromagnetic wave to a lower electronic energy level by being excited by spontaneous emission (Mark Fox, 2010). There are also different ways to achieve luminescence. One of them is radioluminescence obtained by radiation such as x-rays. Another one is thermoluminescence that is obtained by heat. Chemiluminescence is obtained by chemical reactions, mechanically excitable triboluminescence is possible and ultrasound-induced sonoluminescence is one of the ways to obtain luminescence (Obodovskiy, 2019).

1.2.1 Photoluminescence

Photoluminescence is a type of luminescence obtained by the re-emission of absorbed light by spontaneous emission. Einstein suggested an equation to explain the spontaneous emission rate. The spontaneous emission rate is important because the shape of the emission band changes depending on the thermal distribution.

$$W_{u \to l} = A_{l,u} N_u \qquad (1.1)$$

In the equation, "W" indicates the spontaneous emission rate, "u" indicates the higher energy level and "l" indicates the lower energy level. "$A_{l,u}$" represents the Einstein coefficient of spontaneous emission and "N_u" defines the number of molecules at the high energy level (Peter Atkins et al., 2018).

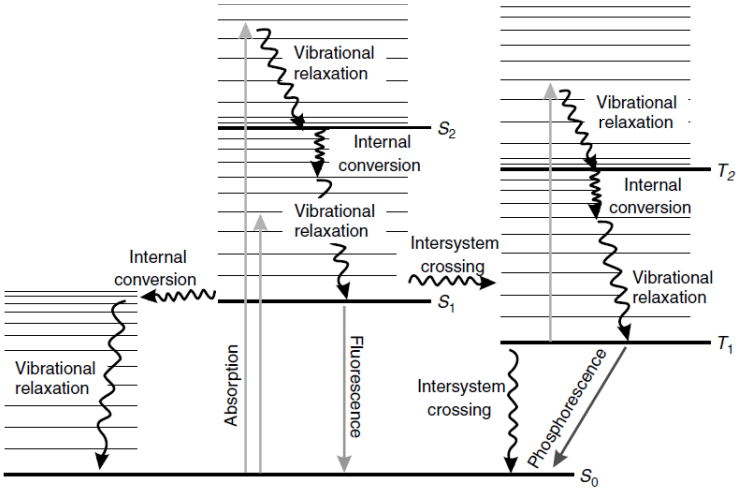

Figure 4: Alexander Jabłoński Diagram

The electronic energy levels exist as a singlet state when spin is paired and a triplet state when spin is unpaired. Higher electronic energy levels can be denoted as S_1, S_2, T_1 and T_2. Emissions cannot always be observed as radiative decay. They can also lose their energy as non-radiative decay. Jabłoński explained the reasons for Stokes's shifts in **Figure 4**. Absorbed energy can be lost non-radiatively by vibrational relaxation, internal conversion, and intersystem crossing (Sauer et al., 2011).

The emission of photoluminescence is divided according to lifetime. These are called fluorescence, phosphorescence and persistent. Fluorescence can last up to 10 ns while phosphorescence can last up to 10 s. Moreover, persistent luminescence is also radiative decay, where emission can last from minutes to hours (Noto et al., 2016). The difference between fluorescence and phosphorescence can be understood by looking at the Jabłoński diagram because the spin state changes singlet state to triplet state and if the molecule emits singlet to ground state called fluorescence and triplet to ground state called phosphorescence. This explains why the phosphorescence lifetime is longer than the fluorescence lifetime (Valeur & Berberan-Santos, 2011).

1.2.1.1 Quantum Yield

Quantum yield and lifetime are one of the most important distinctive properties of optical solids. Single-molecule fluorophores with high quantum yields such as rhodamine dyes exhibit high photoluminescence intensity (Kubin & Fletcher A.F, 1982). Since quantum yield is the ratio of the emitted photon to the absorbed photon, it is expressed as in the equation below.

$$\eta = \frac{N(emitted)}{N(absorbed)}$$

Quantum yield can approach its maximum value if there is no non-radiative decay (Lakowicz, 2006). It is possible to calculate the quantum yield of a system using either the absolute or the relative method. There are three different techniques available for the absolute method. (1) integrating sphere, (2) calorimetric method,

and (3) thermal lens spectroscopy. Integrating sphere is a spherical device with a highly reflecting surface. Luminescent particles are placed in the integrating sphere with a right-angle geometry. Refractive index, polarization and spatial anisotropy corrections eliminate with the integrating sphere method. The relative method requires a reference standard with a known quantum yield. Identical measurement conditions such as the same excitation power and wavelength between the sample and the reference are needed for the relative method. The refractive index of the sample and the reference are required for the relative method (Fontes & Santos, 2020).

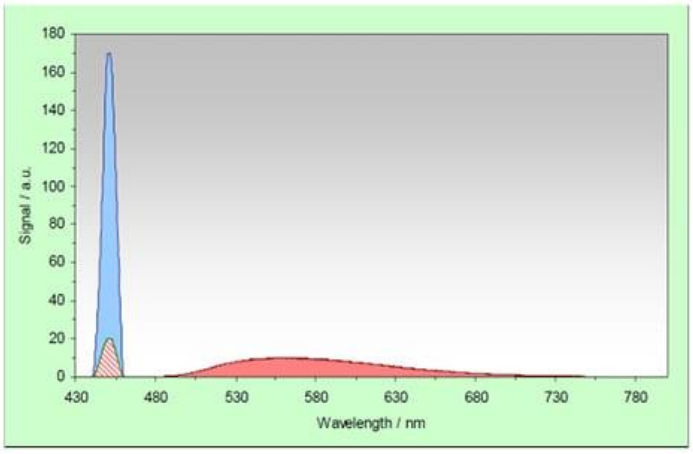

Figure 5: Quantum yield calculations with absolute method

In this study, the quantum yield was calculated with the absolute method. The measurement is carried out with highly reflective material. The blue area represents the reference material reflection which has %100 reflection and the red hatched area in the excitation region defines the reflection of the sample in **Figure 5**. Their difference is equal to absorption. The red area in the emission range is the emission of the sample and dividing the emission area by the reflection difference gives the quantum yield.

$$\eta = \frac{Red\ area}{Blue\ area - Red\ hatched}$$

1.2.1.2 Decay Lifetime

The average time a molecule spends from an excited state to spontaneous emission is called a lifetime. It can be denoted as given equation.

$$\tau = \frac{1}{k_f + k_{nr}}$$

Where k_f is the rate for fluorescence and k_{nr} is the rate for non-radiative decays. Since the fluorescence intensity is proportional to the excited electrons, the first-order rate equation can also be expressed as

$$I(t) = I_0 e^{-(\frac{t}{\tau})}$$

As the number of excited electrons is directly proportional with fluorescence intensity I(t). Integration between t=0 and t yields determines single exponential decay. Not every molecule needs to obey the single exponential decay. If the molecule exhibits extrinsic luminescence, higher orders may be required due to geometry and coordination. High-order exponential decay can be denoted as a given equation (Sauer et al., 2011).

$$I(t) = \sum_i I_i e^{-(\frac{t}{\tau_i})}$$

1.3 Luminescent Rare Earth Elements

Lanthanide chemistry began with discovery of the gadolonite by Johan Gadolin in 1794. Later, with the discovery of other rare earth minerals, lanthanides found their place in the periodic table. Although lanthanides are called rare earth elements, they are not very rare and generally lighter lanthanides are more abundant in nature than heavier ones (Cotton, 2006).

Due to their unique properties, rare earth elements can be used in many fields, from super magnets to fluorescent lamps, and solar cells to biological applications

(Balaram, 2019). One of the biggest factors behind their unique properties is the empty 4f orbital and that are shielded by the 5s and 5p orbitals. Lanthanide ions can make intra-4f and 4f-5d transitions. Since they are well shielded, they are not much affected by the crystal field effect. The 4f electrons are not involved in chemical bonding, so the emission from their energy level does not change much (Gai et al., 2014).

The energy levels of lanthanides can be expressed in atomic term symbols. Absorption and emission between rare earth ions can be explained by allowed and forbidden transitions between these energy levels (Pawade et al., 2019). Dieke (Dieke & Satten, 1970) studied the electronic energy levels of rare earth ions in $LaCl_3$ crystal and showed the energy levels in the graph as follows.

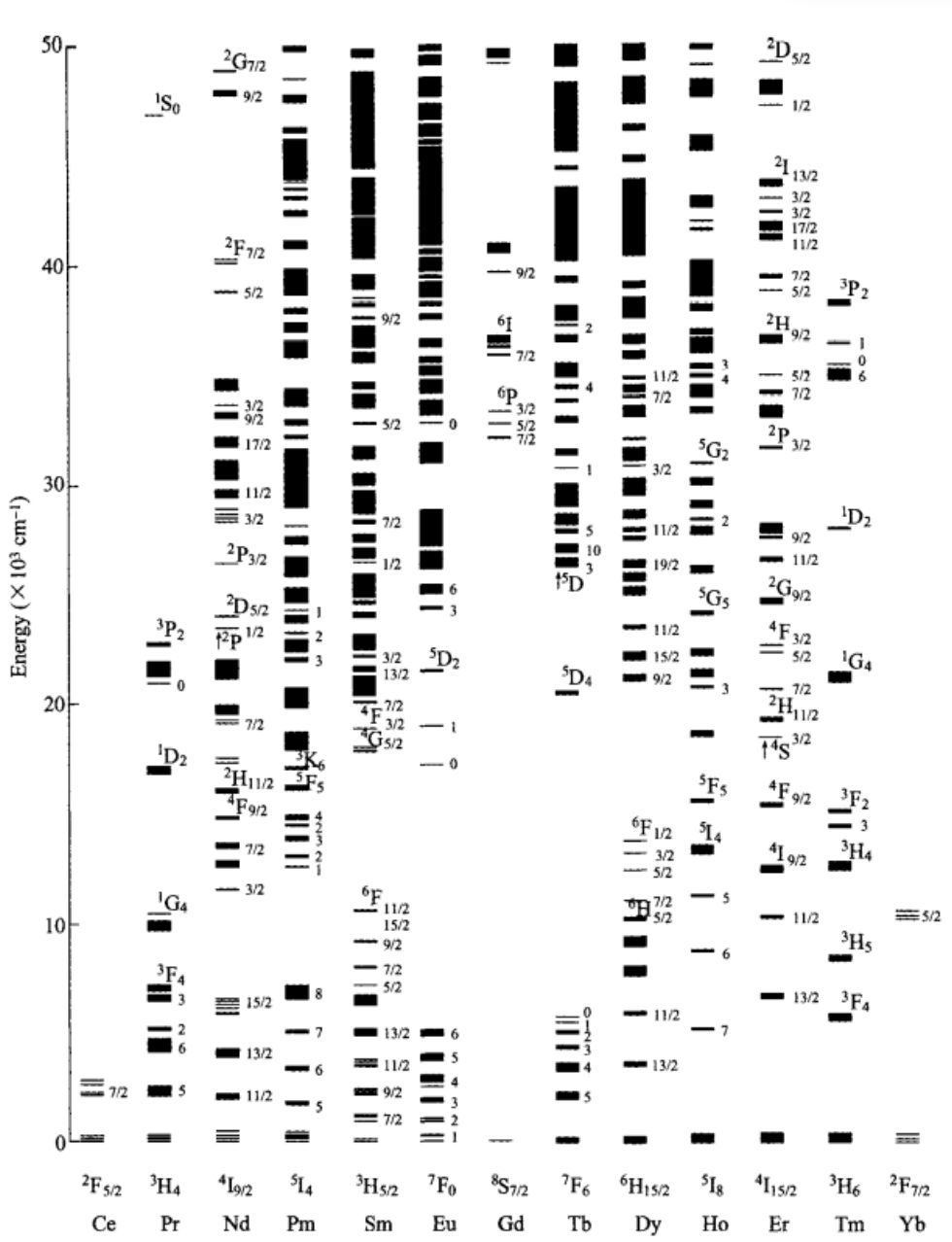

Figure 6: Dieke Diagram for trivalent rare earth ions

1.3.1 Gadolinium

Gadolinium is the 8th element in the lanthanide series and has the electron configuration of [Xe] $4f^7\ 5d^1\ 6s^2$ (Pawade et al., 2019). The ground state term symbol of Gadolinium is $^8S_{7/2}$. Because of its high first excitation transition, rare earth

elements can be doped into the Gadolinium host, allowing them to energy transfer mechanisms or receive the desired emission (Dieke & Satten, 1970). This can be seen in **Figure 6** (Liu & Jacquier, 2005). Meng et al. studied the energy transfer mechanism between Gadolinium ion and Europium and the emission of Eu^{3+} ion was investigated. In the study, the $^{8}S_{7/2}$ to $^{6}I_{7/2}$ transitions excitation value of the Gd^{3+} ion was calculated as 272 nm. When the lifetime behaviour was examined, it was determined that the lifetime of gadolinium ion decreased as the Eu^{3+} concentration increased and energy transfer was observed (Meng et al., 2012).

Another advantage of Gadolinium is that it can be used in magnetic and optical imaging strategies. Due to the paramagnetic properties of the Gd^{3+} ion, it can be used as a magnetic resonance imaging agent, while its optical properties allow it to be used in optical imaging (Ortega-Berlanga et al., 2021). The 7 unpaired electrons in the 4f orbital of gadolinium show paramagnetic properties. Gadolinium contrast agents decrease the longitudinal relaxation time and can provide brighter and better-focused magnetic resonance imaging images due to their high magnetic moment and long electron spin relaxation time (Chanana et al., 2022). Guleria et al. used the Gd_2O_3 molecule as a T_1-T_2 dual-mode MRI contrast agent and investigated the effect of polyols on the system (Guleria et al., 2019). Gadolinium was used as a contrast agent for computed tomography in an individual with dysphasia (Esmail & Rafiq, 2019).

1.3.2 Cerium-Terbium

Green-emitted white light diode has attracted intense interest as an optical material by many researchers. The Terbium ion itself is a rare earth element with emission in the green zone with $^{5}D_3$ or $^{5}D_4$.to $^{7}F_j$ (j=0-6) transitions. Since forbidden f-f transitions show weak and narrow excitation, Terbium ion used as an activator for green light emission which can be co-doped with cerium ion as a sensitizer to increase the luminescence intensity. The intensity of Terbium ion can be increased by the spin exchange mechanism by exciting the Cerium ion (Guan et al., 2016).

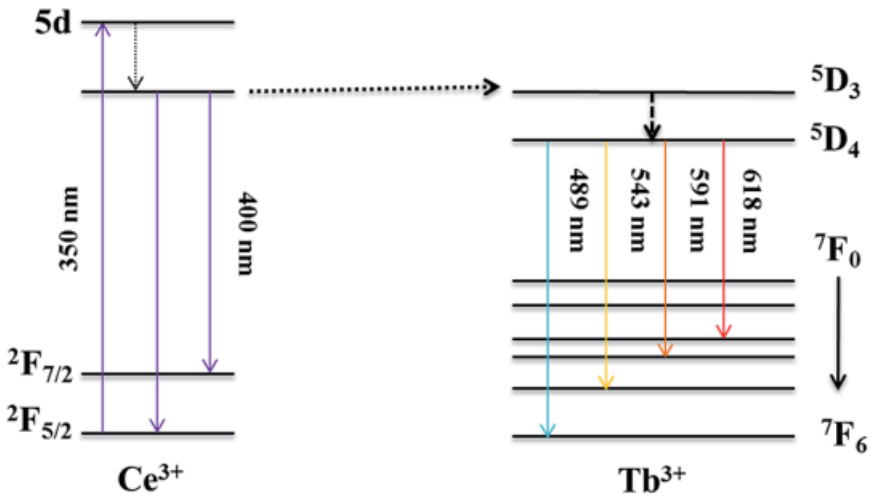

Figure 7: Energy transfer mechanism between Cerium and Terbium trivalent ions

In **Figure 7**, the energy transfer mechanism between the Cerium and Terbium ions is given. Maggay and coworkers observed that when Cerium ion was used as a sensitizer and Terbium ion was used as an activator, the luminescence intensity was higher than the emission with Terbium ion alone. (Maggay et al., 2015).

1.3.3 Europium

Europium ions are phosphors that can be excited by UV radiation that is used for red light emissions. Europium trivalent ion has the configuration [Xe]$4f^6$. The $4f^6$ configuration can be expressed with the 119 atomic term symbols. Many Eu^{3+} ions show luminescent character due to the $^5D_0$ to ^7F_j transition. **Table 1** shows the expected transitions and emission values for the Eu^{3+} ion.

Table 1: Expected emissions from trivalent Europium ion

Transition	*Wavelength Range (nm)*
$^5D_0 \rightarrow {}^7F_0$	570-585
$^5D_0 \rightarrow {}^7F_1$	585-600
$^5D_0 \rightarrow {}^7F_2$	610-630
$^5D_0 \rightarrow {}^7F_3$	640-660

$^5D_0 \rightarrow {}^7F_4$	680-710
$^5D_0 \rightarrow {}^7F_5$	740-770
$^5D_0 \rightarrow {}^7F_6$	810-840

The reason the energy values in emissions increase as the J line increases is explained by the Lande interval rule. Lande stated that the difference between energy levels is directly proportional to the total angular momentum value (Binnemans, 2015). Cui and coworkers studied Europium-doped $GdBO_3$ particles and emphasized that the ideal phosphor should be homogeneous, and the polydispersity index should be low. In their experiments, they compared the stirred tank reactor (STR) with the rotator-packed bed reactor (RPB) and observed that the doped ion distribution was more uniform in the RPB reactor. In line with these results, it was observed that the luminescence intensity of the particles synthesized in the RPB reactor was higher than the STR (Seraiche et al., 2020b). In another study, Huy et al. reported that Sr_2YF_7 particles doped with Yb^{3+}, Er^{3+} and Eu^{3+} ions, increased the power conversion efficiency by up to 20.9% by using both up conversion and down conversion in their solar cell devices (Huy et al., 2022).

1.4 Drug Delivery

Drug delivery has been studied for more than 60 years. During this time many methods have been developed for drug delivery systems. Before 1950, all drugs were available as pills and in contact with water the entire drug was released before release could be controlled. In 1952 Lee developed a formulation that could release for 12 hours (Lee & Li, 1952). Over time, different drug delivery systems have been developed as sustained release, timed release, extended release etc. Drug delivery systems can generally be divided into three generations. The first generation is the generation in which oral and transdermal dosages were developed between 1950 and 1980. Different release formulations have been developed in this period. The most widely used of these were diffuse and dissolution controlled. The second generation

covers the period between 1980 and 2010. The second-generation drug delivery systems struggled with more complicated release profiles than the first-generation. The second generation developed smart delivery systems based on the development of control systems in the first generation. For example, biodegradable polymer-based poly(lactic-co-glycolic acid) systems with prolonged release were studied (Ye et al., 2010). The third generation drug delivery systems continue to develop to eliminate deficiencies in the former two generations. This generation is called modulated delivery system. The problems in the third generation are the delivery of drugs such as low water solubility, being targeted, crossing the brain-blood barrier and being non-toxic. In addition, control of drug loading and release kinetics can be added to the expectations from the third generation (Yun et al., 2015).

Nanoparticles can penetrate the cell more easily than large molecules with their physicochemical and biological properties. Due to these properties, they can be used in drug delivery systems. Conjugation between the drug and the loaded nanoparticle is very important for targeted therapy. In the strategies used in drug delivery systems, molecules that can establish a relationship between the ligand and problematic cells are used for targeted therapy, while drug release can also occur with physical stimuli such as temperature, pH, and magnetism. The main goal of these systems is to induce drug release in the problem cell. In drug delivery systems, nanoparticles must be biocompatible and non-toxic. (Wilczewska et al., 2012).

1.4.1 Hydroxyapatite

Hydroxyapatite is an inorganic compound with the formula $Ca_{10}(PO_4)_6(OH)_2$. Hydroxyapatite is the most abundant mineral in bones and teeth. For this reason, it is used in osteoinductive and regeneration areas. In addition to these properties, hydroxyapatite is also widely used in drug-delivery systems. Being a biocompatible material allows it to overcome biological barriers. Many vitamins, hormones, antibiotics and anticancer drugs can be transported with this drug delivery system (Munir et al., 2021).

Hydroxyapatite can be synthesized by many methods. As a general structure, it is possible to synthesize it by dry, wet, and high-temperature methods. The synthesized hydroxyapatite may have different morphology, size, and crystal phases according to the synthesis method (Mohd Pu'ad et al., 2019). It is also possible to coat synthetic hydroxyapatite on metal surfaces or nanoparticles. Mondal et al. studied cancer treatment by coating iron oxide particles with hydroxyapatite. Iron oxide particles are used in magnetic hyperthermia treatment because they generate heat under an alternating magnetic field, but since iron is a redox center in Fe_3O_4 particles, they create oxidative stress in the cell and have detrimental effects such as reactive oxygen species and hydrogen peroxide. For this reason, Fe_3O_4 nanoparticles are coated with hydroxyapatite to avoid these effects. Hydroxyapatite was synthesized by the wet precipitation method and calcium nitrate tetrahydrate and diammonium hydrogen phosphate were used as precursors (Mondal et al., 2017).

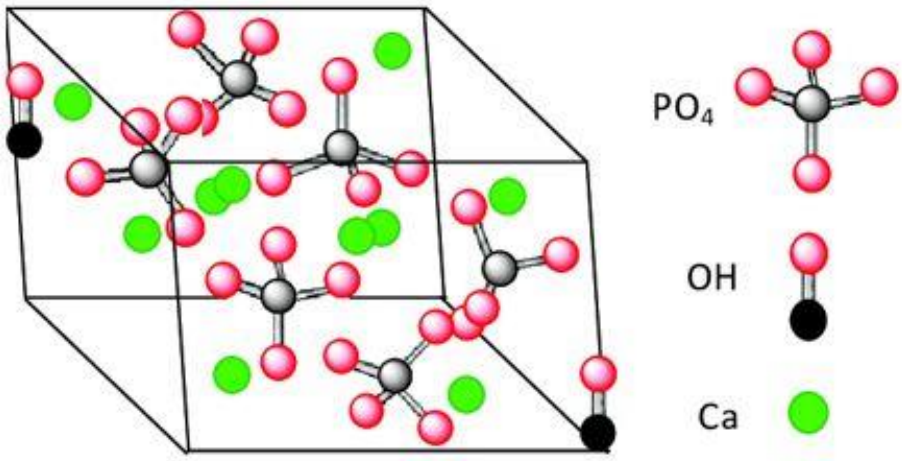

Figure 8: Crystal structure of hydroxyapatite

The crystal structure of hydroxyapatite can be seen in **Figure 8**. Hydroxyapatite with a hexagonal structure belongs to the $P6_3$ space group. Lattice parameters were a=b=9.55 Å, c=6.92 Å and $\alpha=\beta=90°$, $\gamma=120°$. Hydroxyapatite, which does not

interact magnetically, is a good drug delivery candidate with hydroxyl groups in its structure (Rujitanapanich et al., 2014). In drug delivery systems, drugs can be loaded into the drug carrier by different mechanisms. These can occur by sorption, chemical bonding or mechanical aspects. In the strategies developed in recent years, intermolecular forces can be used as a strategy between the drug and the carrier. With a basic strategy, the carrier and the drug can be attached by this method and the sorption mechanism is activated. Hydroxyapatite interacts with the drug as an active site with the -OH groups in its structure and the drug is loaded onto the hydroxyapatite (Loca et al., 2015). Drugs are loaded by mixing on colloidally stable particles in a certain time interval and this loading and release may vary depending on the structure and geometry of the material (Čolović et al., 2012).

1.4.2 PEGylation

PEGylation or coating the surface with PEG is one of the methods often used in drug delivery systems to improve efficiency. PEGylation increases circulation time by reducing protein deposition and decreases immunogenicity. PEGylation prevents aggregation by protecting the surface and increases systematic circulation time (Suk et al., 2016). Gref et al. were the first group to introduce PEGylated nanoparticles. They observed that nanoparticles increase circulation time and at the same time decreased liver uptake compared to non-PEGylated ones (Yun et al., 2015). PEG is used in studies due to its non-toxic, non-immunogenetic, and non-antigenic properties. At the same time, it prevents the dispersion of nanoparticle surfaces and non-specific protein adsorption (Venkatasubbu et al., 2013).

Khanh et al. examined the cellular effects of PEGs with 11 different molecular weights in their studies. In their experiments with PEG 200, 400, 600, 1000, 1500, 1500, 4000, 8000, 10000, 12000 and 20000, they observed that low molecular weight decreased cell viability, whereas high molecular weight had a limited effect on cell viability (le Khanh et al., 2022).

1.4.3 Real-Time Monitoring

Recently, inorganic nanocarriers with fluorescent properties have been investigated by researchers to monitor drug loading and release properties. Drug monitoring is important to get rid of excess drug side effects such as toxicity, damage to the immune system. Moreover, fluorescent imaging is a low-cost, highly selective, sensitive, and non-destructive method, which make it easier to use. For these reasons, fluorescent trackers have attracted the attention of researchers for theranostics and have become a good candidate for real-time monitoring in drug delivery systems (Fan et al., 2018). However, fluorescent nanocarriers have a few limitations. Absorption at low wavelengths limits fluorescent trackers. Wavelengths between 600-1100 nm are considered to be the “optical window” and the range in which biological cells, hemoglobin and deoxyhemoglobin in blood have the lowest absorbance (Tian et al., 2012).

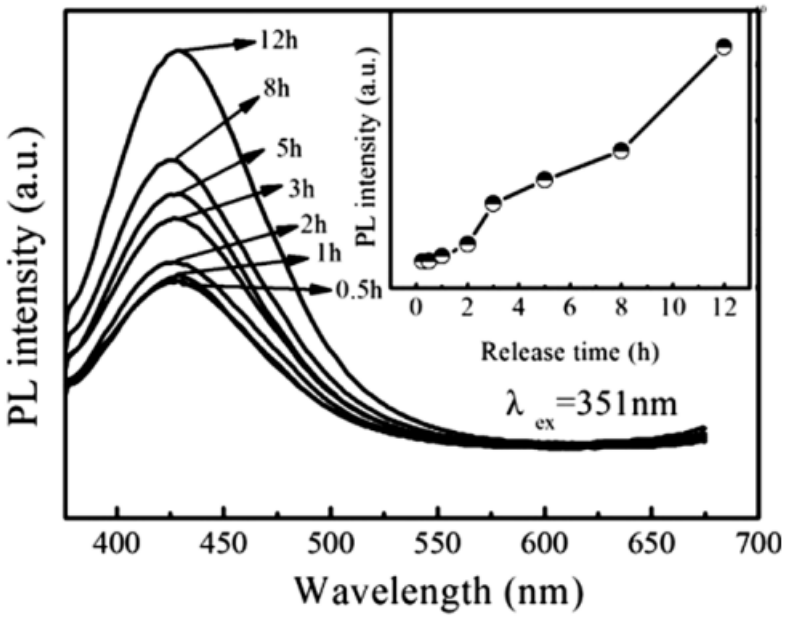

Figure 9: Photoluminescence intensity as a function of cumulative release

Jiang et al. synthesized strontium-doped hydroxyapatite microspheres by hydrothermal method. They prepared hydroxyapatite particles and used vancomycin as a model drug in drug delivery systems. In their studies, they found that morphology, luminescent intensity, drug loading and release profile were related to the amount of strontium. Then, they followed the cumulative release of vancomycin with luminescence intensity and followed the luminescence changes over time in **Figure 9** (Jiang et al., 2014).

Aim of the Study

This thesis study aimed to develop luminescent nanoparticles that can perform real-time monitoring as well as deliver drugs. In this context, the following objectives were aimed to be accomplished:

- To synthesize and characterize $Ce^{3+/}Tb^{3+}$ codoped GdB_3O_6 with different chelating agents and surfactant to see the effect on the crystal structure and photoluminescence intensity in $Gd_{0.95}Ce_{0.025}Tb_{0.025}B_3O_6$ particles.
- To synthesize and characterize Eu^{3+} doped GdB_3O_6 with different dopant ratios to see concentration quenching and how dopant ratio affects the crystal structure.
- To synthesize and characterize the Eu^{3+} doped $GdBO_3$ particles to compare photoluminescent properties with the Eu^{3+} doped GdB_3O_6.
- To coat the particles with hydroxyapatite and PEG to increase the drug loading capacity and circulation time.
- To study drug loading and release profiles of the particles.
- To perform real-time monitoring studies using the optical properties of the particles.

CHAPTER 2

MATERIALS AND METHODS

2.1 Materials

The chemicals used in our studies are listed in **Table 2**

Table 2: Material used for the synthesis of core and shell nanoparticles

Material	Molar Mass (g/mol)	Brand
Gadolinium Oxide Gd_2O_3	362.5	Acros Organics
Europium Oxide Eu_2O_3	351.93	Aldrich
Cerium Carbonate $Ce_2(CO_3)_3$	460.27	Aldrich
Terbium Oxide Tb_4O_7	747.69	Aldrich
Boric Acid H_3BO_3	61.83	Merck
Ethylene diamine tetra Acetic Acid (EDTA) $C_{10}H_{16}N_2O_8$	292.24	Sigma
Cetyltrimethyl Ammonium Bromide $C_{19}H_{42}BrN$	364.45	Sigma
Phthalic Acid $C_8H_6O_4$	166.14	Merck
Tartaric Acid, $C_4H_6O_6$	150.087	Sigma

Table 2 (cont'd)

Glycine $C_2H_5NO_2$	75.07	Sigma
Calcium Nitrate Tetrahydrate $CaH_8N_2O_{10}$	236.15	Sigma
Diammonium Hydrogen Phosphate $(NH_4)_2HPO_4$	132.06	Merck
Ammonium Hydroxide NH_4OH	35.04	Sigma
Citric Acid $C_6H_8O_7$	192.124	Sigma Aldrich
Nitric Acid (%65) HNO_3	63.01	Merck

2.2 Synthesis

2.2.1 Synthesis of rare earth doped GdB_3O_6 and $GdBO_3$

To improve the optical properties of phosphors, the advantageous features of the sol-gel process were utilized. First of all, it is foreseen that in order to obtain a smaller particle size, it is necessary to avoid agglomeration of the material. For this purpose, different chelating agents were used during the synthesis. Oxides of rare earth element ions to be used during the synthesis were utilized as starting material. The oxides were then converted into nitrate salts with nitric acid to make them soluble in water because the solvent in the solution in the sol-gel process is water. A stoichiometric amount of nitric acid was added to the rare earth oxides and stirred at 80 °C. The nitrate salts were added to 0.80 g boric acid (H_3BO_3), cationic surfactant

CTAB or chelating agents (EDTA, citric acid, glycine, tartaric acid, phthalic acid) and water prepared in a stoichiometric ratio. 200 mL of solution was stirred at 80 °C until the dark resin was obtained. Ce^{3+}/Tb^{3+} codoped GdB_3O_6 synthesis was calcinated at 900 °C for all different chelating agents and surfactant in **Table 3**.

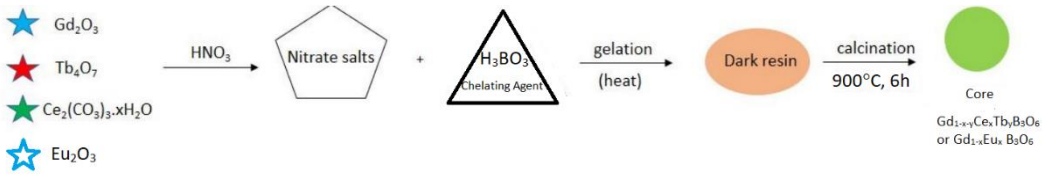

Figure 10: Synthesis scheme of GdB_3O_6

For instance, synthesis of $Gd_{0.95}Ce_{0.025}Tb_{0.025}$ was started with 0.59 g Gd_2O_3, 0.022 g $Ce_2(CO_3)_3$ and 0.036 g Tb_4O_7. Rare earth oxides were nitrated with 10 mL of nitric acid. 0.80 g boric acid, 0.51 g CTAB stirred with 200 mL water. When the solution was heated to 80 °C. Rare earth nitrates were added to the solution. After the dark resin was obtained while stirring at 80 °C. The resin was calcinated at 900 °C for 6 hours. Stoichiometric amounts of doped ions can be seen in **Table 6**. Then, after obtaining the optimum condition, Eu^{3+} doped GdB_3O_6 particles were synthesized according to the ratio in **Table 4**. The same conditions were applied to Eu^{3+} doped $GdBO_3$. Nitrate salts and boric acid prepared in the stoichiometric ratio were calcined at 800° for 3 hours for the synthesis of $GdBO_3$ after the stoichiometric addition of the CTAB. Prepared stoichiometric ratios of Eu^{3+} doped $GdBO_3$ can be seen in **Table 5**.

Table 3: Amount of chelating agent and surfactant for synthesis of GdB_3O_6 structure

Chelating Agent (mol ratio)	**Amount (g)**
CTAB %40	0.51
CTAB %60	0.77
CTAB %80	1.02
CTAB %160	2.04
EDTA %40	0.51

Table 3 (cont'd)

Citric Acid %40	0.27
Glycine %40	0.11
Tartaric Acid %40	0.21
Phthalic Acid %40	0.23

Table 4: Amount of oxides for the synthesis of GdB_3O_6 structure

	Amount of Gd_2O_3 (g)	**Amount of Eu_2O_3 (g)**
GdB_3O_6	0.63	
$Gd_{0.99}Eu_{0.01}B_3O_6$	0.62	0.006
$Gd_{0.97}Eu_{0.03}B_3O_6$	0.61	0.018
$Gd_{0.95}Eu_{0.05}B_3O_6$	0.59	0.030
$Gd_{0.93}Eu_{0.07}B_3O_6$	0.58	0.043
$Gd_{0.90}Eu_{0.10}B_3O_6$	0.57	0.06
$Gd_{0.875}Eu_{0.125}B_3O_6$	0.55	0.075
$Gd_{0.85}Eu_{0.15}B_3O_6$	0.54	0.09
$Gd_{0.825}Eu_{0.175}B_3O_6$	0.52	0.105

Table 5: Amount of oxides for the synthesis of $GdBO_3$ structure

	Amount of Gd_2O_3 (g)	**Amount of Eu_2O_3 (g)**
$GdBO_3$	0.84	
$Gd_{0.99}Eu_{0.01}BO_3$	0.83	0.008
$Gd_{0.96}Eu_{0.04}BO_3$	0.80	0.03
$Gd_{0.93}Eu_{0.07}BO_3$	0.77	0.05
$Gd_{0.90}Eu_{0.10}BO_3$	0.76	0.08
$Gd_{0.875}Eu_{0.125}BO_3$	0.74	0.1
$Gd_{0.85}Eu_{0.15}BO_3$	0.71	0.12
$Gd_{0.825}Eu_{0.175}BO_3$	0.69	0.15
$Gd_{0.80}Eu_{0.20}BO_3$	0.67	0.17

Table 6: Amount of oxides for the synthesis of Ce^{3+}/Tb^{3+} doped GdB_3O_6 structure

	Amount of Gd_2O_3 (g)	**Amount of $Ce_2(CO_3)_3$**	**Amount of Tb_4O_7 (g)**
$Gd_{0.95}Ce_{0.025}Tb_{0.025}B_3O_6$	0.59	0.022	0.036

2.2.2 Hydroxyapatite coating and PEGylation

Hydroxyapatite was synthesized on the core as a shell to improve drug loading capacity. The wet precipitation method was used to synthesize hydroxyapatite. Calcium nitrate tetrahydrate and diammoniumhydrogen phosphate and ammonium hydroxide were used as precursors.

First, 0.5 grams of nanoparticles were dispersed into 0.06 M $Ca(NO_3)_2.4H_2O$ solution and stirred for 1 hour. Then 0.07 M $(NH_4)_2HPO_4$ solution was slowly added into the solution and pH was kept constant with NH_4OH at pH 9. After the particles were mixed for 2 hours, then the coating process was completed by calcining at 600° for 2 hours.

PEGylation was performed at 2% and 100 mg nanoparticles were mixed with 2% PEG with a molecular weight of 10000 for 24 hours. The solution was then centrifuged and dried in a freeze-dryer for 1 day.

2.2.3 Doxorubicin Loading and Release

Doxorubicin hydrochloride was used as a model drug. In order to investigate drug storage and release, calibration curves were first prepared. The prepared 1000 ppm (1 mg/mL) doxorubicin hydrochloride solution was diluted in phosphate pH 7.4, acetate 5.5 and water at certain concentrations and calibration curves were prepared according to the highest absorbance value of doxorubicin hydrochloride solution at 480 nm. For the maximum absorbance at 480 nanometers, 5 different calibration

curves were prepared. These are the phosphate 7.4 and acetate 5.5 buffer solutions used to calculate release and loading profiles in the range of 1-10 ppm and the calibration with water to calculate loading between 10-400 ppm. 1 ppm solution as an example. The 1000 ppm stock solution was first diluted 100 times and the diluted solution was once again diluted 10 times to obtain 1 ppm. Calibration curve were obtained using the maximum absorbance values of doxorubicin at 480 nm using doxorubicin samples at 1, 2, 3, 4, 5, 6, 7, 8, 9, and 10 ppm concentration. Calibration curve using doxorubicin samples at 10, 20, 40, 60, 80, 100, 150, 200, and 400 ppm concentrations was also obtained in the same way.

As a drug loading procedure, 10 mg of the particles was added into 2 mL 1000 ppm doxorubicin hydrochloride solution. The prepared suspension was first stirred in a sonicator for 30 minutes and then stirred in the dark and inert atmosphere for 24 hours. The suspension was then separated by centrifugation at 6000 rpm for 10 minutes.

The experiments were then continued with drug release. Drug-loaded nanoparticles were taken into 1 mL acetate or phosphate buffer solutions. They were mixed at 150 rpm in a 37 °C incubator to simulate body temperature. 300 µL of the suspension was sampled at 30 minutes 1, 2, 3, 4, 5, 6 and 24 hours, divided into three and the absorbance of each 100 µL sample was measured after addition of 300 µL of fresh buffer solution onto it. The average of the three measurements taken was averaged based on the maximum absorbance values at 480 nm. The release processes were carried out over total moles. Since the number of moles loaded was known from the previous process, the total moles were calculated at each step. Firstly, the absorbance values obtained were substituted into the relevant calibration curves and the concentration was calculated as a result of the release.

2.2.4 Cell Culture

The colorectal cancer cell line HCT-116 was purchased from ATCC (American Type Culture Collection). HCT-116 cells were cultured in RPMI (Roswell Park Memorial Institute Medium, Biological Industries) medium. L-glutamine (2 mmol/L), 1% pen/strep solution and 10% FBS (fetal bovine serum) were added to the RPMI medium. For subculturing, the old medium was first removed, then the cells were washed with 1X PBS (phosphate buffered salt) and incubated with 0.25% Trypsin-EDTA at 37°C until the cells are detached from the growth surface (5-10 minutes). A complete medium with three times the amount of trypsin was used for trypsin inhibition. Cells were centrifuged at 2000 x g for 2 minutes and the supernatant was removed and the cells were suspended with appropriate amount of fresh medium and transferred to new growth flasks or plates. According to ATCC guidelines, HCT116 cell line was grown in a humidified and sterile environment at 37°C with 5% CO_2. The cell lines are regularly tested for mycoplasma contamination by PCR and Plasmocin (Invivogen, USA) is added to the media to prevent mycoplasma contamination.

2.2.5 MTT Analysis

The change in growth and viability of cells after treatment with nanoparticles was determined using MTT [3-(4,5-Dimethylthiazol-2-yl)-2,5-Diphenyltetrazolium bromide]. For the assay, cells were seeded in 96-well plates with 10,000 cells per well as recommended by the MTT protocol. One day after seeding the cells, nanoparticles were prepared by serial dilution method from 100 µg/mL to 12.5 µg/mL concentration of loaded doxorubicin and treated for 24 hours. Free doxorubicin of the same concentration was used as a control. At the end of the treatment period, the media were replaced with fresh media containing MTT and incubated for 4 hours. At the end of the incubation period, 1% SDS - 0.01 M HCl solution was added to each well to dissolve the formazan crystals formed. The plates

were incubated for 16 h and the absorbance at 570 nm wavelength was measured with a spectrophotometer (Multiskan GO; Thermo Fisher Scientific, USA). For the statistical analysis, the absorbance of wells containing only medium and MTT (blank) was subtracted from all other data and the resulting data were normalized to the absorbance of untreated cells and presented as growth rate (%).

2.3 Instrumentation

2.3.1 X-Ray Diffraction

The crystal structures of metal ion-doped and undoped borate compounds were monitored by powder X-ray diffraction measurement. The powder X-ray pattern of each crystal structure of each compound is like a fingerprint of the crystal structure of the compound. The powder X-ray information is recorded in libraries and listed on JCPDS (Joint Committee of Powder Diffraction System) cards. The homogeneous distribution of the doped metal ions in the host matrix will affect the luminescence measurements. When the homogeneously distributed metal ions do not cause phase contamination of the crystal structure or the formation of new compounds, peaks should appear in the same places as the peaks in the powder X-ray pattern of the undoped host borate compound. Only when this is achieved will the synthesis step be considered completed. X-ray diffraction patterns were measured on a Rigaku Miniflex X-Ray Diffractometer. Cu Kα(30 kV, 15mA, λ = 1.54Å) was used as the x-ray source. Panalytical, Empyrean X-Ray Diffractometer was used as another device. Cu Kα (45 kV, 40mA, λ= 1.54Å) was used as an X-ray source. For measurements taken between 5° and 90°, the goniometer was set to rotate 2° per minute.

2.3.2 Fourier Transform Infrared Spectroscopy

Infrared spectroscopy was used to determine the vibrational modes. The measurements were performed using a Nicolet iS50 FTIR Spectrometer with an Attenuated total reflection cap and pellet and the measurements were studied at wavenumber in the range of 540-4000 cm^{-1}.

2.3.3 Photoluminescence

A photoluminescence spectrometer was used to determine the optical properties. The measurements were carried out with Varian Cary Eclipse Fluorescence Spectrometer and Edinburgh Instruments FS5, excitation spectra were based on maximum emission and emission spectra were based on maximum excitation.

2.3.4 Quantum Yield Measurements

Quantum yield measurements were performed for further optical characterization. Measurements were performed with an integrating sphere on an Edinburgh Instruments FS5 device at 0.5 nm/s.

2.3.5 Decay Curve Measurements

Decay curve measurements were taken to calculate the optical extinction. In the handmade device, a 365 nm pulsed laser was used as a source. A photomultiplier tube (Oriel 70-680) was used as a detector. Measurements were taken after the nanoparticles were pelletized.

2.3.6 Scanning Electron Microscopy and Energy Dispersive X-Ray

To examine the morphological properties of the nanoparticles, measurements were taken at METU Central Laboratory in QUANTA 400F Field Emission SEM device. For the determination of the elements on the surface of the obtained nanoparticles, JXA- 8230 electron probe microanalysis device was used in METU Central Laboratory.

2.3.7 Dynamic Light Scattering and Zeta Potential Measurements

The size distribution of the obtained nanoparticles was obtained by dynamic light scattering spectrophotometry. Zetasizer Nano ZS device was used for dynamic light scattering analysis. Zeta potential measurements were also performed on the same device and the phase plot and frequency values given by the device were followed to obtain accurate measurements.

2.3.8 Ultraviolet-Visible Spectroscopy

UV-VIS spectrometer was used to monitor drug loading and release profiles. The experiments performed using Agilent Synergy H1 Hybrid Multi-Mode Reader, measurements were taken using 96 well plates.

2.3.9 Thermal Gravimetric Analysis

Thermal Gravimetric Analyses Measurements were taken up to 800 °C by increasing the temperature by 10 °C per minute in STA 449 F1 Jupiter device.

CHAPTER 3

RESULTS AND DISCUSSION

3.1 X-Ray Diffraction Patterns

The crystal structures of metal ion-doped and undoped triborate and borate compounds were monitored by powder X-ray diffraction measurement. The powder X-ray pattern of each crystal structure of each compound is like a fingerprint of the crystal structure of the compound. The powder X-ray information is recorded in libraries and listed on JCPDS (Joint Committee of Powder Diffraction System) cards. The syntheses of interest were compared with the JCPDS cards and the crystal structure analyses were matched with the compatible cards.

3.1.1 X-Ray Diffraction Patterns of $Gd_{0.95}Ce_{0.025}Tb_{0.025}B_3O_6$ with Different Chelating Agents and Surfactant

Firstly, the synthesis was carried out with different chelating agents or surfactant to see the effect of the chelating agent on the crystal structure.

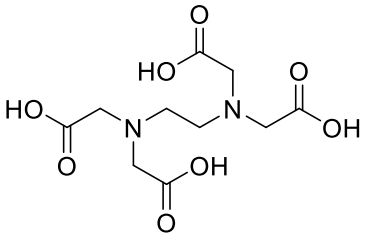

Figure 11: Chemical structure of EDTA

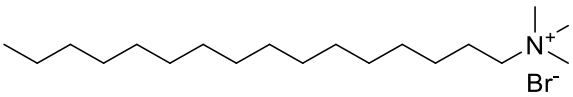

Figure 12: Chemical structure of CTAB

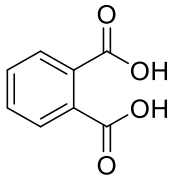

Figure 13: Chemical structure of phthalic acid

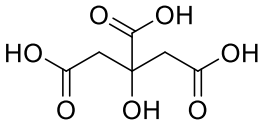

Figure 14: Chemical structure of citric acid

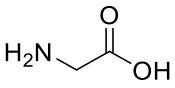

Figure 15: Chemical structure of glycine

The chemical structure of the chelating agents and surfactant is given in **Figure 11, 12, 13, 14 and 15**. Chelating agents and surfactant have an impact on the crystal structure, morphology and luminescence properties of the product. There are certain limitations in borate synthesis according to previous studies regarding the hydrolysis of boric acid and thermodynamic limitations with borate formations. Studies showed that boric acid hydrolysis and polyborate formation is as follows (Sasidharanpillai et al., 2019).

$$B(OH)_3 + OH^- \leftrightarrow [B(OH)_4]^-$$

$$2B(OH)_3 + OH^- \leftrightarrow [B_2(OH)_7]^-$$

$$3B(OH)_3 + OH^- \leftrightarrow [B_3O_3(OH)_4]^- + 3H_2O$$

$$4B(OH)_3 + 2OH^- \leftrightarrow [B_4O_5(OH)_4]^- + 5H_2O$$

$$5B(OH)_3 + OH^- \leftrightarrow [B_5O_6(OH)_4]^- + 6H_2O$$

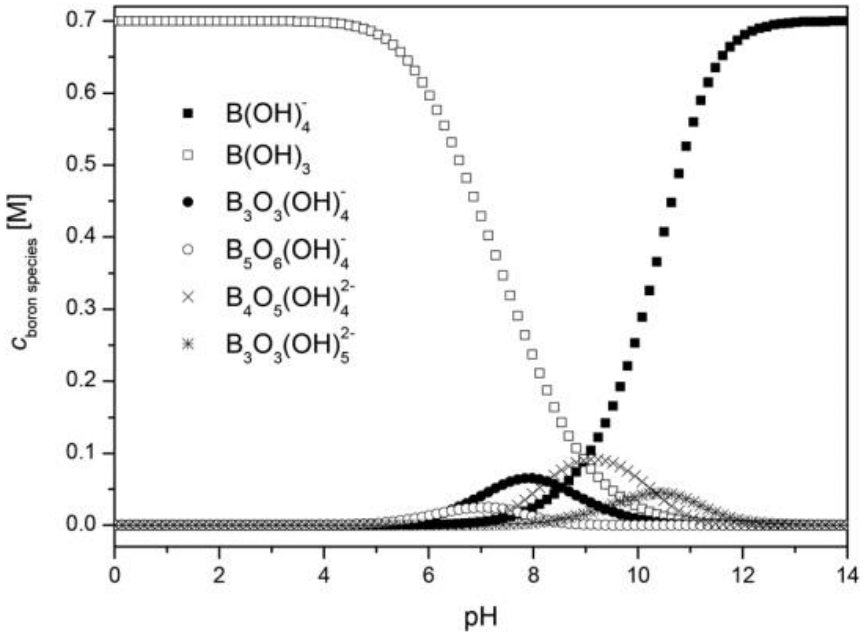

Figure 16: Polyborate formation depending on pH and concentration

It has been stated that the formation of polyborate by boric acid depends on pH. While the formation of the borate structure is required at pH 8, it was suggested that the triborate structure can be found stably at pH 6 and that these formations depend on the concentration of boric acid and can be seen in **Figure 16** (Schott et al., 2014).

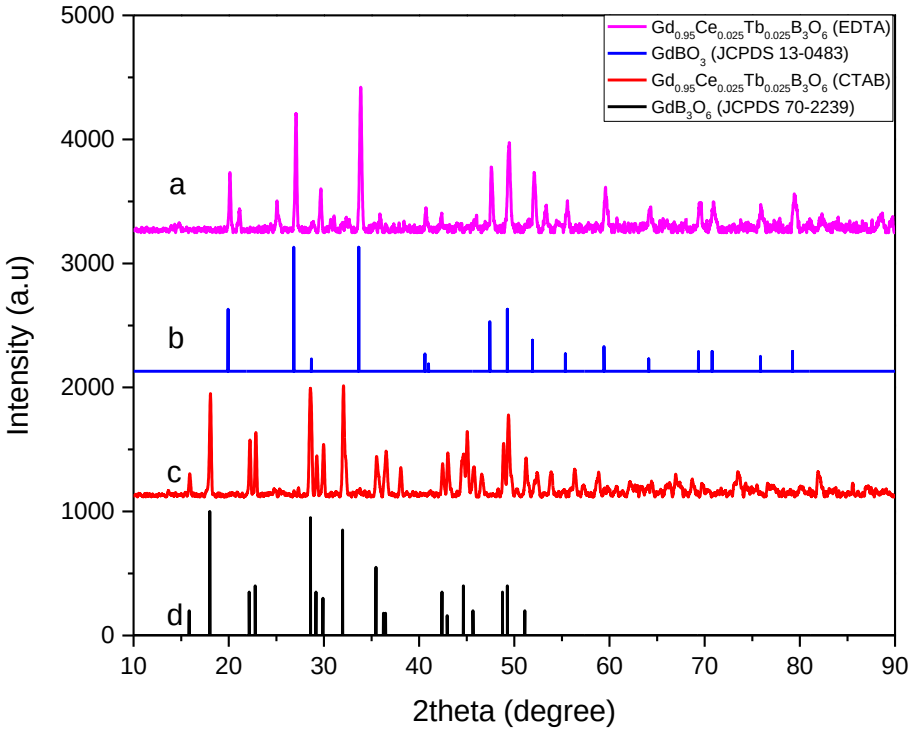

Figure 17: X-Ray diffraction patterns of Ce^{3+}/Tb^{3+} doped GdB_3O_6 with a) EDTA b) JCPDS-130483 and c) CTAB d) JCPDS 70-2239

X-Ray diffraction analysis was performed to analyze the crystal structure of Ce^{3+}/Tb^{3+} doped CTAB and EDTA synthesized GdB_3O_6 nanoparticles that can be seen in **Figure 17**. The recorded diffraction peaks of Ce^{3+}/Tb^{3+} doped GdB_3O_6 with synthesized CTAB, nanoparticles are in an agreement with JCPDS card number 70-2239. Ce^{3+} ion, Tb^{3+} ion, and Gd^{3+} ion radius are 102 pm, 92.3 pm, and 93.8 pm in 6 coordinate respectively. As the synthesis of GdB_3O_6 was processed by decreasing the amount of Gd^{3+} ions. Thanks to lanthanide contraction, ions that doped to the structure can substitude in crystal structure with Gd^{3+} ions. In the experiments with CTAB, the pH was measured at around 6 and CTAB is cationic surfactant to increase number of ions in solution. As a result, it is thought that boric acid hydrolysis is important concerning pH in the triborate structure obtained in sol-gel media. In light of these, it appears that the GdB_3O_6 particle was successfully synthesized with CTAB in single phase without formation of other borate compounds. However, the

formation of the orthoborate, $GdBO_3$, structure could not be explained by pH or thermal character in experiments with EDTA. No related study was found in the literature.

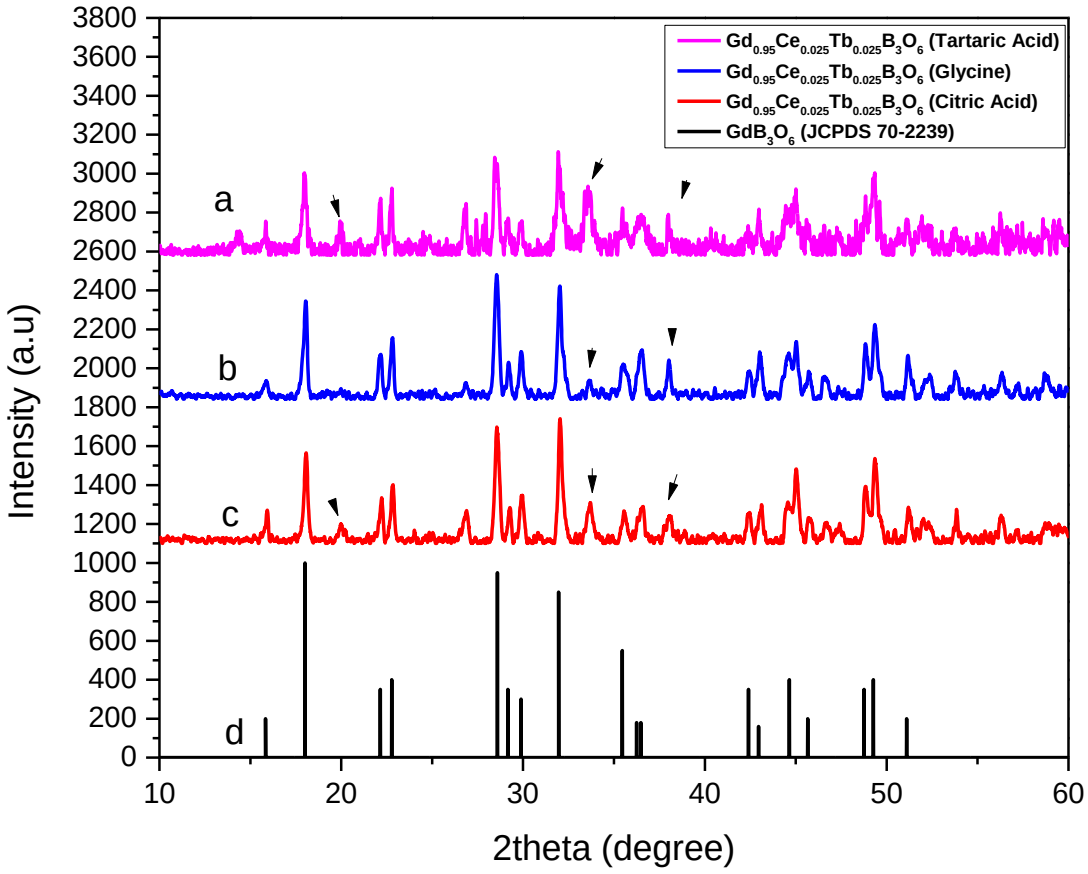

Figure 18: X-Ray diffraction patterns of GdB_3O_6 with a) Tartaric Acid, b) Glycine, c) Citric Acid chelation and d) JCPDS 70-2239

The GdB_3O_6 structure obtained with tartaric acid, glycine and citric acid and matched with the corresponding card number is shown in **Figure 18**. It is seen that the experiments performed are compatible with the relevant JCPDS card, but the diffractions marked in the figure are compatible with $GdBO_3$, combination of both phases. The presence of borate phases in the structure is thought to be the result of diffusion in a high-temperature environment and multiple phase formations are

unavoidable. Moreover, when the intensity values and full width at half maximum values of crystal structures with different chelating agents and surfactant were compared, the highest intensity values and lowest full width at half maximum values were obtained with CTAB. This can be concluded as the highest crystalline and single phase product was acquired with CTAB.

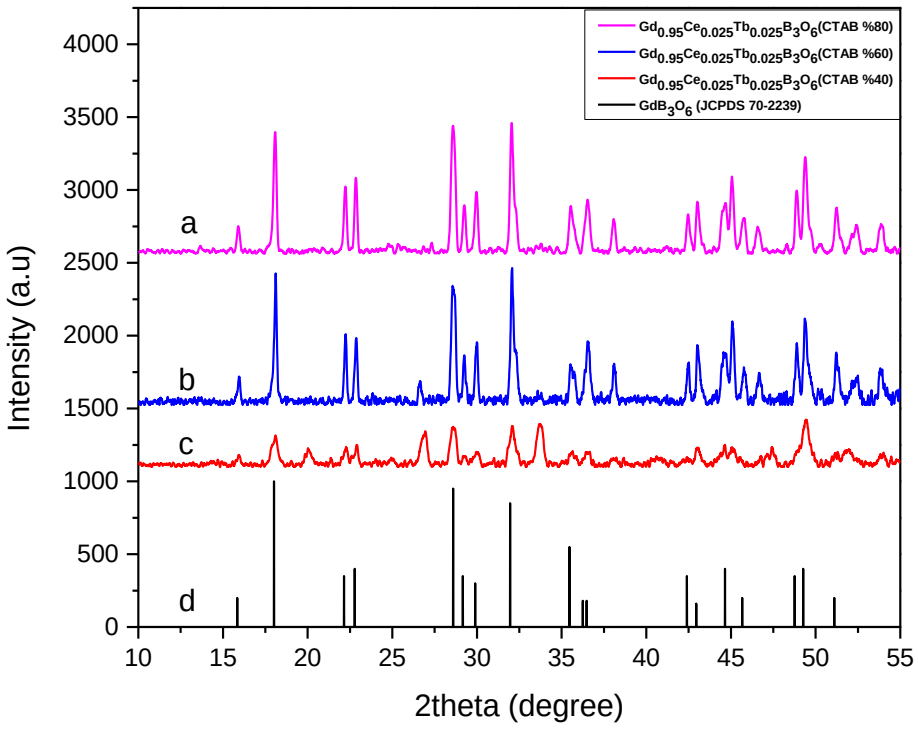

Figure 19: X-Ray Diffraction patterns of Ce^{3+}/Tb^{3+} doped GdB_3O_6 with different CTAB amount a) %80, b) %60 c) %40 and d) JCPDS 70-2239

X-ray diffraction patterns for Ce^{3+}/Tb^{3+} doped GdB_3O_6 structure with different ratios of CTAB are given in **Figure 19**. XRD result shows that 40% mol ratio added CTAB has the lowest in crystallinity. This can be seen in XRD peaks. They are lower in intensity and the full-width half maximum is higher. This concluded as lower in crystallinity. As the mol ratio increases crystallinity increases with the increasing mol ratio. The highest crystallinity is observed at the 80% mol ratio added CTAB.

3.1.2 X-Ray Diffraction Patterns of $Gd_xEu_yB_3O_6$

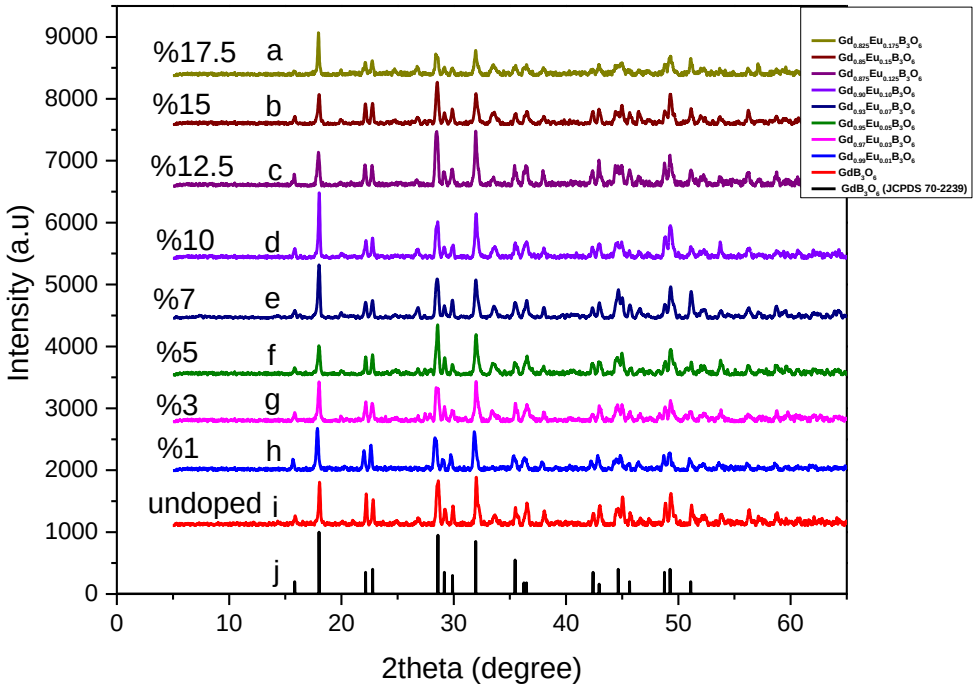

Figure 20: X-Ray diffraction pattern of Eu^{3+} doped GdB_3O_6 structure a) $Gd_{0.825}Eu_{0.175}B_3O_6$, b) $Gd_{0.85}Eu_{0.15}B_3O_6$, c) $Gd_{0.875}Eu_{0.125}B_3O_6$, d) $Gd_{0.90}Eu_{0.10}B_3O_6$, e) $Gd_{0.93}Eu_{0.07}B_3O_6$, f) $Gd_{0.95}Eu_{0.05}B_3O_6$, g) $Gd_{0.97}Eu_{0.03}B_3O_6$, h) $Gd_{0.99}Eu_{0.01}B_3O_6$, i) GdB_3O_6 and j) JCPDS 70-2239

X-Ray diffraction analysis was performed to analyze the crystal structure of Eu^{3+} doped GdB_3O_6 nanoparticles synthesized with CTAB to see whether Europium doping was affecting the structure. Europium values doped up to 17.5% mole ratio are shown in **Figure 20**. Europium-doped GdB_3O_6 nanoparticles were compared with the JCPDS 70-2239 card and found to be compatible. It was determined that gadolinium triborate has a monoclinic crystal system and a C2/c space group. Lattice parameters a=9.83 Å b= 8.15 Å c=6.31 Å and α=90° β=126.83° and γ=90°. In X-Ray analysis, the 2ϑ position varies slightly with size, but it is difficult to distinguish difference since ion sizes are very close to each other due to the lanthanide contraction: The Gd^{3+} radius is 93.8 pm and the Eu^{3+} radius is 94.7 pm in 6

coordinatiton. So that, they can replace each other in the structure. When the intensities of the miller indices are compared between the GdB_3O_6 and EuB_3O_6, it is seen that the structure is more compatible with the GdB_3O_6.

3.1.3 X-Ray Diffraction Patterns of $Gd_xEu_yBO_3$

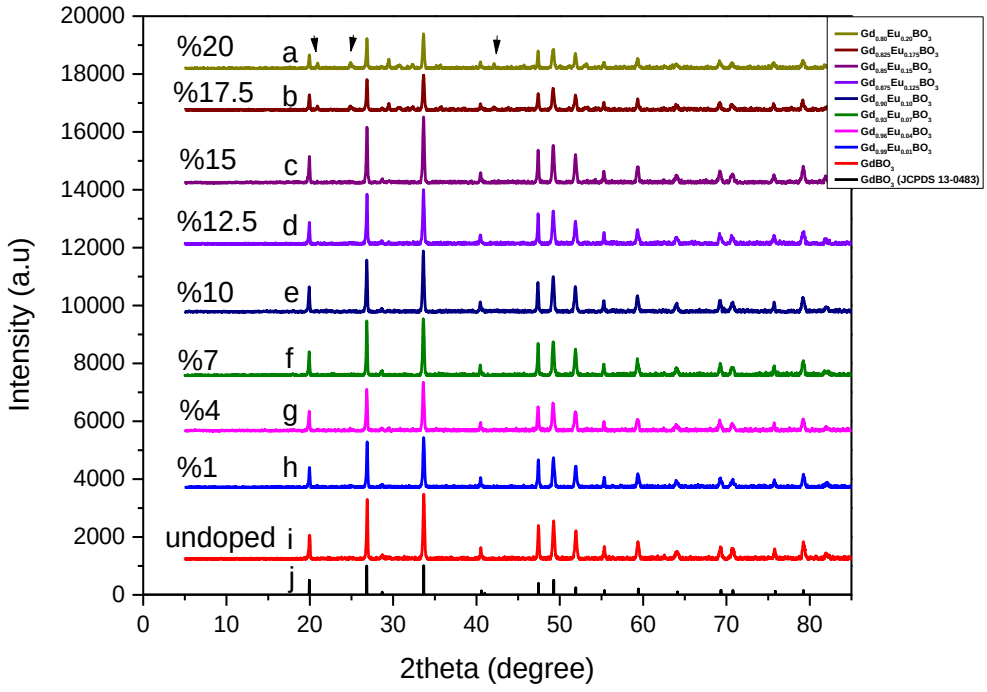

Figure 21: X-Ray diffraction patterns of Eu^{3+} doped $GdBO_3$ structure a) $Gd_{0.80}Eu_{0.20}BO_3$, b) $Gd_{0.825}Eu_{0.175}BO_3$, c) $Gd_{0.85}Eu_{0.15}BO_3$, d) $Gd_{0.875}Eu_{0.125}BO_3$, e) $Gd_{0.90}Eu_{0.10}BO_3$, f) $Gd_{0.93}Eu_{0.07}BO_3$, g) $Gd_{0.96}Eu_{0.04}BO_3$, h) $Gd_{0.99}Eu_{0.01}BO_3$, i) $GdBO_3$ and j) JCPDS 13-0483

X-Ray diffraction analysis was performed to analyze the crystal structure of Eu^{3+} doped $GdBO_3$ nanoparticles synthesized with CTAB. It investigated whether Europium doping affects the structure. Eu^{3+} doped up to 20% are shown in **Figure 21**. Eu^{3+} doped $GdBO_3$ nanoparticles were compared with the JCPDS 13-0483 card and found to be compatible. It was determined that $GdBO_3$ has a hexagonal crystal system and a $P6_3/mmc$ space group. Lattice parameters a=b=3.829 Å and c=8.89 Å

and $\alpha=\beta=90°$ $\gamma=120°$. As a result of the analysis, $EuBO_3$ phases with lattice parameters a=b=3.845 Å and c=8.94 Å and $\alpha=\beta=90°$ $\gamma=120°$ with hexagonal crystal system were found the increase of Europium doping in the borate structure and the phases are marked in **Figure 21**. The space group of the $EuBO_3$ is unspecified in the related JCPDS card number. It is interpreted that the increase in the amount of Europium changes the crystal structure. Schott et al. studied $EuBO_3$ complexes in aqueous solutions and observed the formation of borates in aqueous solutions with Europium. The appearance of the Europium phase at increasing concentrations can be explained in this way (Schott et al., 2014). In addition, under high temperature, excess Eu^{3+} ion forms complexes with borate, which explains the emergence of these phases.

3.1.4 X-Ray Diffraction Patterns of Hydroxyapatite and Hydroxyapatite Coating

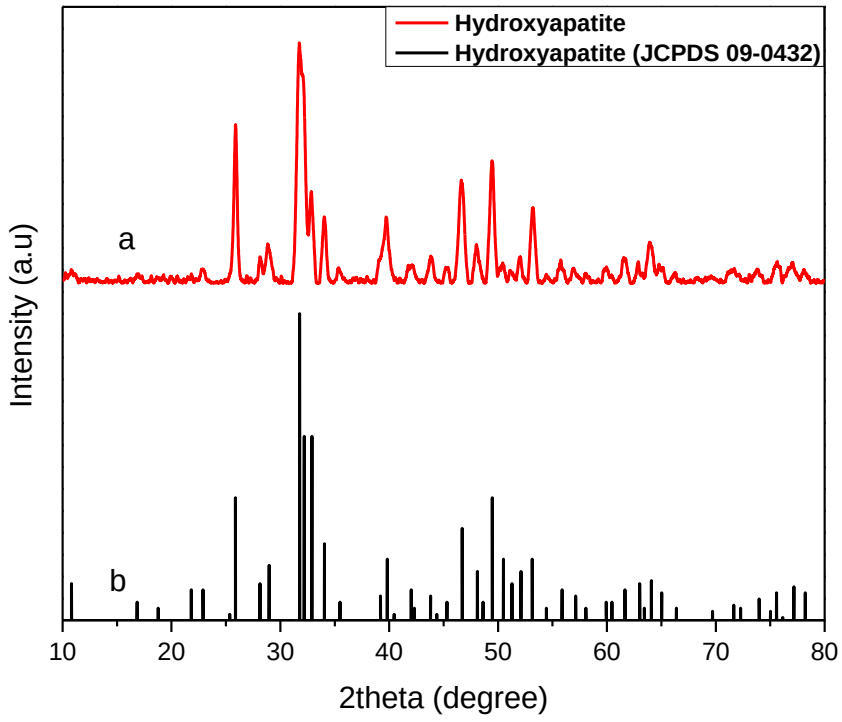

Figure 22: X-Ray diffraction pattern of a) hydroxyapatite and b) JCPDS 09-0432

Before coating the hydroxyapatite, the hydroxyapatite itself was synthesized by the wet precipitation method. For crystal structure analysis, the hydroxyapatite was matched to the JCPDS 09-0432 card and found to be compatible in **Figure 22**. This indicates that hydroxyapatite was successfully synthesized. The obtained hydroxyapatite has a hexagonal crystal structure and a $P6_3/m$ space group. Lattice parameters a=b= 9.55 Å and c=6.92 Å and $\alpha=\beta= 90°$ $\gamma= 120°$.

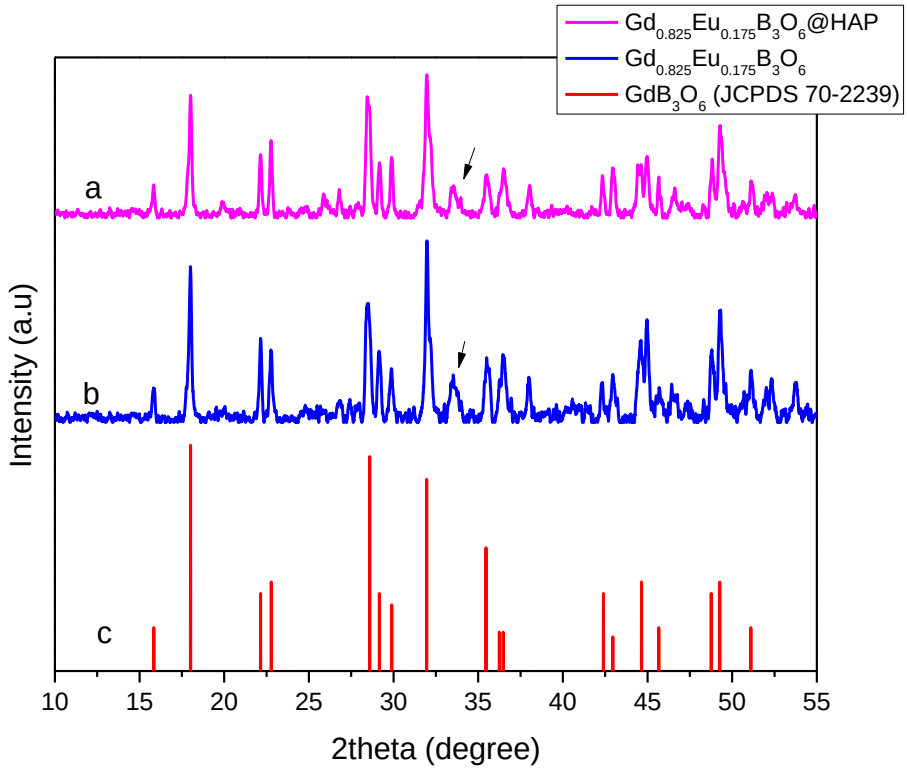

Figure 23: X-Ray diffraction patterns a) $Gd_{0.825}Eu_{0.175}B_3O_6$@HAP, b) $Gd_{0.825}Eu_{0.175}B_3O_6$ and c) JCPDS 70-2239

X-Ray diffraction analysis was performed after hydroxyapatite coating and it was determined that most of the diffraction peaks came from GdB_3O_6 particles. The generated diffraction pattern was compared with the GdB_3O_6 JCPDS card in **Figure 23**. In X-Ray diffraction, the detector detects the x-ray from the planes. Since Gadolinium is a heavier element than calcium and GdB_3O_6 has a higher crystallinity when compare with hydroxyapatite, most of the diffractions are thought to come from the core which is $Gd_{0.825}Eu_{0.175}B_3O_6$. Marked diffraction is found that the peak belongs to the $GdBO_3$ structure.

3.2 Optical Measurements

Photoluminescence emission and excitation spectra were performed to investigate the optical properties. First, the optical properties of the Ce^{3+}/Tb^{3+} doped GdB_3O_6

structure were investigated to see the effect of the chelating agent or surfactant on photoluminescence. Then the amount of CTAB was studied. The optical properties of Eu^{3+} doped GdB_3O_6 and $GdBO_3$ compounds were then investigated for the red light, and quantum yield and decay lifetime measurements were also completed.

3.2.1 Photoluminescence Measurements of $Gd_{0.95}Ce_{0.025}Tb_{0.025}B_3O_6$ with different chelating agents and surfactant

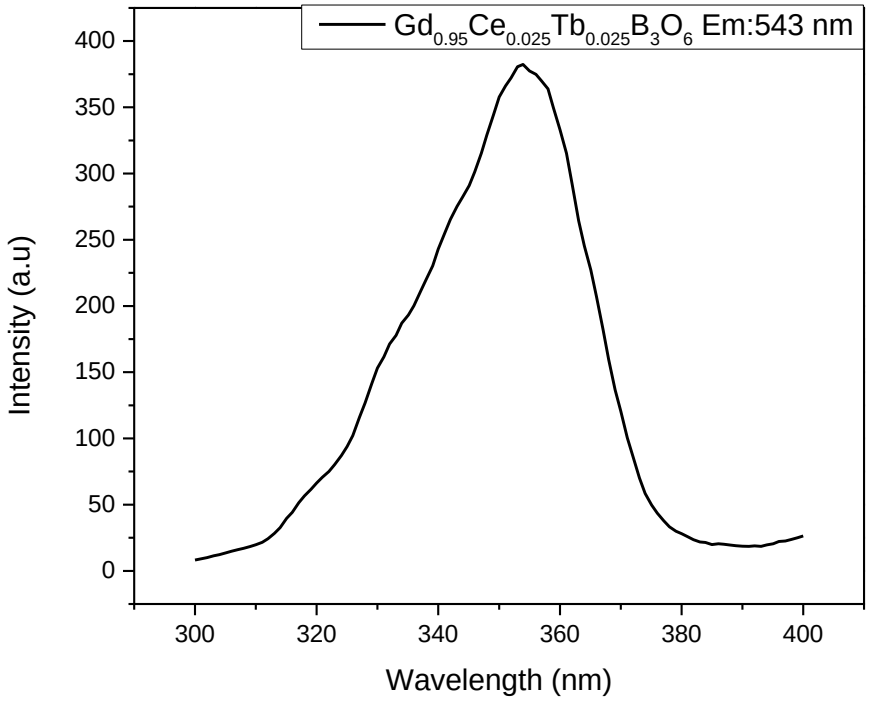

Figure 24: Excitation spectrum of Ce^{3+}/Tb^{3+} doped GdB_3O_6 structure

In order to obtain the maximum emission, the excitation spectrum of the Ce^{3+}/Tb^{3+} doped GdB_3O_6 particle was measured and the maximum excitation was determined as 353 nm and represented in **Figure 24**.

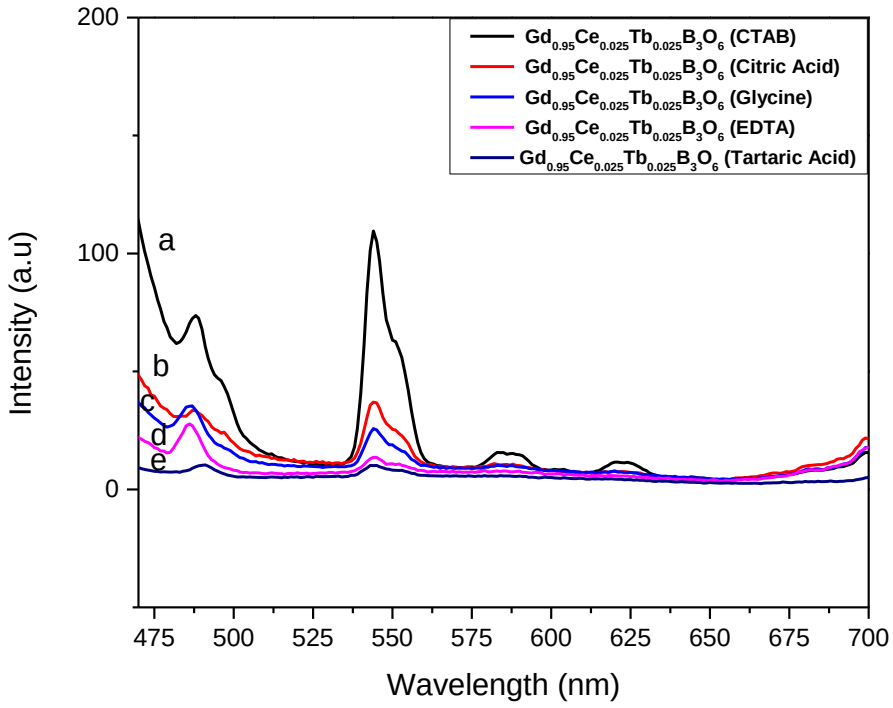

Figure 25: Photoluminescence spectrum of Ce^{3+}/Tb^{3+} doped GdB_3O_6 structure with the different chelating agents and surfactant a) CTAB, b) Citric Acid, c) Glycine, d) EDTA, e) Tartaric Acid

The emission graph of Ce^{3+}/Tb^{3+} doped GdB_3O_6 particles synthesized with different chelating agents and surfactant is shown in **Figure 25**. Emissions of Tb^{3+} ion belong to the $^5D_4 \rightarrow {}^7F_6$ transition at 480 nm, $^5D_4 \rightarrow {}^7F_5$ at 543 nm, $^5D_4 \rightarrow {}^7F_5$ at 590 nm, $^5D_4 \rightarrow {}^7F_4$ at 590 nm and $^5D_4 \rightarrow {}^7F_3$ at 620 nm. As mentioned in the introduction, Cui et al. suggested that the highest luminescence intensity is achieved when the doped ion is uniformly distributed in the crystal cell (Seraiche et al., 2020b). In studies with different chelating agents and surfactant, the highest luminescence intensity was obtained with CTAB. The reason for that, CTAB forms micelles in the solution and the CTAB has a long carbon chain in the structure. Therefore, CTAB makes the most uniform distribution that causes the highest luminescence intensity. Another reason is that the highest crystallinity in the structure was obtained with

CTAB since the highest intensity and lowest FWHM in the XRD pattern were acquired by CTAB.

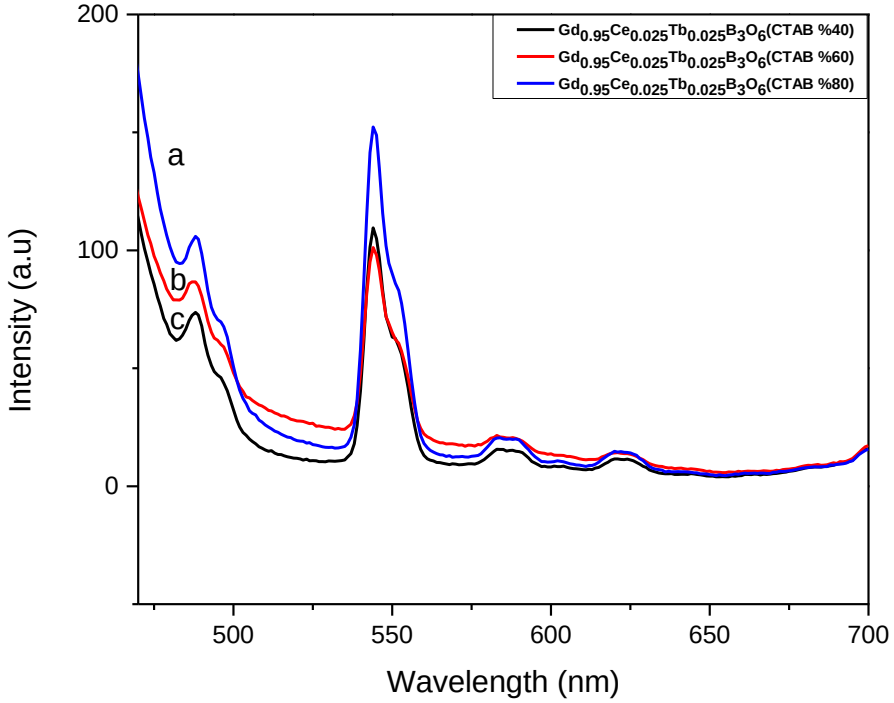

Figure 26: Photoluminescence spectrum of Ce^{3+}/Tb^{3+} doped GdB_3O_6 structure with CTAB amount a) %80, b) %60, c) %40

As seen in **Figure 26**, optical measurements were taken on the amount of CTAB and it was observed that the highest intensity was obtained in the GdB_3O_6 structure synthesized with an 80% mole ratio CTAB. CTAB amount affects the crystal structure of the Ce^{3+}/Tb^{3+} doped GdB_3O_6 structure. Wang et al. studied the effect of surfactants on the photoluminescence properties of ZnO films. They synthesized with the different surfactant, and surfactant ratios and observed that the highest luminescence intensity was obtained with higher crystallinity. Since the crystallinity of particles affects the luminescence intensity, GdB_3O_6 particles crystallinity changes with the CTAB as the crystallinity increases it is observed that luminescence intensity increases (J. Wang et al., 2019).

3.2.2 Photoluminescence Measurements of $Gd_xEu_yB_3O_6$

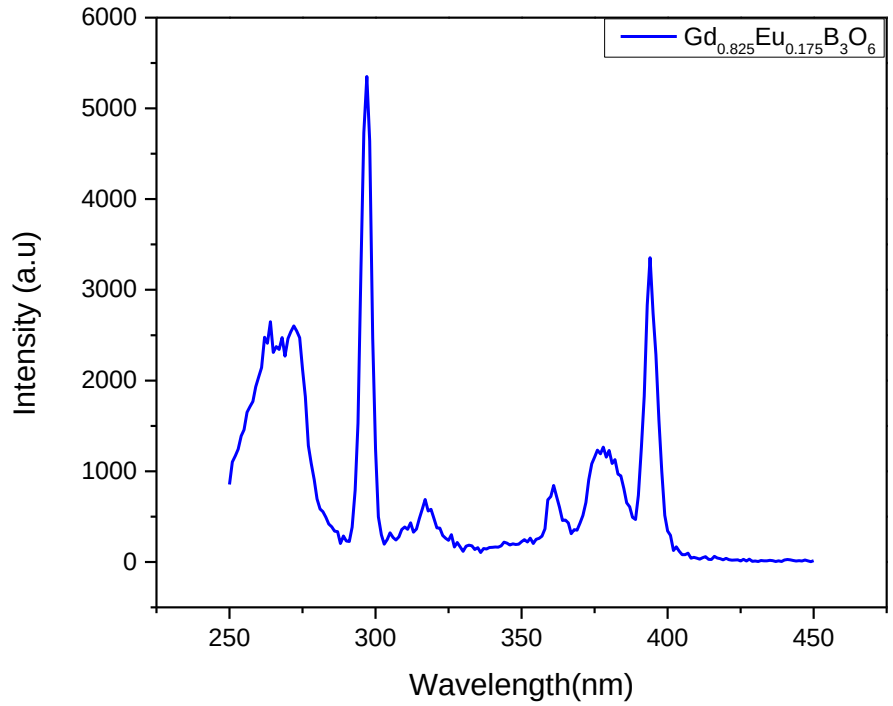

Figure 27: Excitation spectrum of Eu^{3+} doped GdB_3O_6 structure

After obtaining the highest luminescence intensity with CTAB, Eu^{3+} doped GdB_3O_6 particle was synthesized. Meng et al. performed optical studies on Eu^{3+} doped $Gd(BO_2)_3$ compound and found that there is an energy transfer from the Gd host to Eu at 272 nm and the reason for this is the $^8S_{7/2} \rightarrow {}^6I_{7/2}$ transition and examined its optical properties by exciting Eu at 393 nm due to the transition of $^7F_0 \rightarrow {}^5L_6$. In their studies, they observed that Eu^{3+} doping does not cause concentration quenching and intensity increases as the amount of Eu^{3+} increases (Meng et al., 2012). The excitation spectra for Eu^{3+} doped GdB_3O_6 particles were collected with a slit width of 2.5 mm and the highest excitation values were determined in **Figure 27**. Thus, emission spectra were collected with excitation at 272 nm, 296 and 393 nm for transfer.

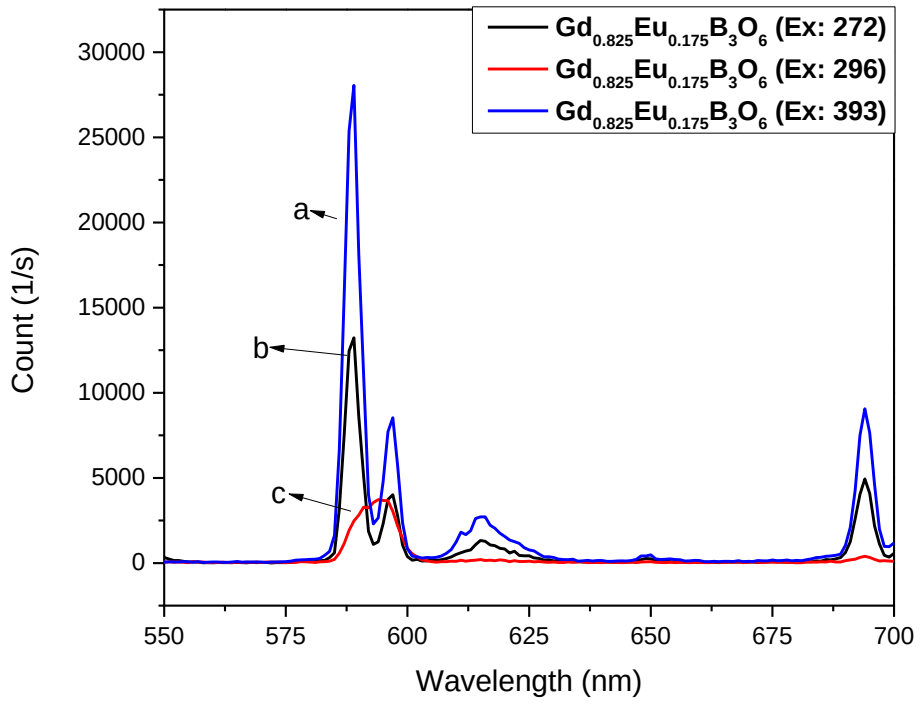

Figure 28: Emission spectrum of Eu^{3+} doped GdB_3O_6 structure a) excitation at 393 nm, b) excitation at 272 nm, c) excitation at 296 nm

The related excitation and related emissions after excitation are shown in **Figure 28**. The emission data collected by excitation at 272, 296 and 393 nm were measured between 550-700 nm at a slit width of 2.5 mm for both excitation and emission. The transition at 585 nm is referred to as the $^5D_0 \rightarrow {}^7F_1$ transition. Emission at 610 nm refers to emission $^5D_0 \rightarrow {}^7F_2$, emission at 650 nm to $^5D_0 \rightarrow {}^7F_3$ and emission at 700 nm to transition $^5D_0 \rightarrow {}^7F_4$. The reason why the emission to $^5D_0 \rightarrow {}^7F_1$ is higher than $^5D_0 \rightarrow {}^7F_2$ is thought to be the magnetic dipole transition of $^5D_0 \rightarrow {}^7F_1$ emission and the electric dipole transition of $^5D_0 \rightarrow {}^7F_2$ emission. (Binnemans, 2015).

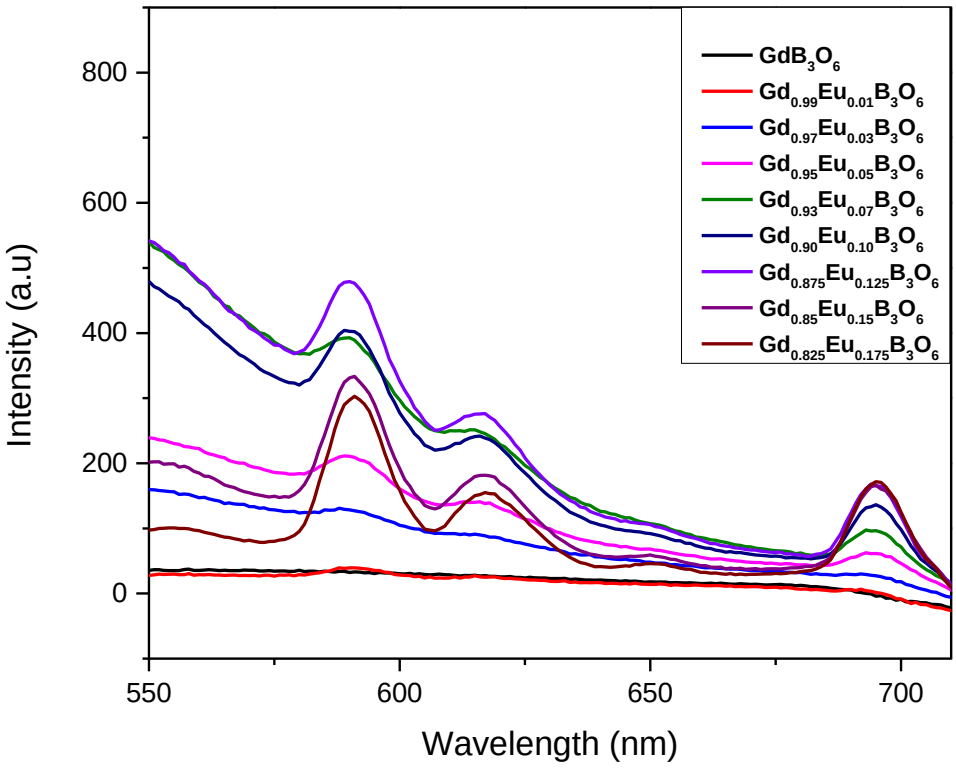

Figure 29: Emission spectrum of Eu^{3+} doped GdB_3O_6 structure with different doping concentration

Emissions for Europium ions doped at different concentrations are represented in **Figure 29**. In line with the literature, concentration quenching was not observed at increasing Europium concentration with the doped Eu^{3+} ion. The reason concentration quenching is not encountered is that this phenomenon is usually seen in energy transfer (Ju et al., 2013). At 394 nm, Europium undergoes a transition of $^7F_0 \rightarrow {}^5L_6$ and increasing Europium concentration increases the intensity.

3.2.3 Photoluminescence Measurements of $Gd_xEu_yBO_3$

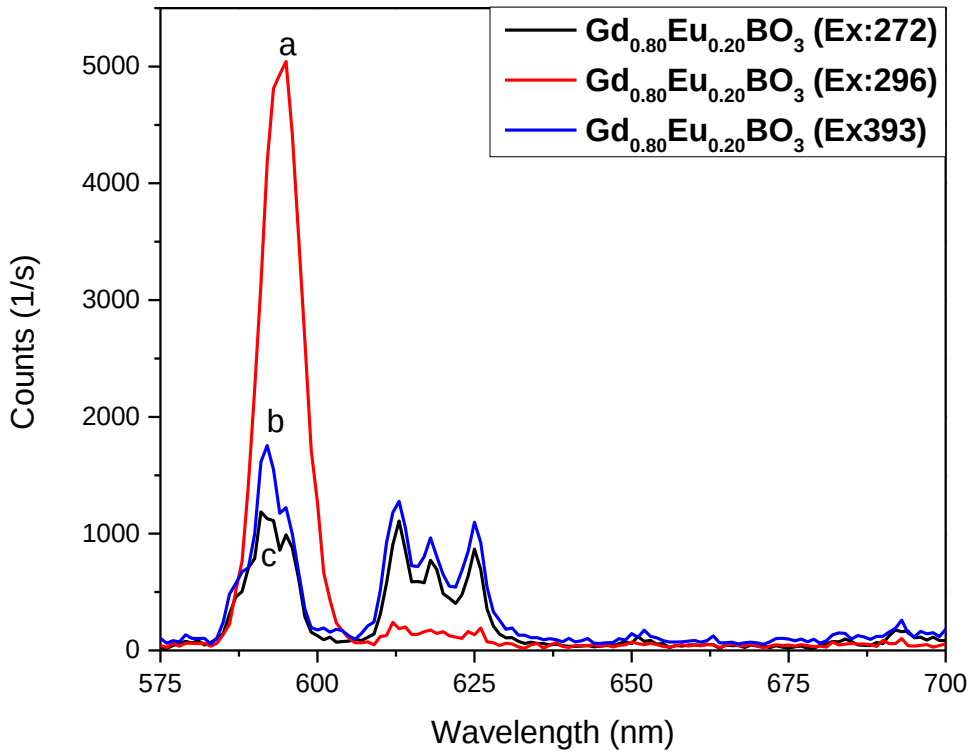

Figure 30: Emission spectrum of Eu^{3+} doped $GdBO_3$ structure a) excitation at 296 nm, b) excitation at 393 nm, c) excitation at 272 nm

The related excitation and related emissions after excitation are shown in **Figure 30**. The emission data collected by excitation at 272, 296 and 393 nm were measured between 550-700 nm at a slit width of 2.5 mm for both excitation and emission. The transition at 585 nm is referred to as the $^5D_0 \rightarrow {}^7F_1$ transition. Emission at 610 nm and 625 nm refers to emission $^5D_0 \rightarrow {}^7F_2$, emission at 650 nm to $^5D_0 \rightarrow {}^7F_3$ and no emission at 700 nm to transition $^5D_0 \rightarrow {}^7F_4$ was observed for the BO_3 structure. $^5D_0 \rightarrow {}^7F_2$ emissions splits into two separate emissions lines due to the fact that the crystal field splitting (Seraiche et al., 2020).

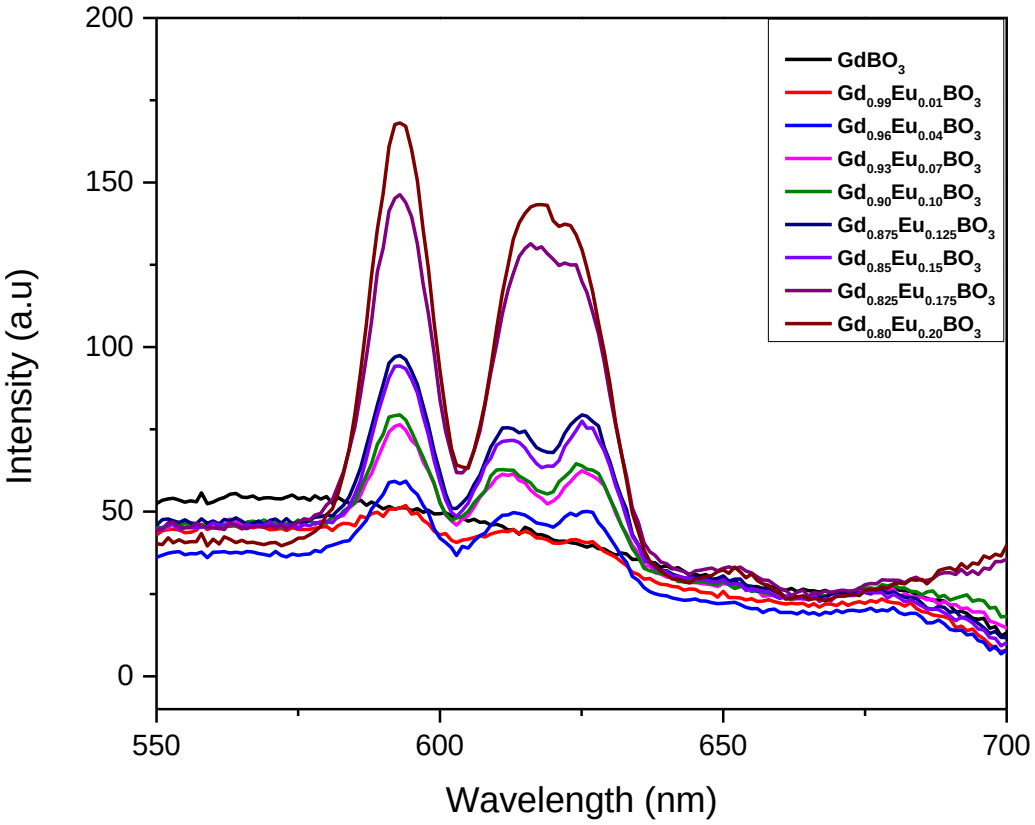

Figure 31: Emission spectrum of Eu^{3+} doped $GdBO_3$ structure with different doping concentrations

Emissions for Europium ions doped at different concentrations are represented in **Figure 31**. In line with the literature, concentration quenching was not observed as in the B_3O_6 structure at increasing europium concentration with the doped Eu^{3+} ion.

3.2.4 Comparsion of $Gd_xEu_yB_3O_6$ and $Gd_xEu_yBO_3$

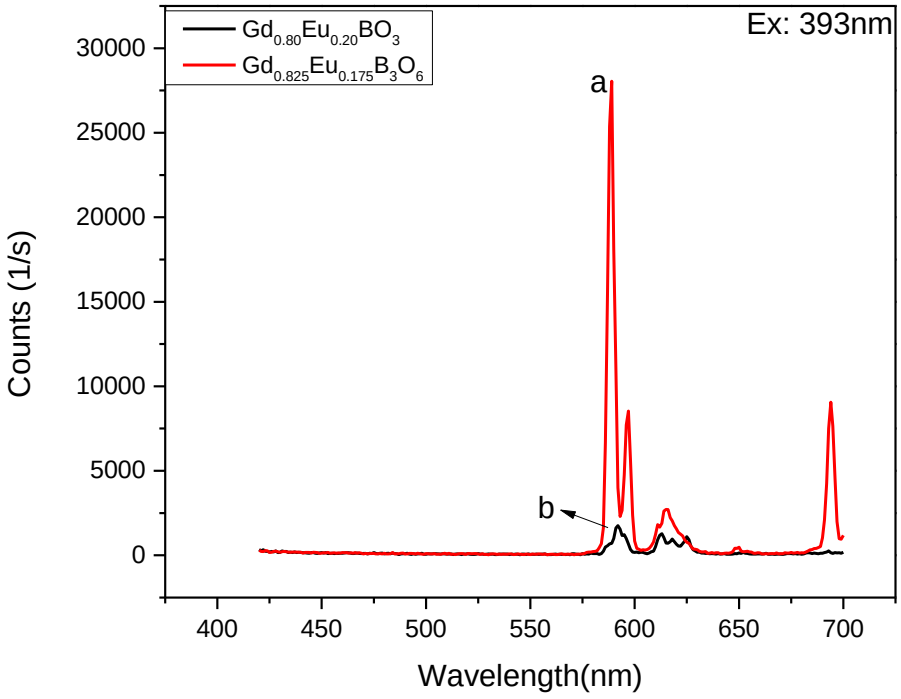

Figure 32: Comparison of a) $Gd_{0.825}Eu_{0.175}B_3O_6$ and b) $Gd_{0.80}Eu_{0.20}BO_3$ structure

In line with the obtained photoluminescence results, $Gd_{0.825}Eu_{0.175}B_3O_6$ and $Gd_{0.80}Eu_{0.20}BO_3$ nanoparticles were compared depending on the intensity in **Figure 32**. As a result of the analysis, the luminescence intensity was found to be higher in the triborate structure than in the borate structure. In addition, the transition at 700 nm could not be observed in the borate structure. In his publication, Rukang worked with isolated BO_3, BO_4 and B_3O_6 groups and examined their transition energies and UV absorption wavelengths. As a result, he proved that UV absorption is dominated by the oxygen in the tetrahedral BO_4 group, while BO_3 groups have absorption edges at lower wavelengths (Li, 1989). According to this information, borates are formed by combinations of tetrahedral BO_4 and trigonal planar BO_3 groups. Since these combinations will be different for borate and triborate structures, since their UV

absorption is different, the triborate particle that can absorb more, can emit more and its intensity is higher.

3.2.5 Photoluminescence Measurements after Hydroxyapatite Coating

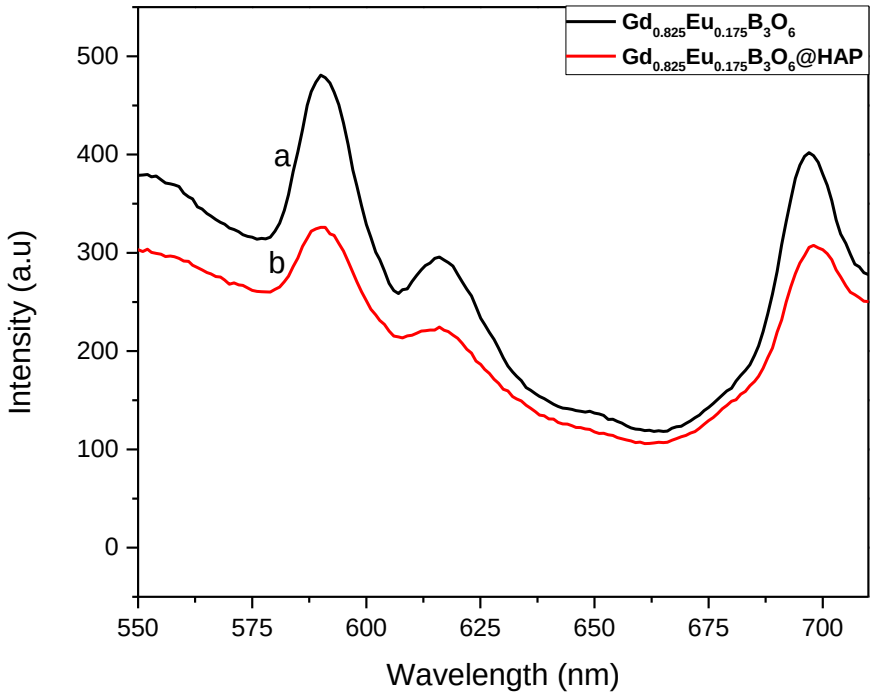

Figure 33: Emission spectrum of Eu^{3+} doped GdB_3O_6 structure a) before and b) after hydroxyapatite coating

The emission graph of the Eu^{3+} doped GdB_3O_6 structure at 394 nm after coating with hydroxyapatite is shown in **Figure 33**. The transition of $^5D_0 \rightarrow {}^7F_1$, $^5D_0 \rightarrow {}^7F_2$ $^5D_0 \rightarrow {}^7F_4$ can be seen in the emission spectrum. Ain et al. conducted powder UV studies of hydroxyapatite and found that hydroxyapatite has an absorbance at 394 nm (Ain et al., 2019). In theory, each material has a refractive index and extinction coefficient. Since the extinction coefficient causes an exponential decrease in the electric field of the incident wave, it is thought that the luminescence intensity decreases as a result

of an extra coating (Mark Fox, 2010). The absorbance of hydroxyapatite at 394 nm also supports this idea.

3.2.6 Quantum Yield Calculations of $Gd_xEu_yB_3O_6$ and $Gd_xEu_yBO_3$

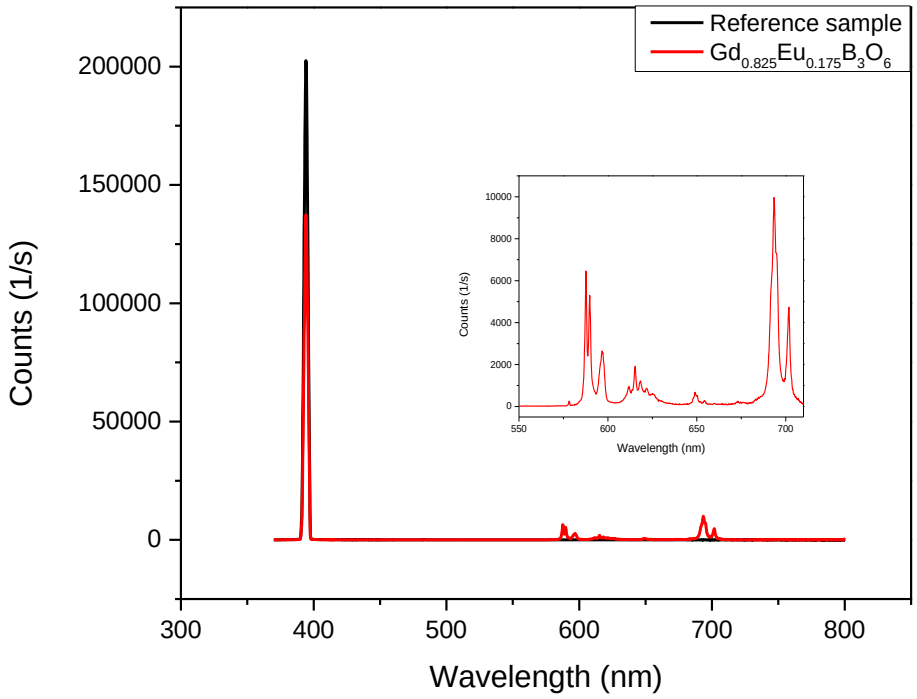

Figure 34: Quantum yield measurement of $Gd_{0.825}Eu_{0.175}B_3O_6$ structure with 394 nm excitation, inset shows the emission between 550-710 nm

For further characterization of the optical properties, the quantum yield calculations were carried out. To calculate the quantum yield of the $Gd_{0.825}Eu_{0.175}B_3O_6$ particle, measurements were first taken on an integrating sphere coated with $BaSO_4$, a material with very high reflection in the device. The particle was then excited at a 394 nm excitation value in the same integrating sphere and the values are shown in **Figure 34**. Ems is the emission area of the particle, Er is the excitation area of the reference and Es is the excitation area of the particle. In theory, the field difference between excitation is considered absorption and the ratio of emission to absorption

gives the quantum yield. For the particle excited at 394 nm, the fields were calculated in the Origin program and the values are as follows.

$$\eta = \frac{E_{ms}}{E_r - E_s}$$

E_r: 708503.5573852

E_s: 478729.664019

E_{ms}: 44347.4839082

As a result of the calculations, the quantum yield for the emission of the particle at 700 nm was calculated as 19.3%.

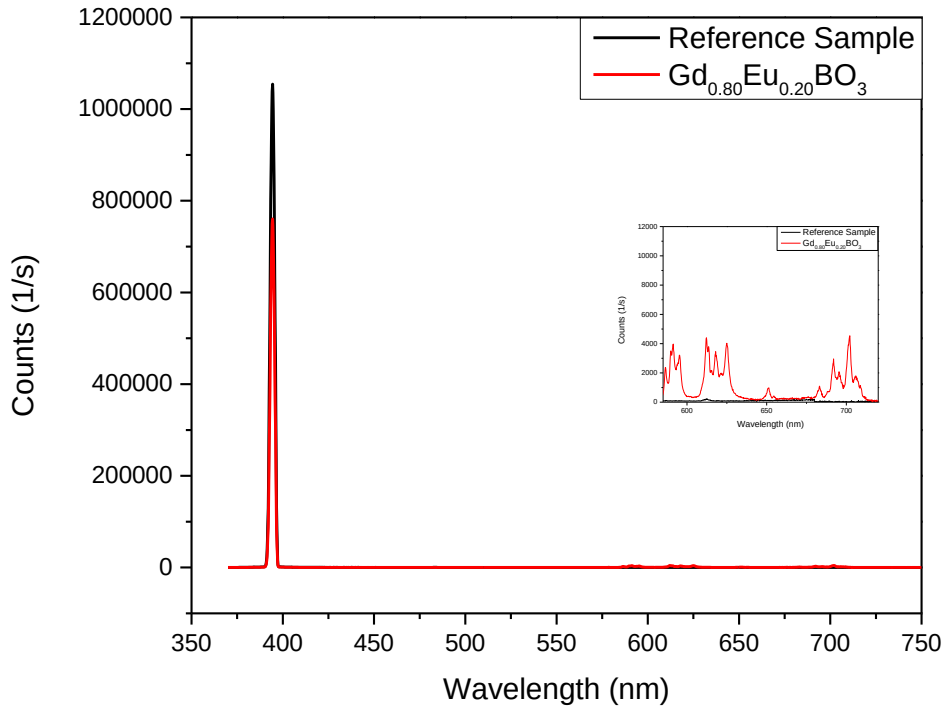

Figure 35: Quantum yield measurement of $Gd_{0.80}Eu_{0.20}BO_3$ structure with 394 nm excitation, inset shows the emission between 550-700 nm

The same experiment has carried out for the $Gd_{0.80}Eu_{0.20}BO_3$ compounds in **Figure 35**.

E_r: 3161058.618669

E_s: 2210076.8672

E_{ms}: 5455.137243

As a result of the calculations, the quantum yield for the emission of the particle at 700 and 585 nm was calculated as 0.57% and %3 respectively.

3.2.7 Decay Lifetime Measurements of $Gd_xEu_yB_3O_6$ and $Gd_xEu_yBO_3$

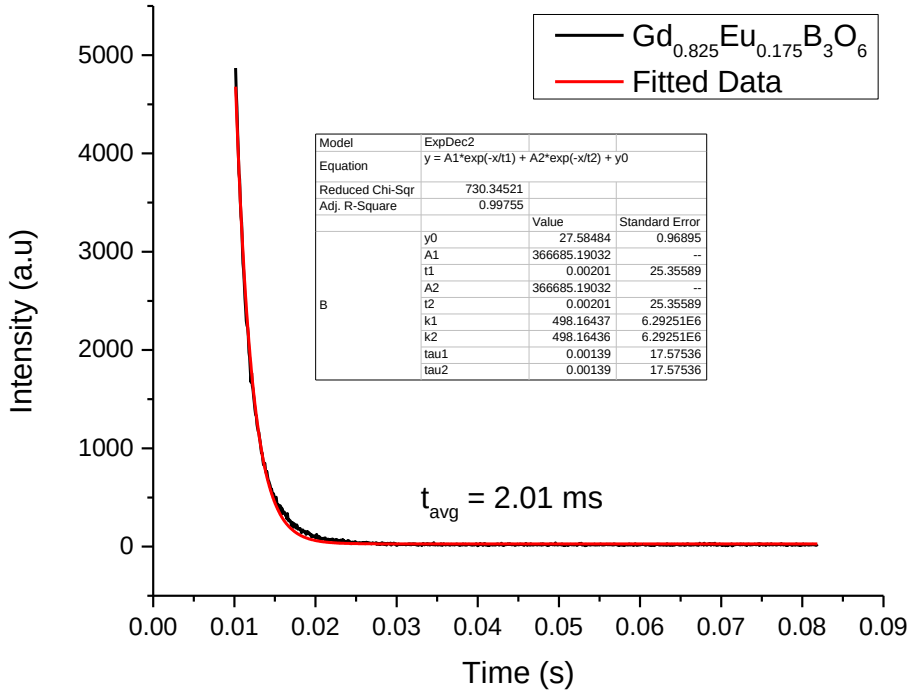

Figure 36: Decay measurement for the Eu^{3+} doped GdB_3O_6 structure

Decay lifetime measurements were performed in Prof. Dr. Enver Bulur's laboratory with a 365 nm pulsed laser excitation source. Since 585 nm has the highest intensity in the experiments with $Gd_{0.825}Eu_{0.175}B_3O_6$, the emission at 585 nm was used and the decay curves obtained were fit as single and double exponential decay functions.

Since the R^2 value of the double exponential decay function is higher than single, double exponential decay function values were used and the time is given as average. The values related to the fit are shown in **Figure 36**. For the $Gd_{0.825}Eu_{0.175}B_3O_6$ particle, the decay time is calculated as 2.01 ms.

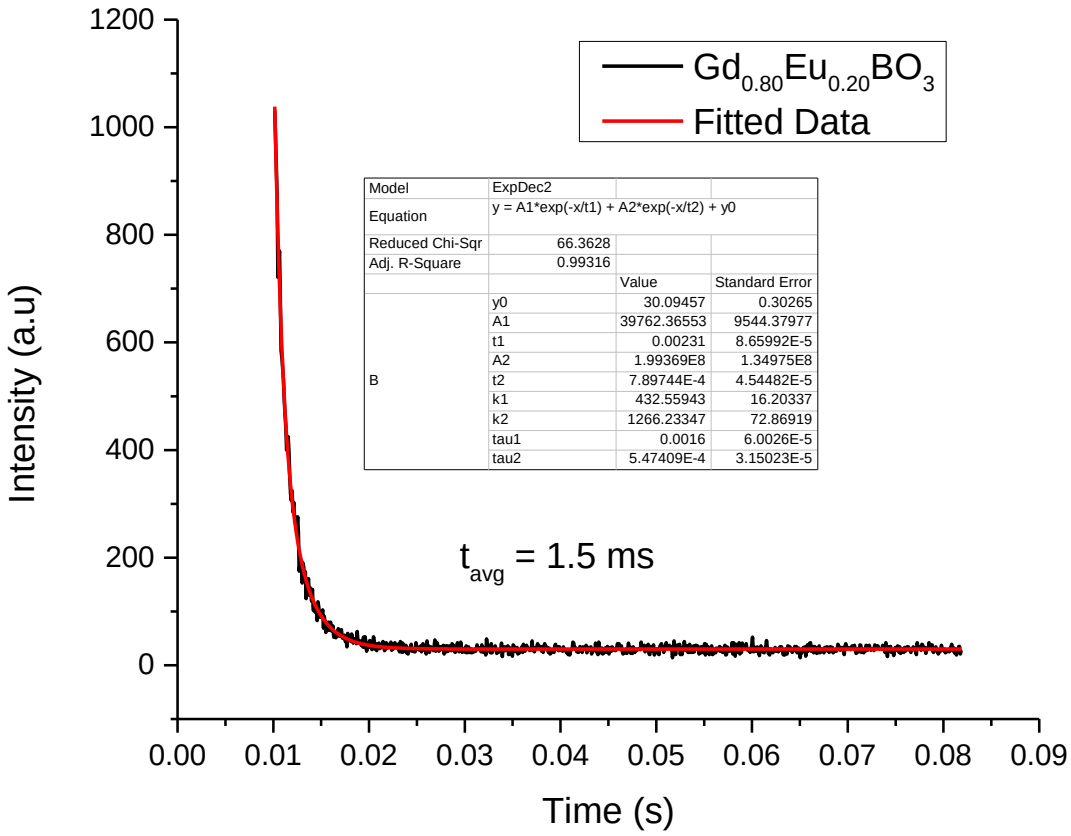

Figure 37: Decay measurement for Eu^{3+} doped $GdBO_3$ structure

The same procedure was completed for the $Gd_{0.80}Eu_{0.20}BO_3$ particle and the decay lifetime was calculated as 1.5 ms which is shown in **Figure 37**. Since the decay lifetime difference between triborate and borate particles is an intensity-dependent measurement, the differences between their durations are thought to be due to intensity differences.

3.3 FT-IR Measurements

3.3.1 FT-IR Measurements of $Gd_{0.95}Ce_{0.025}Tb_{0.025}B_3O_6$ with different chelating agents

Infrared spectroscopy was used to analyze the vibrational modes of the particles and to further characterize their phases. Due to their polymeric behaviour, borates form triangular BO_3 and tetrahedral BO_4 anions in complex combinations. The expected vibrational modes for isolated BO_3 groups with trigonal planar D_{3h} symmetry and BO_4 groups with tetrahedral T_d symmetry are shown in the table below (Weir & Schroeder, 2000).

Table 7: Expected infrared spectroscopy wavenumber for BO_3 and BO_4 groups

	D_{3h} BO_3 group	**T_d BO_4 group**
Symmetrical strech	950 cm^{-1}	1000 cm^{-1}
Out-of-plane bend	750 cm^{-1}	Below 600 cm^{-1}
Antisymmetric strech	1250 cm^{-1}	1000 cm^{-1}
In-plane bend	600 cm^{-1}	600 cm^{-1}

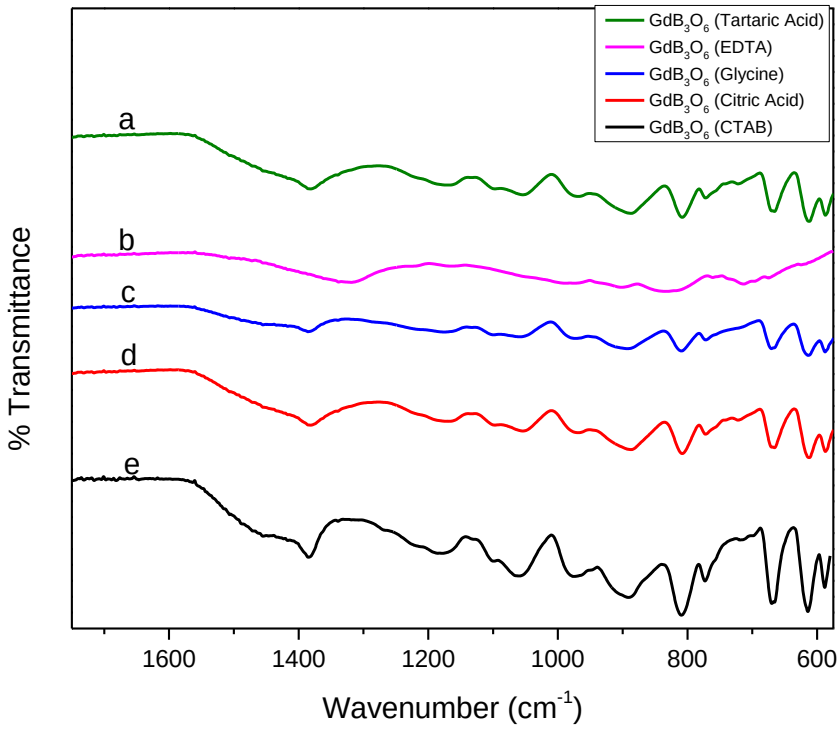

Figure 38: FT-IR spectrum of GdB_3O_6 structure with different chelating agents and surfactant a) Tartaric Acid, b) EDTA, c) Glycine, d) Citric Acid, e) CTAB

In experiments with different chelating agent and surfactant, infrared spectroscopy was used to complete the characterization and to analyze the BO_3 and BO_4 structures in the structure in **Figure 38**. As a result of the analysis, the expected values of BO_3 and BO_4 groups in the structure are given in **Table 7**.

3.3.2 FT-IR Measurements of $Gd_xEu_yB_3O_6$

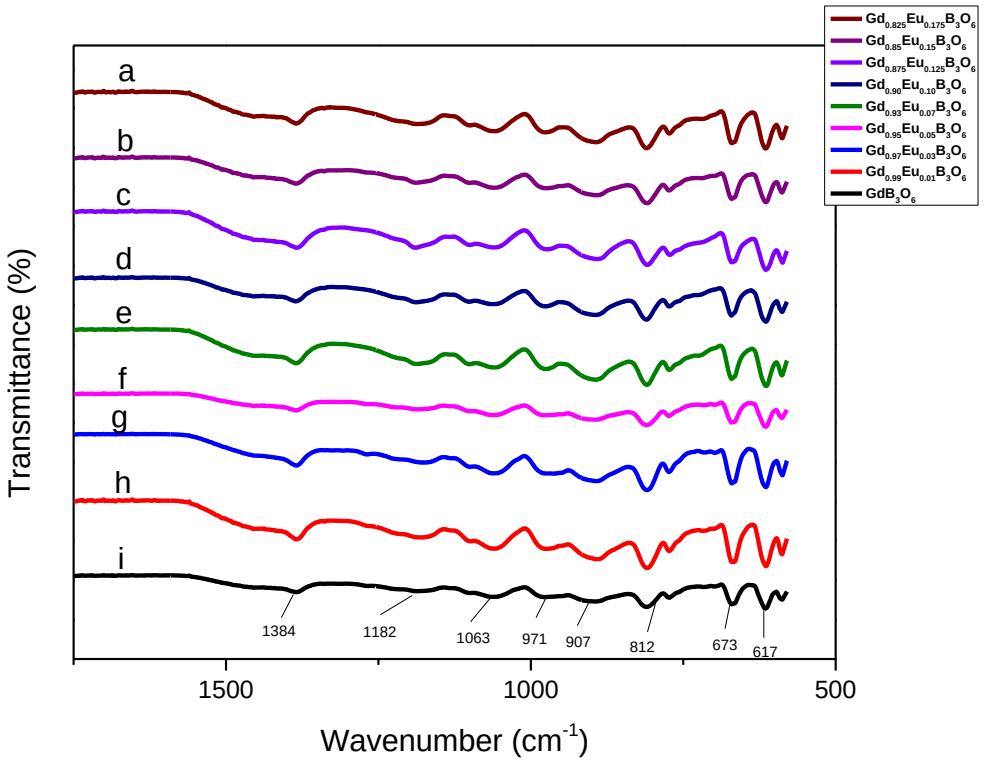

Figure 39: FT-IR spectrum of Eu^{3+} doped GdB_3O_6 structure a) $Gd_{0.825}Eu_{0.175}B_3O_6$, b) $Gd_{0.85}Eu_{0.15}B_3O_6$, c) $Gd_{0.875}Eu_{0.125}B_3O_6$, d) $Gd_{0.90}Eu_{0.10}B_3O_6$, e) $Gd_{0.93}Eu_{0.07}B_3O_6$, f) $Gd_{0.95}Eu_{0.05}B_3O_6$, g) $Gd_{0.97}Eu_{0.03}B_3O_6$, h) $Gd_{0.99}Eu_{0.01}B_3O_6$, i) GdB_3O_6

FT-IR spectroscopy analysis was performed to complete the characterization of the $Gd_{1-x}Eu_xB_3O_6$ particles and to see whether the doped ions form phases in **Figure 39**. First of all, in the studies conducted in the literature, the triborate structure contains trigonal planar BO_3 and tetrahedral BO_4 groups together in the unit cells. It is important to see BO_3 and BO_4 structures in the analysis for the continuation of the characterization. The peaks seen at 1100 and 1500 cm^{-1} are due to the modes of the BO_3 group. Peaks between 800 and 1100 cm^{-1} come from 4-fold boron compounds. The peaks at 812 and 673 cm^{-1} come from tetrahedral and trigonal planar peaks due to bending, respectively (Weir & Schroeder, 2000). For the triborate structure, unlike the $GdBO_3$ structure, no change in phases was observed with doping.

3.3.3 FT-IR Measurements of $Gd_xEu_yBO_3$

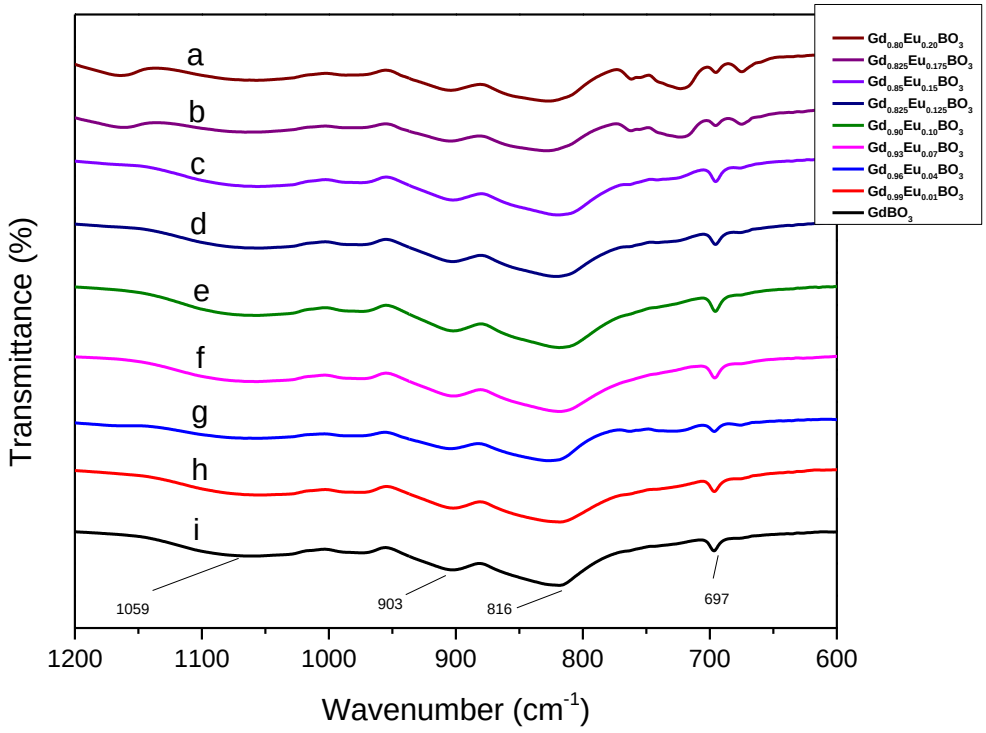

Figure 40: FT-IR spectrum of Eu^{3+} doped $GdBO_3$ structure a) $Gd_{0.80}Eu_{0.20}BO_3$, b) $Gd_{0.825}Eu_{0.175}BO_3$, c) $Gd_{0.85}Eu_{0.15}BO_3$, d) $Gd_{0.875}Eu_{0.125}BO_3$, e) $Gd_{0.90}Eu_{0.10}BO_3$, f) $Gd_{0.93}Eu_{0.07}BO_3$, g) $Gd_{0.96}Eu_{0.04}BO_3$, h) $Gd_{0.99}Eu_{0.01}BO_3$, i) $GdBO_3$

FT-IR spectroscopy analysis was performed to complete the characterization of the $Gd_{1-x}Eu_xBO_3$ particles and to see whether the doped ions form phases in **Figure 40**. First of all, rare earth orthoborates can exist in three isostructural forms. La-Nd orthoborates are defined as aragonite type, Sm-Yb orthoborates as vaterite type and Lu borates as calcite type borates. While aragonite and calcite-type borates contain isolated BO_3 groups in their structures, vaterite-type borates contain BO_3 and BO_4 structures together. The reason for this is actually due to the presence of the $B_3O_9^{9-}$ ring in the vaterite type. As a result of the analysis, the peaks at the range 500 - 1250 cm^{-1} belong to vaterite-type borate. In the peaks starting with 17.5% mole ratio Europium doped borate structure, the peaks appearing between 1250 and 1500 cm^{-1}

are associated with the formation of the Europium phase with the formation of phases in XRD results. These results indicate the formation of calcite-type Europium borates in the structure (Seraiche et al., 2020).

3.3.4 FT-IR Measurements of Hydroxyapatite and Hydroxyapatite Coating

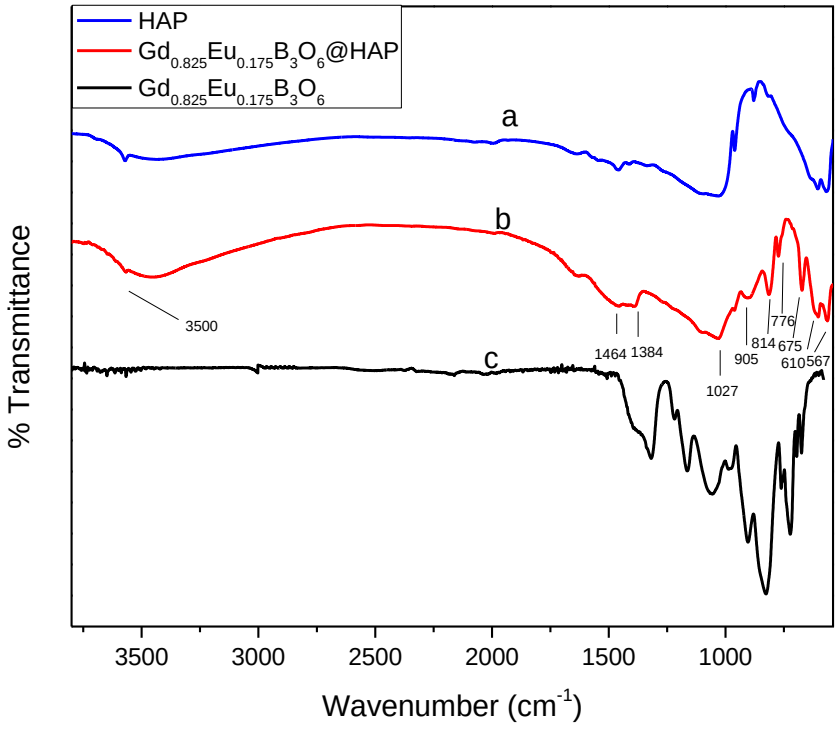

Figure 41: FT-IR spectrum of a) hydroxyapatite, b) after hydroxyapatite coating c) $Gd_{0.825}Eu_{175}B_3O_6$

Infrared analyses of $Gd_{0.825}Eu_{175}B_3O_6$, hydroxyapatite and hydroxyapatite-coated $Gd_{0.825}Eu_{175}B_3O_6$ structure are given in **Figure 41**. The peaks of the coated triborate structure are also marked in the figure. According to the analysis and literature review, 567 and 610 cm^{-1} peaks are due to the P-O bending mode. 675 and 812 cm^{-1} come from the trigonal BO_3 and tetrahedral BO_4 bending features, respectively, 1364 and 1464 cm^{-1} indicate BO_3 stretching, 3500 cm^{-1} indicates O-H stretching,

while the peak at 1027 cm^{-1} belongs to the vibrational mode of the P-O group. As a result of the analysis, contrary to X-Ray analysis, vibrational patterns of the core and coating were obtained in hydroxyapatite coating. Another important point is that the O-H stretching mode is seen to distinguish hydroxyapatite from calcium phosphate. This proves the presence of hydroxyl groups in the structure. As a result, the hydroxyapatite coating was successful according to the infrared results.

3.3.5 FT-IR Measurements after PEGylation

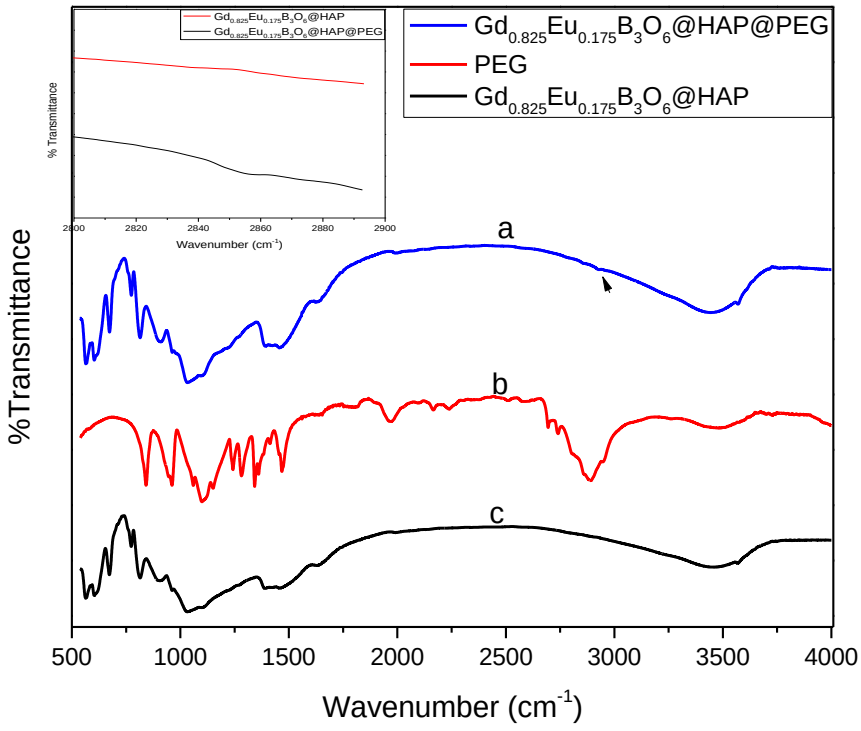

Figure 42: FT-IR spectrum of a) $Gd_{0.825}Eu_{0.175}B_3O_6$@HAP@PEG, b) PEG, c) $Gd_{0.825}Eu_{0.175}B_3O_6$@HAP, inset represents the range between 2800 cm^{-1} and 2900 cm^{-1} of a and c

The infrared data of hydroxyapatite-coated triborate particles after PEGylation are given in **Figure 42**. The GdB_3O_6 particles coated in **Figure 42** were analyzed and only a different peak at 2850 cm^{-1} was determined in the analysis after PEGylation

was completed. The peak at 2850 cm^{-1} belongs to PEG 10000 as can be understood from the figure and it is thought that the PEGylation is complete.

3.4 Dynamic Light Scattering Measurements

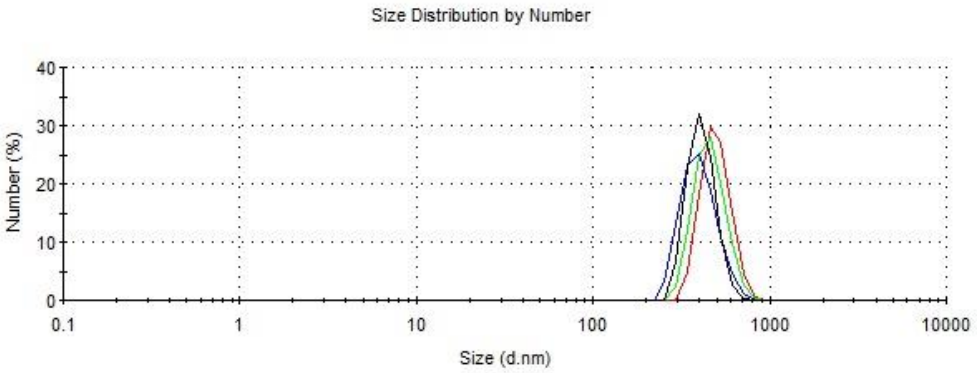

Figure 43: Dynamic Light Scattering of GdB_3O_6 structure with CTAB

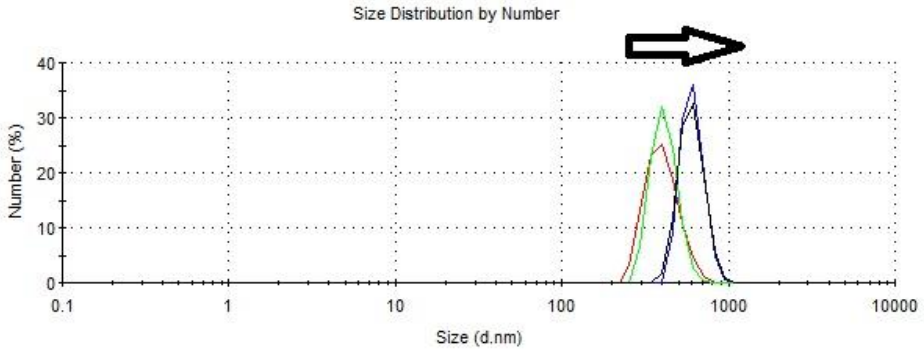

Figure 44: Dynamic Light Scattering after hydroxyapatite coating

DLS results of GdB_3O_6 structures synthesized with CTAB and hydroxyapatite-coated are given in **Figures 43** and **Figure 44**. As a result of the analysis, the size distribution by the number value of the GdB_3O_6 structure synthesized with CTAB was found to be 458.65 nm on average, while it was found to be 616.85 nm in the results considering that the size distribution would increase after coating. In line with these results, as expected, an increase in particle size was observed and the coating is considered to be successful.

3.5 Scanning Electron Microscopy and Energy Dispersive X-Ray Analysis

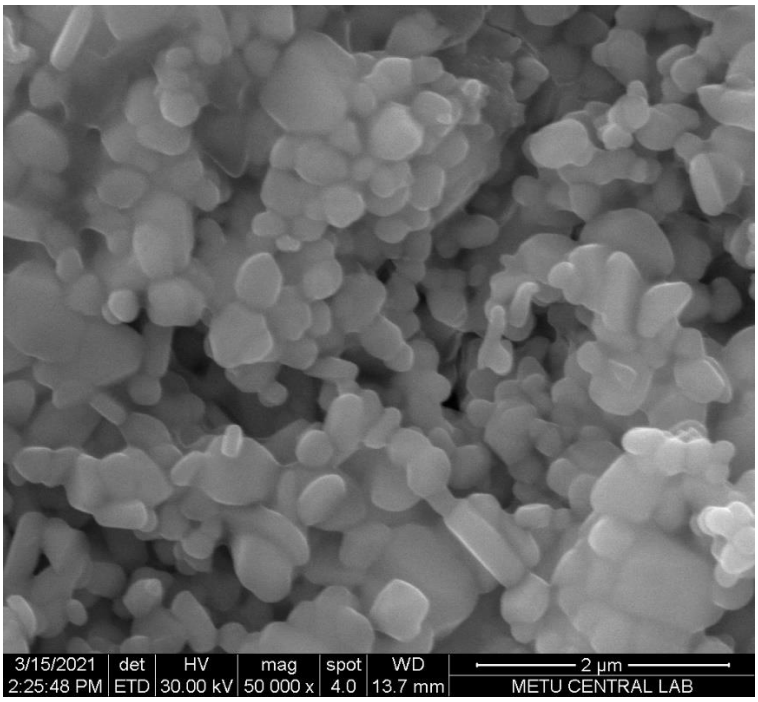

Figure 45: SEM images of GdB_3O_6 structure before hydroxyapatite coating

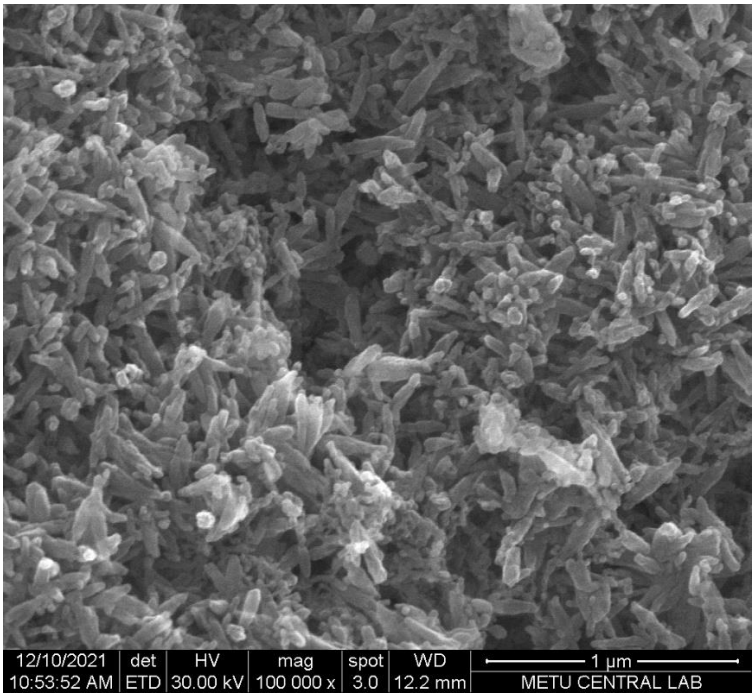

Figure 46: SEM images of GdB_3O_6 structure after hydroxyapatite coating

SEM images of GdB_3O_6 structures synthesized with CTAB and hydroxyapatite-coated are given in **Figures 45** and **Figure 46**. SEM images were taken to examine their morphological properties. **Figure 45** shows the spherical structure is observed. In **Figure 46**, in the images obtained after coating, the particles become more prismatic. The change in the morphology also shows that hydroxyapatite coating was successfully achieved. After hydroxyapatite coating, agglomeration of the particles was decreased concerning CTAB synthesized particles when compared to **Figure 45** and **Figure 46**.

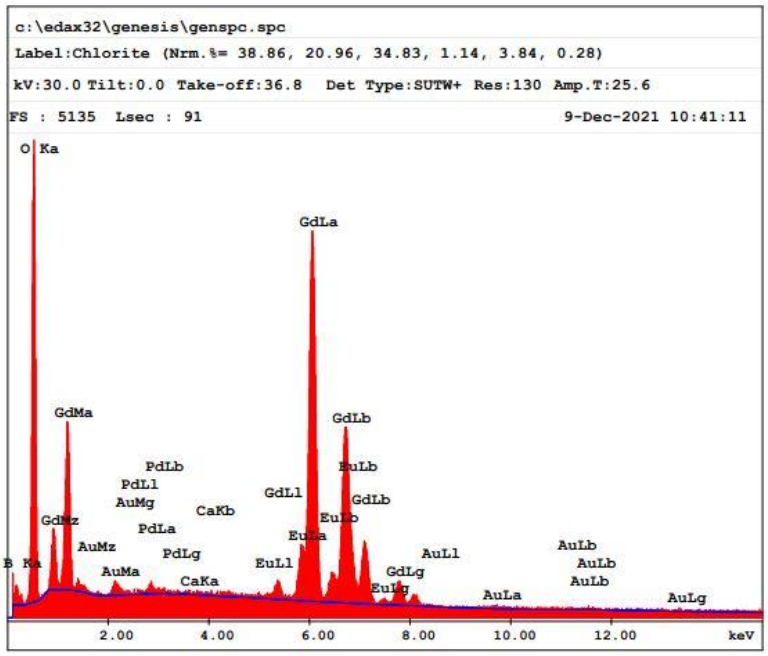

EDAX ZAF Quantification (Standardless)
Element Normalized
SEC Table : Default

Element	Wt %	At %	K-Ratio	Z	A	F
B K	30.05	58.39	0.0919	1.0512	0.2909	1.0001
O K	27.31	35.86	0.0704	1.1099	0.2322	1.0000
PdL	0.51	0.10	0.0036	0.8764	0.8081	1.0076
CaK	0.03	0.02	0.0003	1.0583	0.7894	1.0219
EuL	5.23	0.72	0.0490	0.8469	1.1061	1.0003
GdL	36.23	4.84	0.3334	0.8308	1.1072	1.0004
AuL	0.63	0.07	0.0049	0.7905	0.9997	1.0000
Total	100.00	100.00				

Figure 47: EDX analysis before hydroxyapatite coating

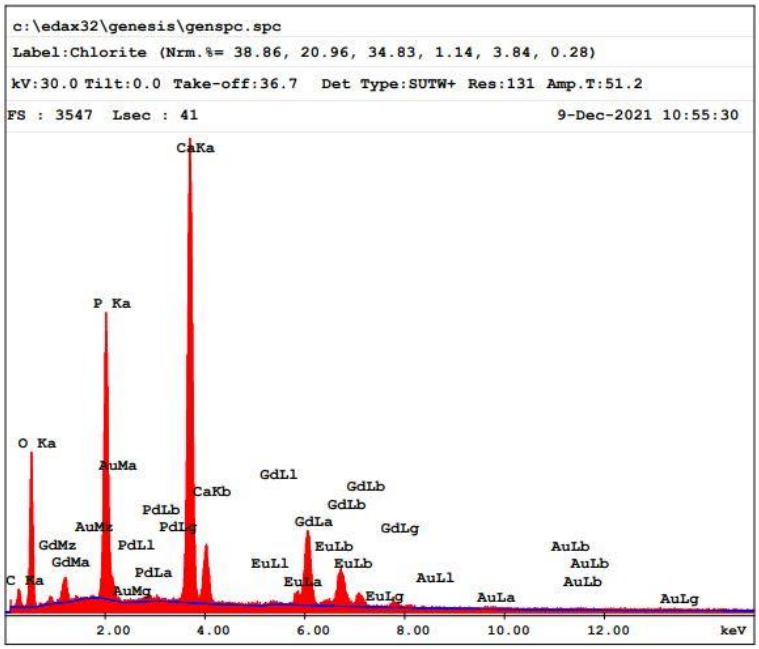

EDAX ZAF Quantification (Standardless)
Element Normalized
SEC Table : Default

Element	Wt %	At %	K-Ratio	Z	A	F
C K	9.58	19.98	0.0192	1.0782	0.1856	1.0005
O K	32.77	51.27	0.0500	1.0629	0.1435	1.0001
P K	14.75	11.92	0.0730	0.9920	0.4965	1.0058
PdL	0.62	0.15	0.0045	0.8355	0.8499	1.0214
CaK	21.43	13.38	0.1779	1.0070	0.8171	1.0091
EuL	2.53	0.42	0.0214	0.8093	1.0450	1.0005
GdL	17.47	2.78	0.1459	0.7937	1.0518	1.0006
AuL	0.85	0.11	0.0066	0.7508	1.0274	1.0000
Total	100.00	100.00				

Figure 48: EDX analysis after hydroxyapatite coating

To perform elemental analysis of the $Gd_{0.825}Eu_{0.175}B_3O_6$ particle before and after hydroxyapatite coating and to complete the characterization of the hydroxyapatite coating, energy dispersive x-ray analysis was completed and is shown in **Figure 47** and **Figure 48**. According to the analysis results, the Ca/P mass ratio obtained after the coating is calculated as 1.45. Since the mass ratio of Hydroxyapatite itself is 1.67, the result is quite close and the coating is considered to be successful.

3.6 Thermal Gravimetric Analysis and Differential Thermal Analysis

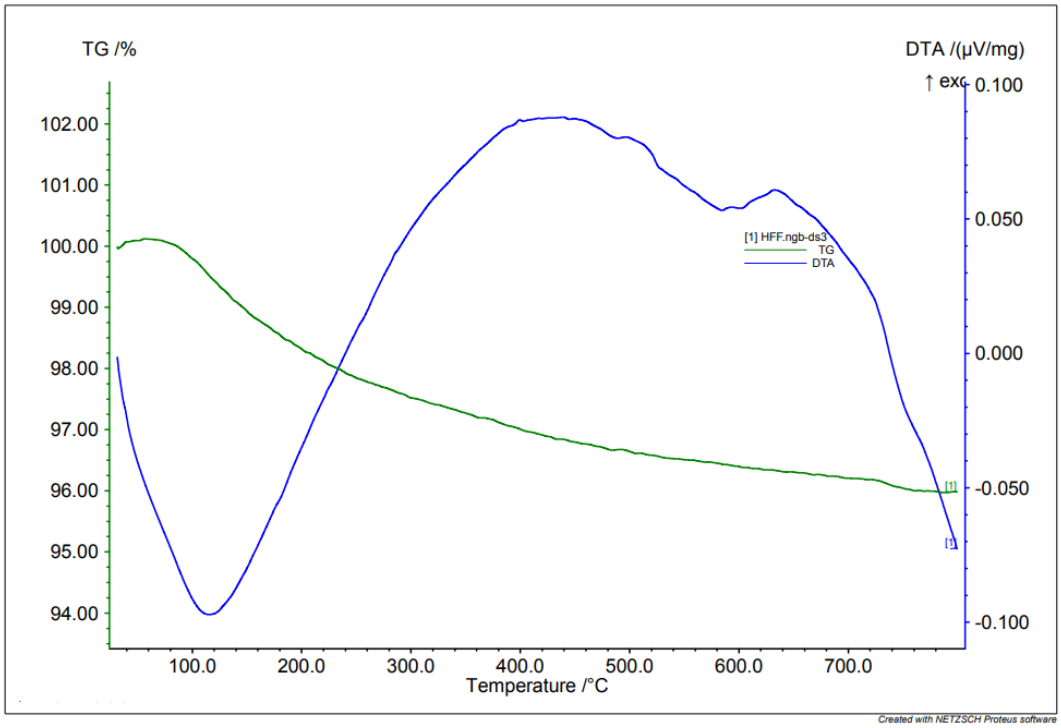

Figure 49: TGA and DTA analysis of $Gd_{0.825}Eu_{0.175}B_3O_6$@HAP

TGA and DTA measurements were performed to characterize how the material behaves at high temperatures and PEGylation. Analyses were carried out in a nitrogen environment with an increase of 10 °C per minute. TGA and DTA measurements of the $Gd_{0.825}Eu_{0.175}B_3O_6$@HAP particle are shown in **Figure 49**. In the measurements taken up to 800°, there is a loss of almost 3.5% and hydroxyapatite and borate, which is a heat-resistant material, did not show any degradation.

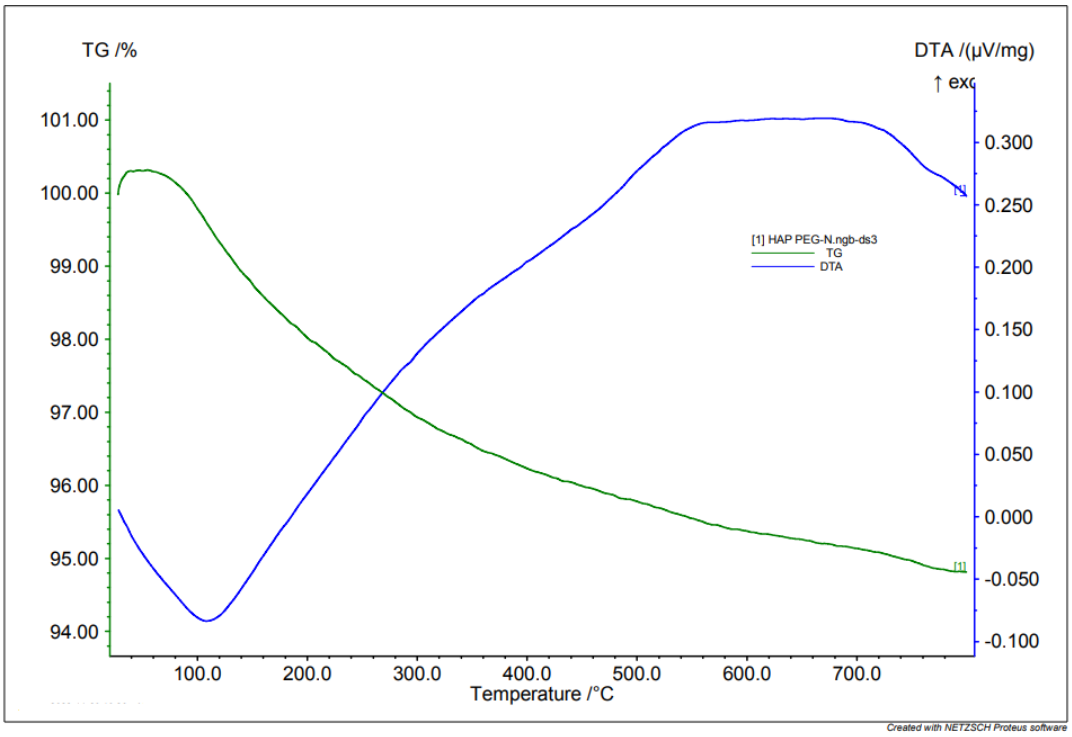

Figure 50: TGA and DTA analysis of $Gd_{0.825}Eu_{0.175}B_3O_6$@HAP@PEG

For the characterization of PEGylation, TGA and DTA of PEG-coated particles were performed. DTA was performed to see any different endothermic or exothermic peaks caused by PEG. As a result of the analysis in **Figure 50**, no different peak was found in DTA. The reason for this can be shown as the PEG coating is less than 2%. Probably PEG was in a smaller amount than DTA could detect and the signal was not detected. On the other hand, when we look at the TGA, the $Gd_{0.825}Eu_{0.175}B_3O_6$@HAP@PEG particles experienced a mass loss close to 5%. This is thought to be the result of the 2% PEG coating and supports that the PEG coating was successful.

3.7 Drug Loading and Release Profile

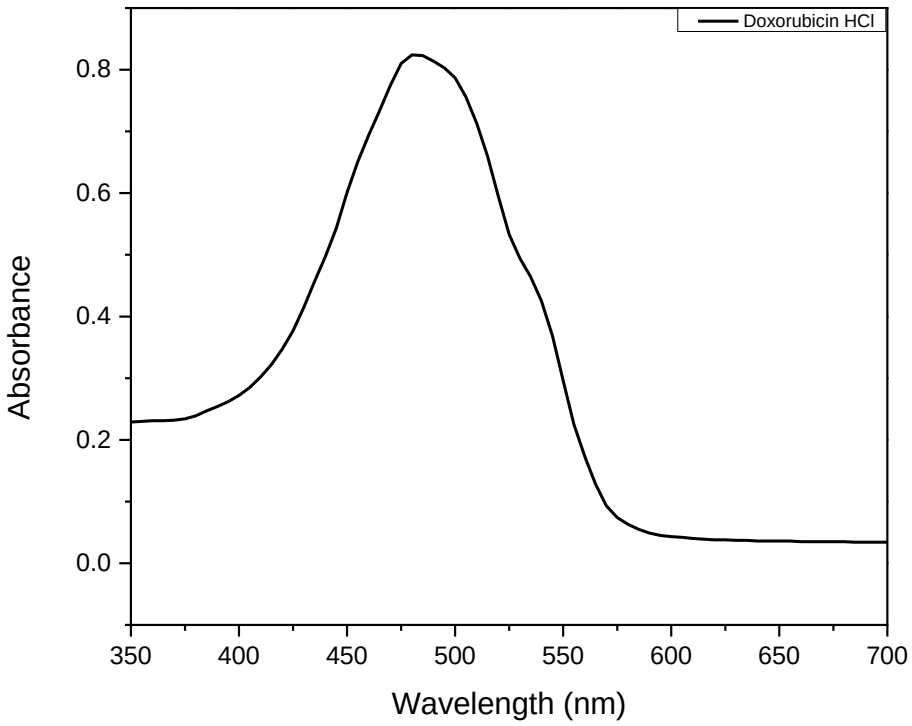

Figure 51: Doxorubicin HCl UV-Vis spectrum

Doxorubicin, an anticancer drug, was used as a model drug. UV-VIS spectrometer was used for the loading and release analysis of doxorubicin. **Figure 51** shows the UV-VIS spectrum of doxorubicin. Doxorubicin has a maximum peak at 480 nm and a molar absorptivity of 11500 $L.mol^{-1}.cm^{-1}$. Separate calibration curves were prepared for water, pH 7.4 PBS buffer and pH 5.5 acetate buffer. To determine drug loading % a water calibration curve was prepared. Moreover, drug molecules concentration was tracked with pH 7.4 PBS buffer and pH 5.5 acetate buffer calibration curves. **Appendices A** shows these calibration curves.

3.7.1 Drug Loading

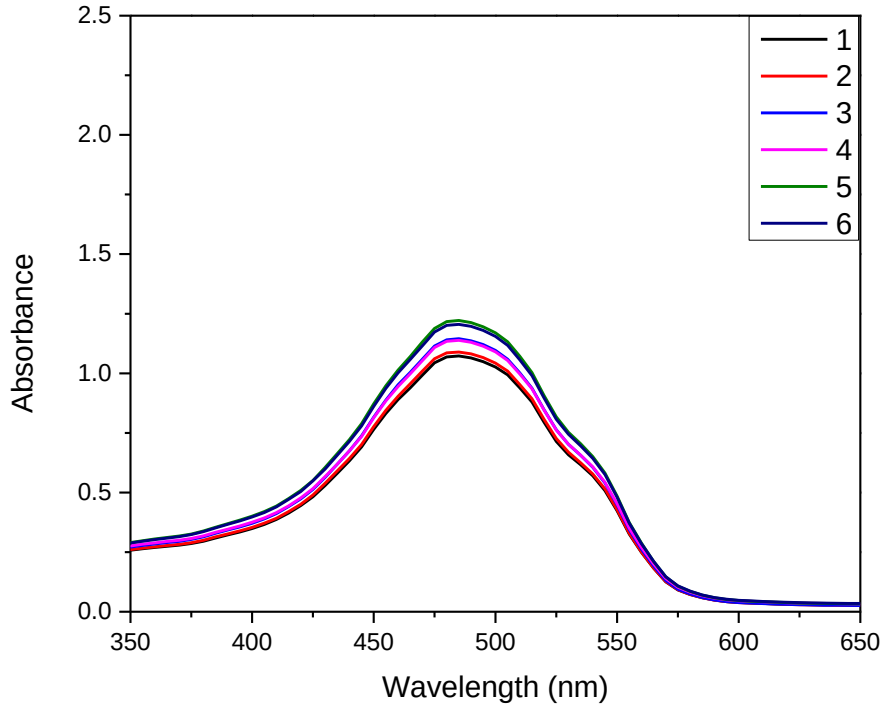

Figure 52: UV-VIS spectrum of supernatant for the $Gd_{0.825}Eu_{0.175}B_3O_6$@HAP@PEG

After the calibration curves were prepared, drug loading was started. $Gd_{0.825}Eu_{0.175}B_3O_6$ nanoparticle with high therapeutic potential was selected for drug loading. As a drug loading procedure, 10 mg of the particles was added into 2 mL 1000 ppm doxorubicin hydrochloride solution. The prepared suspension was firstly stirred in a sonicator for 30 minutes and then stirred in the dark for 24 hours. To prevent oxidation of the doxorubicin. Drug loading processes were done in a nitrogen atmosphere. The suspension was then allowed to separate by centrifugation at 6000 rpm for 10 minutes. The driving force for drug loading is considered as intermolecular forces. Loading was performed for 6 samples to compare the release profiles at pH 7.4 and pH 5.5. Experiments were repeated three times on different days. The data for these six samples are shown in **Figure 52**. The supernatant

obtained after separation was calculated from the absorbance value by water calibration to determine the loading amount.

$$\%\ Loaded\ Drug = \frac{Mass\ of\ drug\ loaded\ (g)}{Mass\ of\ nanoparticles(g)} \text{ x } 100$$

To determine the amount of drug loaded, three different samples were taken from the supernatant and the average of the three was used. The % loaded drug was calculated according to the above equation. Accordingly, the absorbance values for samples 1,2 and 3 were 1.16, 1.17 and 1.21. It is found that 0.73 mg, 0.71 mg, and 0.68 mg of doxorubicin were left in the supernatant respectively. % loaded drug was calculated by subtracting the amount of supernatant from the initial amount. According to the results obtained, the % loaded drug was 7.35%, 7.07% and 6.81% respectively for samples 1,2 and 3 for the experiments that were used in PBS buffer release.

The same procedure has been used for acetate buffer release and the % loaded drug was calculated as 9.06%, 8.33% and 8.31% for samples 4,5 and 6 for the experiments that were used in acetate buffer release.

3.7.2 Drug Release

Drug release studies were performed in pH 7.4 PBS buffer at a temperature of 37° C to simulate blood medium.

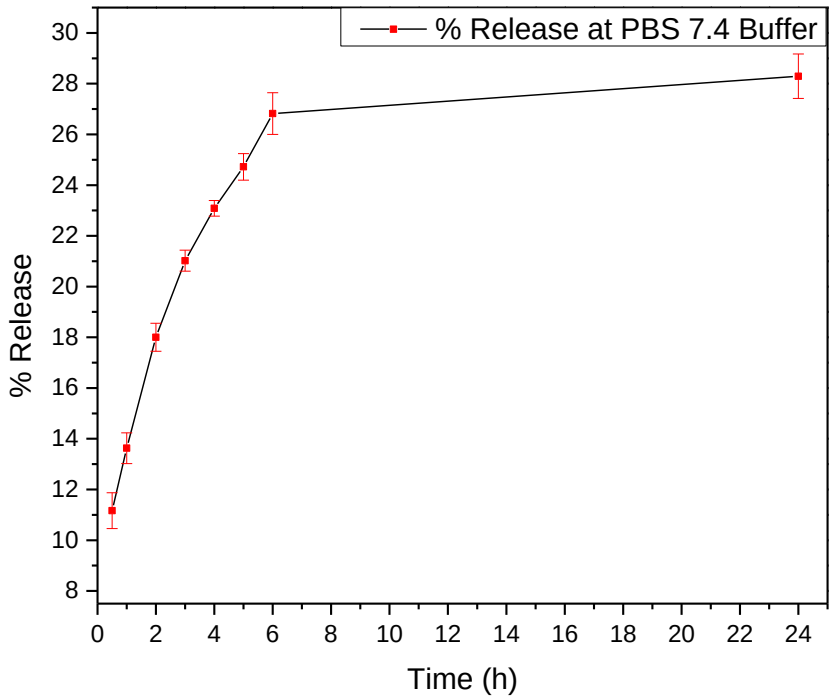

Figure 53: Drug release percent for the PBS pH 7.4 buffer

Firstly, the concentrations were found with the relevant calibration curve for the absorbance values obtained. In the experiments performed at 1 mL, 300 µL of the sample was taken and 300 µL were placed in 96 well plates as 100 µL each. Then 300 µL of fresh PBS was added. For each hour, the number of moles released in the solution was found and the number of moles taken was subtracted and then the new concentration was found. Thus, the number of moles obtained for each hour was determined and the amount of drug loaded was known as % release per hour given in **Figure 53**.

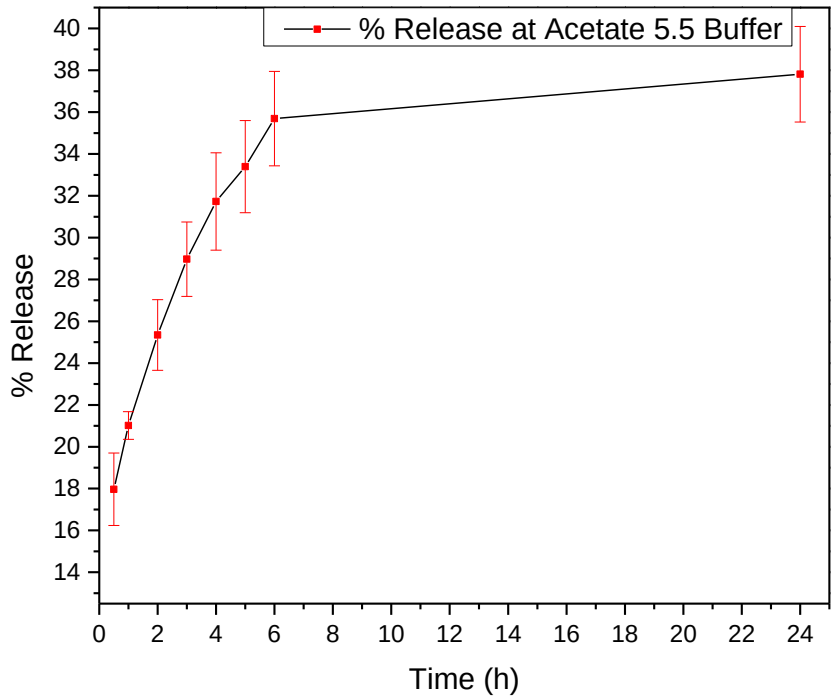

Figure 54: Drug release percent for the pH 5.5 acetate buffer

The same experiments were carried out in acetate pH 5.5 medium under the same conditions. The % release profile as a function of time is given in **Figure 54**. It is a known fact that the surroundings of the tumour cell are more acidic. As glucose consumption increases, lactate and H^+ ions increase and therefore the pH decreases around the tumour. Since the possibility of making a buffer in extracellular cells is limited, the acidity around the tumour cannot be reduced easily (Zhang et al., 2010). As a result of the experiments, 28% of the total loaded drug is released at pH 7.4 in 24 hours, while about 40% is released in a more acidic medium. Moreover, most of the release occurs as a burst in the first 2 hours and subsequent releases happen more slowly in the following hours.

3.7.3 Real Time Monitoring

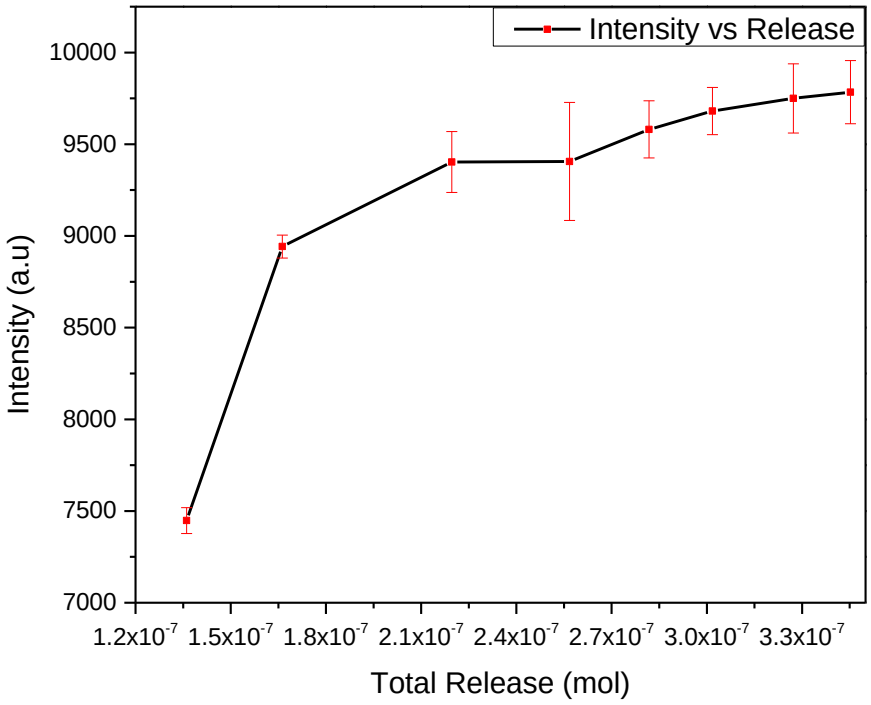

Figure 55: Luminescence intensity as a function of total concentration for PBS pH 7.4

In order to monitor the drug instantaneously, photoluminescence measurements were taken at pH 7.4 during the drug release of $Gd_{0.825}Eu_{0.175}B_3O_6$@HAP@PEG particles and the results of these measurements are given in **Figure 55**. In the analysis, after centrifugation of the drug-loaded particles, photoluminescence measurements were plotted according to the excitation at 394 and emission at 585 nm are shown in the figure. For each hour, the measured particles were taken again and the intensity graph based on the total mole release was plotted for each hour. The increase in intensity as the drug is released is expected which is in line with the literature (Jiang et al., 2014).

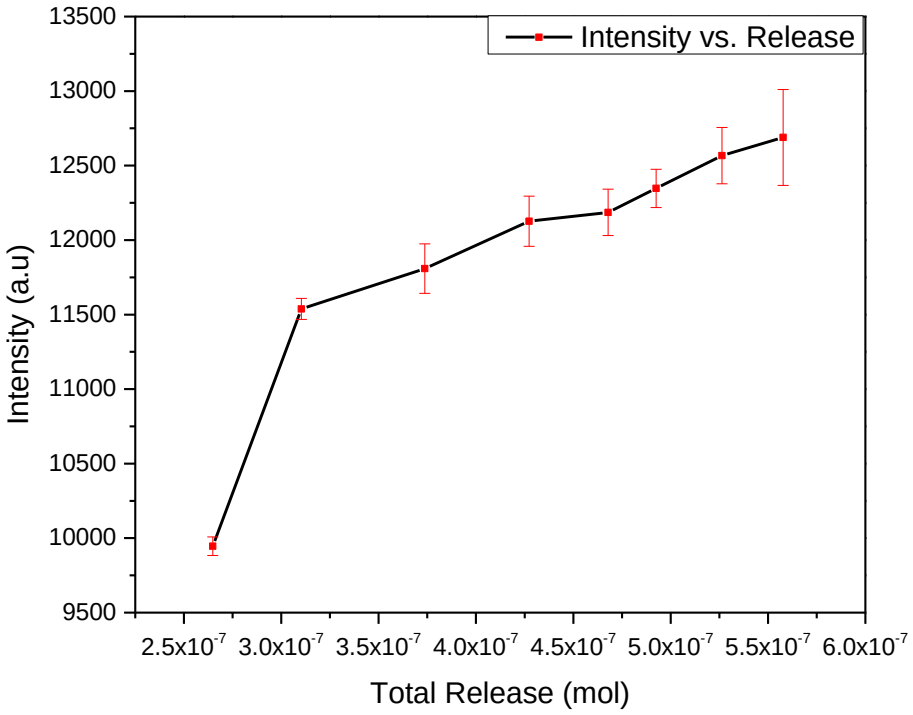

Figure 56: Luminescence intensity as a function of total concentration acetate pH 5.5

Photoluminescence measurements were taken at pH 5.5 during the drug release of $Gd_{0.825}Eu_{0.175}B_3O_6$@HAP@PEG particles and the results of these measurements are given in **Figure 56**. As a result of the analysis, it is known that the intensity is higher in pH 5.5 acetate buffer because more moles are released in the release results. In the experiments performed for real-time monitoring applications, it is seen that the total release can be obtained depending on the intensity. In line with these results, the released drug concentration can be determined depending on the intensity data. This is among the desired results to be obtained with the luminescence core. It shows that real-time monitoring can be performed by using a luminescence core.

3.8 Cell Viability

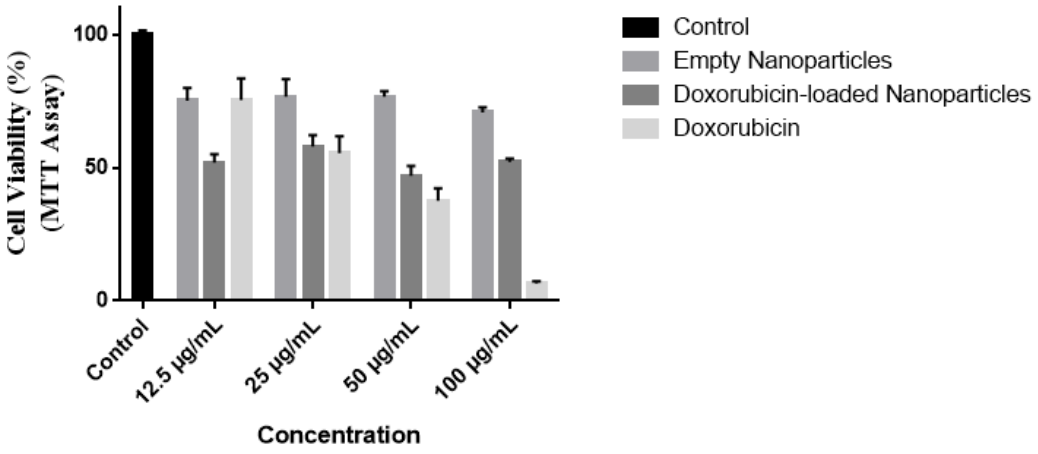

Figure 57: MTT assay of doxorubicin-loaded $Gd_{0.825}Eu_{0.175}B_3O_6$@HAP@PEG particles

In order to monitor cellular cell viability, an MTT assay was performed on the HCT-116 cancer cell line; the results are given in **Figure 57**. In the experiments performed at different concentrations, doxorubicin-treated cancer cells were also included as a control. As a result of the experiments, it was observed that $Gd_{0.825}Eu_{0.175}B_3O_6$@HAP@PEG particles caused nearly 20% of death in the HCT-116 colon cancer line. In experiments with a low concentration of 12 µg/L, drug-loaded particles were calculated to kill more cells than doxorubicin. %50 of the cells were killed by doxorubicin-loaded nanoparticles. Since the particles themselves have a toxic effect and since the doxorubicin concentration has low to kill more cells. Cells were killed by drug-loaded particles at low concentrations. At increasing concentrations, doxorubicin itself was observed to cause more death and cell viability decreased below %10 at 100 µg/L. Albanese et al. observed that agglomeration decreased cellular uptake by 25% compared to monodisperse ones in their experiments (Albanese & Chan, 2011). The zeta potential of the particles measured as -2.54 mV and zeta potential measurements can be seen in **Appendix B**.

This causes it to be prone to agglomerate in the liquid since it is not colloidally stable. More cancer cells could not be killed at high concentrations, probably due to the low cellular uptake of the aggregated particles.

CHAPTER 4

CONCLUSION

Core/shell-type hydroxyapatite and PEG-coated particles $Gd_{0.825}Eu_{0.175}B_3O_6$@HAP@PEG and Ce^{3+}/Tb^{3+} doped GdB_3O_6 particles were successfully synthesized by sol-gel process. The sol-gel process for the $Gd_{0.95}Ce_{0.025}Tb_{0.025}B_3O_6$ particle was carried out with citric acid, glycine, tartaric acid, CTAB and EDTA in the core synthesis. The best crystallinity phase and highest luminescence intensity were observed in CTAB used as a cationic surfactant during the synthesis. Extra $GdBO_3$ phases were found in the GdB_3O_6 structure with citric acid, glycine and tartaric acid chelation. Moreover, the product was found as $GdBO_3$ with EDTA chelation. In the particles doped with different molar ratios of Eu^{3+} ions, an increase in luminescence intensity was observed as the Eu^{3+} ratio increased. The same experiments were performed for the $GdBO_3$ particles and the highest luminescence intensity was obtained at 17.5% Eu^{3+} doping for the GdB_3O_6 structure and 20% Eu^{3+} doping for the $GdBO_3$ structure. Quantum yield was calculated as 19.4% for the $Gd_{0.825}Eu_{0.175}B_3O_6$ particle with a luminescence lifetime of 2 ms. The quantum yield of the $Gd_{0.80}Eu_{0.20}BO_3$ particle was calculated as 3% with a lifetime of 1.5 ms. According to these results, GdB_3O_6 is a better host than $GdBO_3$ in terms of energy transfer and Eu^{3+} ions emissions. Hydroxyapatite was coated on the $Gd_{0.825}Eu_{0.175}B_3O_6$ particles with the wet precipitation method. A decrease in luminescence intensity was observed after the $Gd_{0.825}Eu_{0.125}B_3O_6$ particles were coated with hydroxyapatite due to the absorption of hydroxyapatite at 394 nm. Moreover, the spherical morphology of the $Gd_{0.825}Eu_{0.125}B_3O_6$ particles became prismatic after hydroxyapatite coating. After the PEGylation step, the particles were loaded with doxorubicin. The % loaded drug of particles was calculated as 7.82%. In pH 7.4 PBS, 28% of the drug is released in 24 hours at 37 °C, while in pH 5.5 acetate buffer this rate approaches 40%. This is a positive result for tumour cells,

which have a more acidic environment. Furthermore, luminescence intensity as a function of total drug release was studied for real-time monitoring. As the drug was released, the luminescence intensity of the particles at 585 nm increased.

REFERENCES

Ain, Q. U., Munir, H., Jelani, F., Anjum, F., & Bilal, M. (2019). Antibacterial potential of biomaterial derived nanoparticles for drug delivery application. *Materials Research Express*, *6*(12). https://doi.org/10.1088/2053-1591/ab715d

Akman, P., Ulusan, S., Banerjee, S., & Yilmaz, A. (2020). Core/shell type, Ce^{3+} and Tb^{3+} doped $GdBO_3$ system: Synthesis and Celecoxib drug delivery application. *Microporous and Mesoporous Materials*, *308*. https://doi.org/10.1016/j.micromeso.2020.110528

Albanese, A., & Chan, W. C. W. (2011). Effect of gold nanoparticle aggregation on cell uptake and toxicity. *ACS Nano*, *5*(7), 5478–5489. https://doi.org/10.1021/nn2007496

Balaram, V. (2019). Rare earth elements: A review of applications, occurrence, exploration, analysis, recycling, and environmental impact. *Geoscience Frontiers*, *10*(4), 1285–1303. https://doi.org/10.1016/j.gsf.2018.12.005

Binnemans, K. (2015). Interpretation of Europium(III) spectra. In *Coordination Chemistry Reviews* (Vol. 295, pp. 1–45). Elsevier B.V. https://doi.org/10.1016/j.ccr.2015.02.015

Celik, M. G., Yilmaz, A., & Yazici, A. N. (2017). Synthesis and thermoluminescence characterization of lithium tetraborate ($Li_2B_4O_7$) doped with copper and silver metals. *Radiation Measurements*, *102*, 16–26. https://doi.org/10.1016/j.radmeas.2017.06.002

Chanana, P., Uosef, A., Vaughn, N., Suarez-Villagran, M., Ghobrial, R. M., Kloc, M., & Wosik, J. (2022). The Effect of Magnetic Field Gradient and Gadolinium-Based MRI Contrast Agent Dotarem on Mouse Macrophages. *Cells*, *11*(5). https://doi.org/10.3390/cells11050757

Chung, M. P. (2010). *Handbook on borates: Chemistry, production and applications.* Nova.

Čolović, B., Pašalić, S., & Jokanović, V. (2012). Influence of hydroxyapatite pore geometry on tigecycline release kinetics. *Ceramics International*, *38*(8), 6181–6189. https://doi.org/10.1016/j.ceramint.2012.04.069

Cotton, S. (2006). *Lanthanide and Actinide Chemistry* (1st ed.). Wiley.

Dieke, G. H., & Satten, R. A. (1970). Spectra and Energy Levels of Rare Earth Ions in Crystals. *American Journal of Physics*, *38*(3), 399–400. https://doi.org/10.1119/1.1976350

Esmail, S., & Rafiq, M. (2019). It's All in the History. *Journal of Clinical Review and Case Reports*, *4*(2).

Fan, J., Wang, S., Sun, W., Guo, S., Kang, Y., Du, J., & Peng, X. (2018). Anticancer drug delivery systems based on inorganic nanocarriers with fluorescent tracers. *AIChE Journal*, *64*(3), 835–859. https://doi.org/10.1002/aic.15976

Fontes, A., & Santos, B. S. (2020). *Quantum Dots: Application in Biology (3rd ed.)*. Human Press.

Fujiwara, H. (2003). *Spectroscopic Ellipsometry Principles and Applications*. Wiley.

Gai, S., Li, C., Yang, P., & Lin, J. (2014). Recent progress in rare earth micro/nanocrystals: Soft chemical synthesis, luminescent properties, and biomedical applications. *Chemical Reviews* (Vol. 114, Issue 4, pp. 2343–2389). https://doi.org/10.1021/cr4001594

Guan, A., Zhou, L., Wang, G., Gao, F., Wang, Q., Chen, X., & Li, Y. (2016). Photoluminescence characterization and energy transfer of color-tunable $Li_6Y(BO_3)_3:Ce^{3+}$, Tb^{3+} phosphors. *Physica B: Condensed Matter*, *494*, 75–81. https://doi.org/10.1016/j.physb.2016.04.040

Guleria, A., Pranjali, P., Meher, M. K., Chaturvedi, A., Chakraborti, S., Raj, R., Poluri, K. M., & Kumar, D. (2019). Effect of Polyol Chain Length on Proton Relaxivity of Gadolinium Oxide Nanoparticles for Enhanced Magnetic Resonance Imaging Contrast. *Journal of Physical Chemistry C*, *123*(29), 18061–18070. https://doi.org/10.1021/acs.jpcc.9b04089

Huy, B. T., Kwon, D. H., Lee, S. S., Dao, V. D., Truong, H. B., & Lee, Y. I. (2022). Optical properties of Sr_2YF_7 material doped with Yb^{3+}, Er^{3+}, and Eu^{3+} ions for solar cell application. *Journal of Alloys and Compounds*, *897*. https://doi.org/10.1016/j.jallcom.2021.163189

Icten, O., Kose, D. A., & Zumreoglu-Karan, B. (2017). Fabrication and characterization of magnetite-gadolinium borate nanocomposites. *Journal of Alloys and Compounds*, *726*, 437–444. https://doi.org/10.1016/j.jallcom.2017.07.277

Jiang, F., Wang, D. P., Ye, S., & Zhao, X. (2014). Strontium-substituted, luminescent and mesoporous hydroxyapatite microspheres for sustained drug release. *Journal of Materials Science: Materials in Medicine*, *25*(2), 391–400. https://doi.org/10.1007/s10856-013-5081-4

Ju, G., Hu, Y., Chen, L., Wang, X., & Mu, Z. (2013). Concentration quenching of persistent luminescence. *Physica B: Condensed Matter*, *415*, 1–4. https://doi.org/10.1016/j.physb.2013.01.027

Kenan Yünlü. (2016). *BOR* (1st ed.). BOREN.

Kubin, R. F., & Fletcher A.F. (1982). Fluorescence quantum yields of some rhodamine dyes. *Journal of Luminescence*, *27*(4), 455–462.

Lakowicz, J. R. (2006). *Principles of Fluorescence Spectroscopy (3rd ed.)*. Springer.

Le Khanh, H. P., Nemes, D., Rusznyák, Á., Ujhelyi, Z., Fehér, P., Fenyvesi, F., Váradi, J., Vecsernyés, M., & Bácskay, I. (2022). Comparative Investigation

of Cellular Effects of Polyethylene Glycol (PEG) Derivatives. *Polymers*, *14*(2). https://doi.org/10.3390/polym14020279

Lee, P. I., & Li, J.-X. (2010). *Evolution of Oral Controlled Release Dosage Forms*. John Wiley & Sons, Inc.

Li, R. (1989). The Interpretation of UV Absorption of Borate Glasses and Crystals. *Journal of Non-Crystalline Solids*, *111*(2-3), 199-204. https://doi.org/10.1016/0022-3093(89)90281-0

Liu, G., & Jacquier, B. (2005). *Spectroscopic Properties of Rare Earths in Optical Materials* (1st ed., Vol. 83). Springer Links.

Loca, D., Locs, J., Dubnika, A., Zalite, V., & Berzina-Cimdina, L. (2015). Porous hydroxyapatite for drug delivery. In *Hydroxyapatite (Hap) for Biomedical Applications* (pp. 189–209). Elsevier. https://doi.org/10.1016/b978-1-78242-033-0.00009-2

Maggay, I. V. B., Lin, P. C., & Liu, W. R. (2015). Investigation of luminescence properties and the energy transfer mechanism of $Li_6Lu(BO_3)_3:Ce^{3+}$, Tb^{3+} green-emitting phosphors. *RSC Advances*, *5*(8), 5591–5597. https://doi.org/10.1039/c4ra12538j

Mark Fox. (2010). *Optical Properties of Solids* (2nd ed.). Oxford University Press Inc., New York.

Meng, F., Zhang, X., Li, W., Xie, T., & Seo, H. J. (2012). Luminescence and time-resolved spectroscopy properties of $(Gd_{1-x}Eu_x)(BO_2)_3$ multicrystals. *Journal of Physics and Chemistry of Solids*, *73*(4), 564–567. https://doi.org/10.1016/j.jpcs.2011.12.006

Mohd Pu'ad, N. A. S., Abdul Haq, R. H., Mohd Noh, H., Abdullah, H. Z., Idris, M. I., & Lee, T. C. (2019). Synthesis method of hydroxyapatite: A review. *Materials Today: Proceedings*, *29*, 233–239. https://doi.org/10.1016/j.matpr.2020.05.536

Mondal, S., Manivasagan, P., Bharathiraja, S., Moorthy, M. S., Nguyen, V. T., Kim, H. H., Nam, S. Y., Lee, K. D., & Oh, J. (2017). Hydroxyapatite coated iron oxide nanoparticles: A promising nanomaterial for magnetic hyperthermia cancer treatment. *Nanomaterials*, *7*(12). https://doi.org/10.3390/nano7120426

Mukherjee, P., Suard, E., & Dutton, S. E. (2017). Magnetic properties of monoclinic lanthanide metaborates, $Ln(BO_2)_3$, Ln = Pr, Nd, Gd, Tb. *Journal of Physics Condensed Matter*, *29*(40). https://doi.org/10.1088/1361-648X/aa8160

Munir, M. U., Salman, S., Javed, I., Bukhari, S. N. A., Ahmad, N., Shad, N. A., & Aziz, F. (2021). Nano-hydroxyapatite as a delivery system: overview and advancements. In *Artificial Cells, Nanomedicine and Biotechnology*, *49*(1), 717–727. Taylor and Francis Ltd. https://doi.org/10.1080/21691401.2021.2016785

Mutailipu, M., Poeppelmeier, K. R., & Pan, S. (2021). Borates: A Rich Source for Optical Materials. *Chemical Reviews*, *121*(3), 1130–1202. American Chemical Society. https://doi.org/10.1021/acs.chemrev.0c00796

Noto, L. L., Swart, H. C., Mothudi, B. M., Mbule, P. S., & Dhlamini, M. S. (2016). The Dynamics of Luminescence. In *Luminescence - An Outlook on the Phenomena and their Applications*. InTech. https://doi.org/10.5772/65050

Obodovskiy, I. (2019). Luminescence. In *Radiation* (pp. 207–220). Elsevier. https://doi.org/10.1016/B978-0-444-63979-0.00012-4

Ortega-Berlanga, B., Betancourt-Mendiola, L., del Angel-Olarte, C., Hernández-Adame, L., Rosales-Mendoza, S., & Palestino, G. (2021). An overview of gadolinium-based oxide and oxysulfide particles: Synthesis, properties, and biomedical applications. In *Crystals*, *11*(9). MDPI. https://doi.org/10.3390/cryst11091094

Pawade, V. B., Chopra, V., & Dhoble, S. J. (2019). Introduction to electronic spectroscopy of lanthanide, properties, and their applications. In *Spectroscopy of Lanthanide Doped Oxide Materials*, 1–20. Elsevier Inc. https://doi.org/10.1016/B978-0-08-102935-0.00001-0

Peter Atkins, Julio de Paula, & James Keeler. (2018). *Atkins' Physical Chemistry (11th ed.).* Oxford University Press.

Ranjeh, M., Beshkar, F., Amiri, O., Salavati-Niasari, M., & Moayedi, H. (2020). Pechini sol-gel synthesis of Cu_2O/Li_3BO_3 and CuO/Li_3BO_3 nanocomposites for visible light-driven photocatalytic degradation of dye pollutant. *Journal of Alloys and Compounds*, *815*. https://doi.org/10.1016/j.jallcom.2019.152451

Rujitanapanich, S., Kumpapan, P., & Wanjanoi, P. (2014). Synthesis of hydroxyapatite from oyster shell via precipitation. *Energy Procedia*, *56*(C), 112–117. https://doi.org/10.1016/j.egypro.2014.07.138

Sasidharanpillai, S., Arcis, H., Trevani, L., & Tremaine, P. R. (2019). Triborate Formation Constants and Polyborate Speciation under Hydrothermal Conditions by Raman Spectroscopy using a Titanium/Sapphire Flow Cell. *The Journal of Physical Chemistry B*, *123*(24), 5147–5159. https://doi.org/10.1021/acs.jpcb.9b03062

Sauer, M., Hofkens, J., & Enderlein, J. (2011). *Handbook of Fluorescence Spectroscopy and Imaging*. Wiley. https://doi.org/10.1002/9783527633500

Schmitt, M. K., & Huppertz, H. (2017). β-$Y(BO_2)_3$ - A new member of the β-$Ln(BO_2)_3$ (Ln = Nd, Sm, Gd-Lu) structure family. *Zeitschrift Fur Naturforschung - Section B Journal of Chemical Sciences*, *72*(12), 983–988. https://doi.org/10.1515/znb-2017-0151

Schott, J., Kretzschmar, J., Acker, M., Eidner, S., Kumke, M. U., Drobot, B., Barkleit, A., Taut, S., Brendler, V., & Stumpf, T. (2014). Formation of a Eu(iii) borate solid species from a weak Eu(iii) borate complex in aqueous

solution. *Journal of the Chemical Society. Dalton Transactions*, *43*(30), 11516–11528. https://doi.org/10.1039/c4dt00843j

Seraiche, M., Guerbous, L., Mahiou, R., & Potdevin, A. (2020a). Synthesis of $GdBO_3$:Eu^{3+} nanophosphors via acetylacetone assisted aqueous sol–gel route: Effect of some synthesis parameters. *Optical Materials*, *109*. https://doi.org/10.1016/j.optmat.2020.110339

Severoğlu, M. (2016). *Microwave Assisted Solid State Synthesis of Rare Earth Ions Doped $LaBO_3$, YBO_3 AND $GdBO_3$, Their Characterizations and Investigations of Luminescence Properties*.

Suk, J. S., Xu, Q., Kim, N., Hanes, J., & Ensign, L. M. (2016). PEGylation as a strategy for improving nanoparticle-based drug and gene delivery. In *Advanced Drug Delivery Reviews* (Vol. 99, pp. 28–51). Elsevier B.V. https://doi.org/10.1016/j.addr.2015.09.012

Taneroğlu, O. (2020). *Synthesis and Investigation of Optical Properties of Ce^{3+} , Dy^{3+} , Eu^{3+} Single Doped, Ce^{3+} /Dy^{3+} Codoped, Dy^{3+} /Ce^{3+} /Eu^{3+} and Yb^{3+} Single Doped, Tb^{3+} /Ce^{3+} /Yb^{3+} triple Doped $GdBO_3$.*

Tian, G., Gu, Z., Zhou, L., Yin, W., Liu, X., Yan, L., Jin, S., Ren, W., Xing, G., Li, S., & Zhao, Y. (2012). Mn^{2+} dopant-controlled synthesis of $NaYF_4$:Yb/Er upconversion nanoparticles for in vivo imaging and drug delivery. *Advanced Materials*, *24*(9), 1226–1231. https://doi.org/10.1002/adma.201104741

Valeur, B., & Berberan-Santos, M. N. (2011). A brief history of fluorescence and phosphorescence before the emergence of quantum theory. In *Journal of Chemical Education* (Vol. 88, Issue 6, pp. 731–738). https://doi.org/10.1021/ed100182h

Venkatasubbu, G. D., Ramasamy, S., Avadhani, G. S., Ramakrishnan, V., & Kumar, J. (2013). Surface modification and paclitaxel drug delivery of folic acid modified polyethylene glycol functionalized hydroxyapatite

nanoparticles. *Powder Technology*, *235*, 437–442. https://doi.org/10.1016/j.powtec.2012.11.003

Wang, J., Yu, S., & Zhang, H. (2019). Effect of surfactants on photoluminescence properties of ZnO synthesized by hydrothermal method. *Optik*, *180*, 20–26. https://doi.org/10.1016/j.ijleo.2018.11.062

Wang, P., He, D., Xu, C., Ren, X., Lei, L., Wang, S., Peng, F., Yan, X., Liu, D., Wang, Q., Xiong, L., & Liu, J. (2014). High-pressure x-ray diffraction study of YBO_3/Eu^{3+}, $GdBO_3$, and $EuBO_3$: Pressure-induced amorphization in $GdBO_3$. *Journal of Applied Physics*, *115*(4). https://doi.org/10.1063/1.4862653

Weir, C. E., & Schroeder, R. A. (2000). Infrared Spectra of the Crystalline Inorganic Borates. *Journal of Research of the National Bureau of Standards-A. Physics and Chemistry*, *68*(5). https://doi.org/10.6028/jres.068A.045

Wilczewska, A. Z., Niemirowicz, K., & Markiewicz, K. H. (2012). *Nanoparticles as drug delivery systems*.

Ye, M., Kim, S., & Park, K. (2010). Issues in long-term protein delivery using biodegradable microparticles. In *Journal of Controlled Release*, *146*(2), 241–260. Elsevier B.V. https://doi.org/10.1016/j.jconrel.2010.05.011

Yun, Y. H., Lee, B. K., & Park, K. (2015). Controlled Drug Delivery: Historical perspective for the next generation. *Journal of Controlled Release*, *219*, 2–7. https://doi.org/10.1016/j.jconrel.2015.10.005

Zhang, X., Lin, Y., & Gillies, R. J. (2010). Tumor pH and Its Measurement. *Journal of Nuclear Medicine*, *51*(8), 1167–1170. https://doi.org/10.2967/jnumed.109.068981

APPENDICES

A. Calibration Curve for Doxorubicin

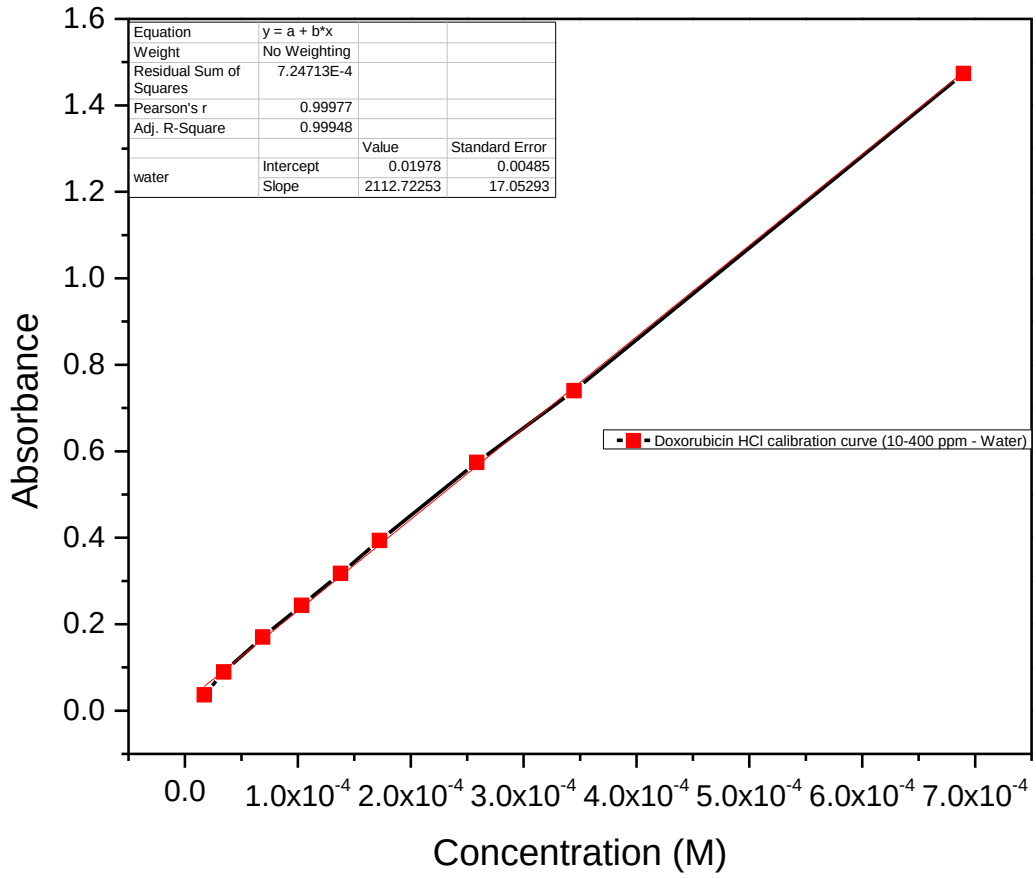

Figure 58: Calibration Curve of Doxorubicin in water

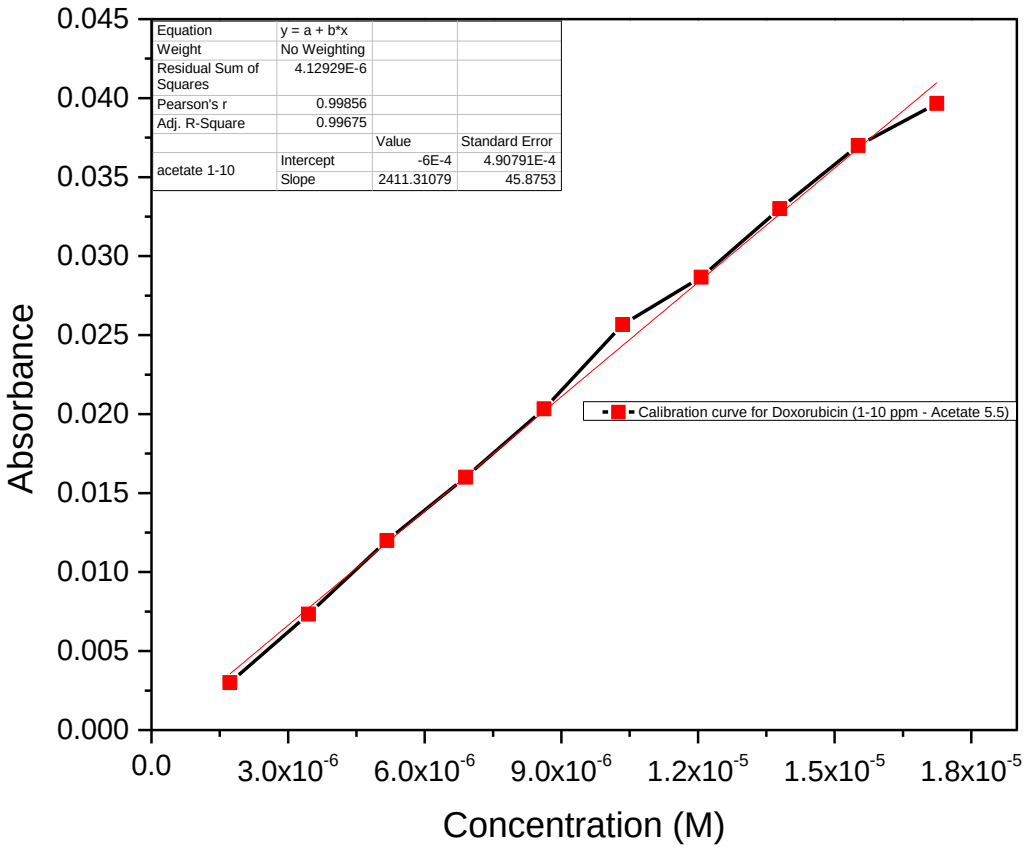

Figure 59: Calibration Curve of Doxorubicin in pH 5.5 acetate buffer

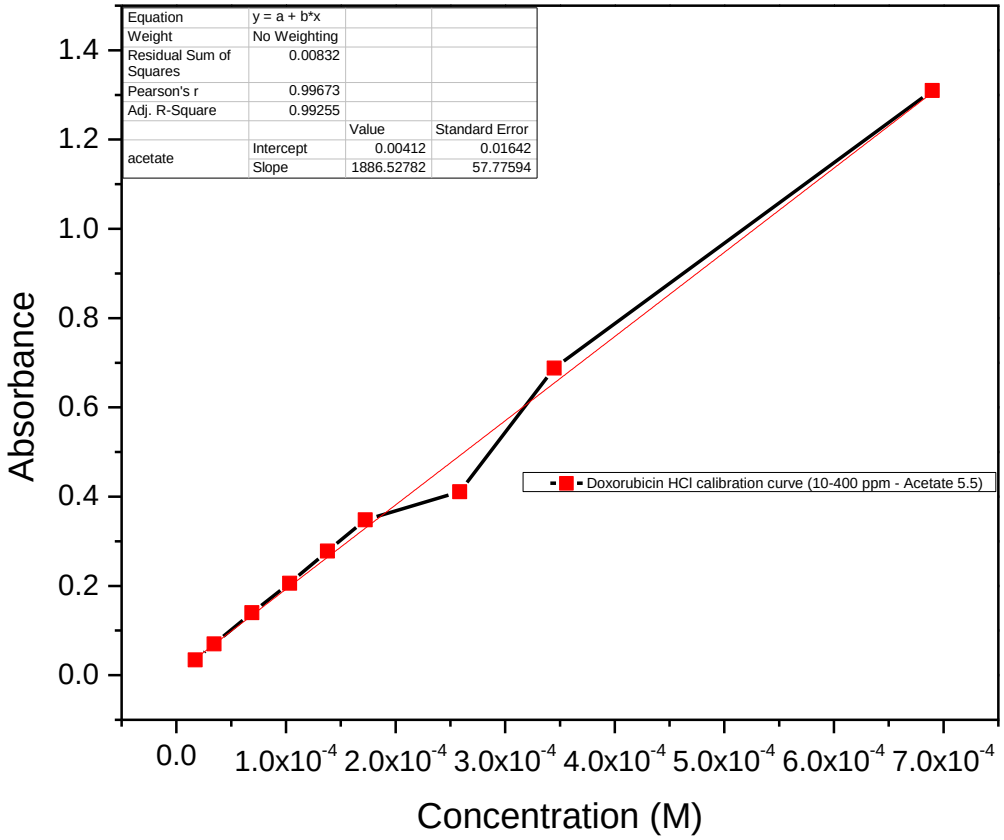

Figure 60: Calibration Curve of Doxorubicin in pH 5.5 acetate buffer

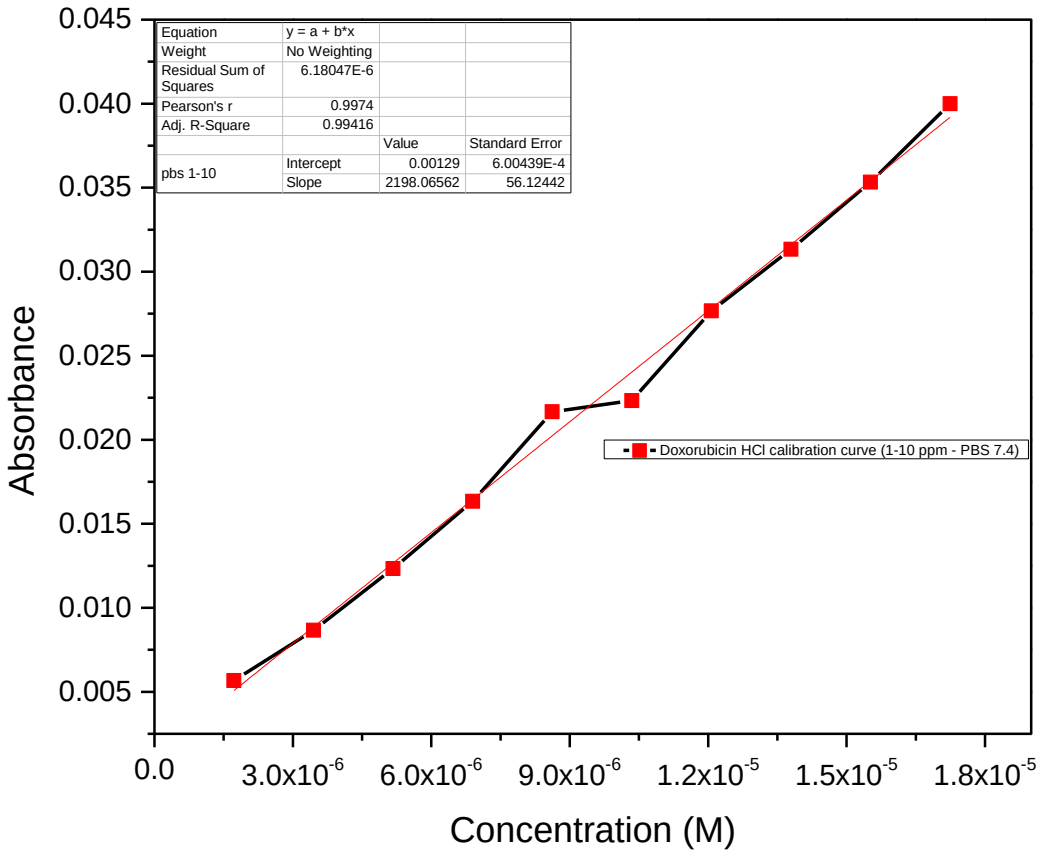

Figure 61: Calibration Curve of Doxorubicin in pH 7.4 phosphate buffer

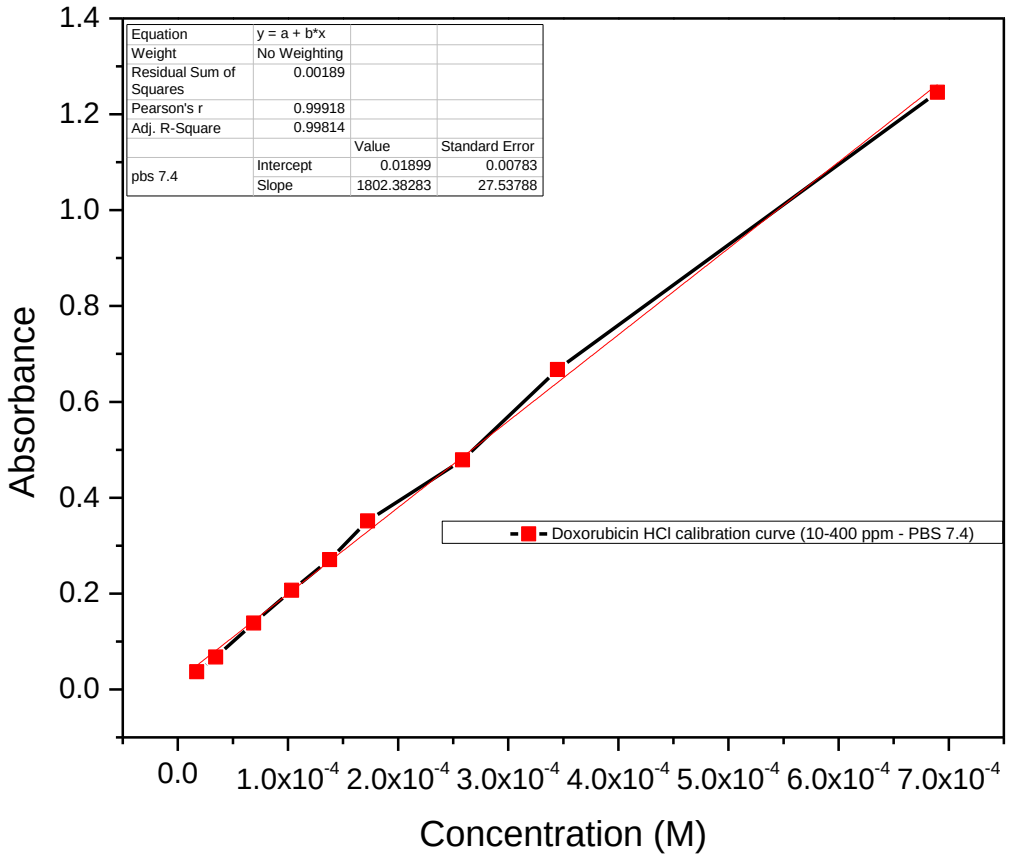

Figure 62: Calibration Curve of Doxorubicin in pH 7.4 phosphate buffer

B. Zeta Potential Measurements

Results

		Mean (mV)	Area (%)	St Dev (mV)
Zeta Potential (mV): -30.7	**Peak 1:**	-30.7	100.0	8.09
Zeta Deviation (mV): 8.09	**Peak 2:**	0.00	0.0	0.00
Conductivity (mS/cm): 0.0197	**Peak 3:**	0.00	0.0	0.00
Result quality : Good				

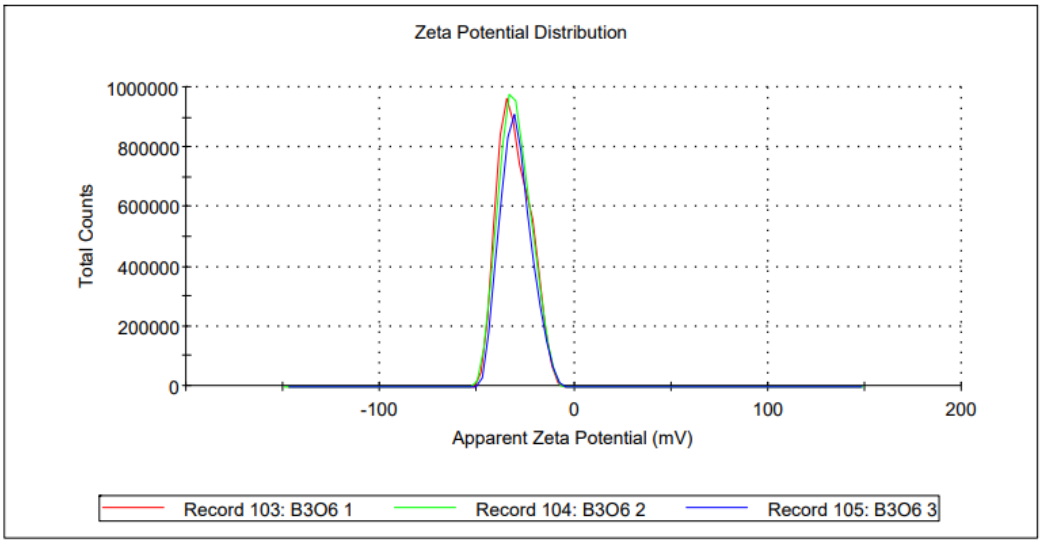

Figure 63: Zeta potential measurement of $Gd_{0.825}Eu_{0.175}B_3O_6$

Results

			Mean (mV)	Area (%)	St Dev (mV)
Zeta Potential (mV):	-2.12	**Peak 1:**	-2.12	100.0	5.96
Zeta Deviation (mV):	5.96	**Peak 2:**	0.00	0.0	0.00
Conductivity (mS/cm):	0.0290	**Peak 3:**	0.00	0.0	0.00
Result quality :	Good				

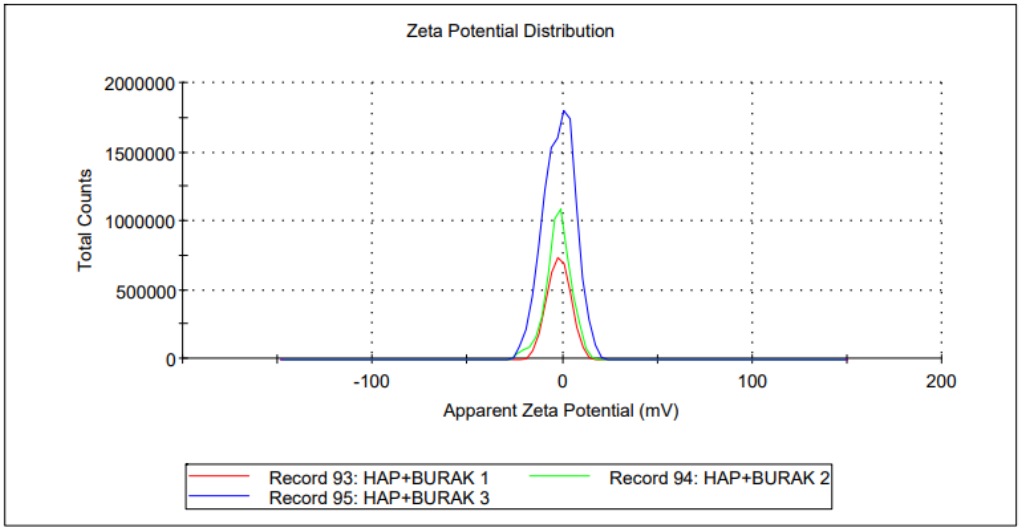

Figure 64: Zeta potential measurement of $Gd0_{.825}Eu_{0.175}B_3O_6$@HAP

Results

		Mean (mV)	Area (%)	St Dev (mV)
Zeta Potential (mV): -2.54	**Peak 1:**	-7.05	60.0	4.88
Zeta Deviation (mV): 7.81	**Peak 2:**	4.81	40.0	4.23
Conductivity (mS/cm): 0.0128	**Peak 3:**	0.00	0.0	0.00

Result quality : Good

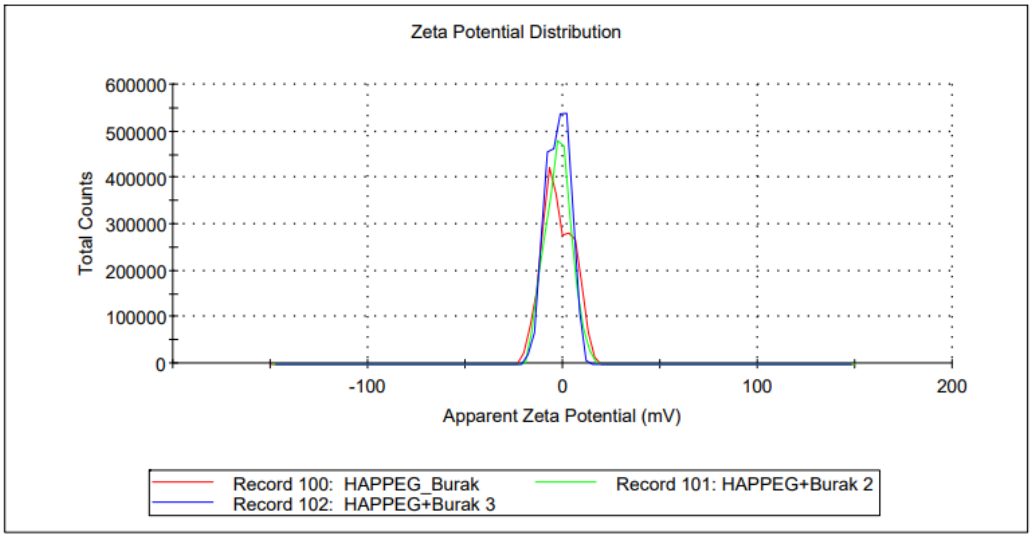

Figure 65: Zeta potential measurement of $Gd_{0.825}Eu_{0.175}B_3O_6$@HAP@PEG